UNIVERSITÀ
DEGLI STUDI
FIRENZE

DOTTORATO DI RICERCA IN
Informatica Sistemi e Telecomunicazioni
Indirizzo: Dinamica non lineare e sistemi complessi

CICLO XXVIII

COORDINATORE Prof. Luigi Chisci

BIOLOGICAL RELEVANCE OF SPIKING NEURAL NETWORKS

Settore Scientifico Disciplinare FIS/07

Dottorando
Dott. *Angulo-Garcia David*

Tutore
Prof. *Torcini Alessandro*

Co Tutore
Dott. *Kreuz Thomas*

Coordinatore
Prof. *Chisci Luigi*

Anni 2012/2015

Presentazione del Collegio alla Commissione di David Angulo Garcia

David Angulo-Garcia (DAG) è uno studente di dottorato Marie Curie nell'ambito del progetto Neural Engineering Transformative Technologies (NETT) ed è stato selezionato da una commissione internazionale fra più di 50 altri candidati da tutto il mondo. La sua attività di ricerca nel triennio ha riguardato lo studio e la caratterizzazione della dinamica di reti neurali. Questa tematica trova collocazione nell'ambito delle Neuroscienze Computazionali, uno dei campi di ricerca in maggiore espansione negli ultimi anni, basti citare l'iniziativa europea Human Brain finanziata con un miliardo di euro per i prossimi 10 anni. In questi tre anni DAG grazie ai fondi europei a lui allocati ha potuto seguire con notevole profitto prestigiose scuole internazionali organizzate sia in ambito NETT, che da istituzioni indipendenti, quali il Bernstein Center di Goettingen in Germania o la Ottawa University in Canada. DAG ha inoltre presentato poster e seminari in ambito nazionale ed internazionale, a conferenze sia sui sistemi dinamici che di neuroscienze computazionali.

Nei primi due anni di tesi DAG ha applicato indicatori innovativi alla caratterizzazione della stabilità lineare e non lineare di reti neurali eccitatorie ed inibitorie. DAG ha poi sviluppato una nuova tecnica di riscostruzione stocastica della dinamica microscopica e macroscopica per reti neurali sparse, che può essere applicata alla dinamica di ogni rete complessa che presenti una connettività random. Infine la sua attività ha riguardato reti neurali con possibili applicazioni di rilevanza fisiologica. In questo senso la collaborazione con il prof. Joshua D. Berke, direttore del Berke Laboratory presso la Michigan University in USA, è stata essenziale in quanto ha consentito di sviluppare a partire dai modelli studiati da David nei primi due anni di tesi, un modello semplice per la dinamica di neuroni dello Striato. Questo modello è capace di predire comportamenti dinamici dello Striato osservati non solo in ratti sani, ma anche in ratti affetti da sindromi quali quella di Parkinson e quella di Hungtinton. Può quindi essere utile per fornire qualche indicazione sulle deficienze fisiologiche alla base di queste sindromi neurali.

Il lavoro di tesi, svolto con estremo impegno e rigore metodologico, ha riguardato aspetti teorici, algoritmici e computazionali, e ha fornito importanti contributi innovativi nell'ambito della caratterizzazione della dinamica di reti neurali e nella modellizzazione di circuiti neurali. I risultati della ricerca sono stati oggetto di due pubblicazioni su riviste internazionali e di una pubblicazione che è nella fase di seconda revisione con alte possibilità di stampa a breve. La tesi sintetizza in modo organico e razionale le varie problematiche affrontate ed i risultati conseguiti.

Il Collegio esprime notevole apprezzamento per il lavoro svolto da David Angulo Garcia durante i suoi studi dottorali e ritiene che egli abbia raggiunto un grado di autonomia assai significativo nello svolgere attività di ricerca scientifica ed un ottimo rigore metodologico.

Pubblicazioni

[1] **D. Angulo-Garcia** and A. Torcini, "Stable chaos in fluctuation driven neural circuits," *Chaos, Solitons and Fractals* 69, 233-245 (2014).

[2] **D. Angulo-Garcia** and A. Torcini, "Stochastic mean field formulation of the dynamics of diluted neural networks," *Phys. Rev. E* 91, 022928 (2015).

[3] **D. Angulo-Garcia**, J.D. Berke, and A. Torcini, "Cell assembly dynamics of sparsely-connected inhibitory networks: a simple model for the collective activity of striatal projection neurons," *Plos Comp Biology*, under review (2015).

Il coordinatore del Dottorato

Prof. Luigi Chisci

Acknowledgements

I wish to thank on the first place the continuous support, both academic and personal, of my supervisor Dr. Alessandro Torcini through the development of the thesis and in general this three-year experience.

I am also grateful with all the staff working at the *Istituto dei Sistemi Complessi* (ISC) and in general at the *Consiglio Nazionale delle Ricerche* (CNR) in Sesto Fiorentino - Italy, where I developed most of my research. In particular I would like to acknowledge my colleagues, Dr. Simona Olmi, Dr. Stefano Lepri and Dr. Stefano Luccioli for productive discussions, and the disposition to give me a hand whenever possible, not only at a professional level, but also in my daily life activities. Special thanks to Nebojsa Bozanic, Thomas Kreuz and Mario Mulansky, also at the ISC, as they contributed significantly to the progress of my research and, during the process, they also became my friends.

A very special acknowledge goes to my family: Fabiola, Andres, Gerard, Isabel, and more recently Miguel Angel; without their unconditional affection, advice and encouragement to follow my career it would have been impossible to achieve my successes. I sincerely thank all the people that regularly reminded me my homeland affection specially Santiago Rubio, Jonathan Moncada, Andres Henao and Alejandra Marin, as well as those who created a familiar environment for me far from home: Indira Rodriguez, Aida Cavallo and Fabio De Francesco.

I express also my gratitude to *Aethia*, and in particular Gianpaolo Perego for providing me the industrial training during the internship at Biopmed cluster.

I would like to extend the acknowledge to all the people that, directly or indirectly contributed to my professional and individual growth.

This work wouldn't be possible without the financial support provided by the European Commission under the program "Marie Curie Network for Initial Training", through the project N. 289146, "Neural Engineering Transformative Technologies (NETT)". I thank also the financial support provided by the "Departamento Adminsitrativo de Ciencia Tecnologia e Innovacion - Colciencias" through the program "Doctorados en el exterior - 2012".

Contents

Chapter 1

Introduction

Few disciplines in the last decades have attracted as much attention as the neurosciences. The rapid growth of new techniques capable of measuring *in-vivo* and *in-vitro* the activity of the brain, has lead to a formidable increase of the efforts aiming to understand the functioning of the most complicated structure of living bodies. These techniques cover a wide range of spatial and temporal resolutions [1, 2, 3, 4]: From techniques aiming to the meausrement of the collective behavior of large neuronal networks during long time spans, such as EEG or fMRI, to more refined techniques designed for the measurement of single cells dynamics with a time precision to the order of milliseconds, for instance Dynamic Patch Clamp technique [1, 5] (see Fig. 1.1). The application of these techniques has helped neuroscientists to reveal the mechanisms involved in cognitive, behavioral and sensory-motor functioning at different scales [6].

Parallel to the development of biomedical and neural engineering procedures, an important part of the progress in the neuro-engineering field has been achieved thanks to mathematical models implemented to explain the experimental findings. The *in-silico* approach to the study of the brain represented a break-through in neuroscience starting from the seminal works by Hodgkin and Huxley on the squid giant axon [7, 8, 9, 10, 11]. Their description of the neuronal activity in terms of a set of ordinary differential equations, published in 1952 and awarded with the Nobel prize in 1963, turned out to be very accurate as it characterized in detail the dynamics of ionic channels present in real neurons. Since then, most of the contributions to the modeling of neuronal dynamics had the purpose of simplifying the mathematical description of the neuronal activity, allowing for a mathematical treatment [12]. Examples of remarkable simplified models, include the FitzHugh-Nagumo [13, 14] and the $I_{Na,p} + I_k$ model [15], (see [16] for other examples). Among the simplified models, one of the most employed is the Leaky Integrate-and-Fire (LIF) model (see [17, 18] for a review). Its simplicity has allowed for the employment of statistical mechanics tools (such as the Fokker-Planck description) to analyze the response of neural networks via mean field reductions [19, 20, 21, 22]. Throughout this dissertation, the LIF neuron model is regarded as our working tool.

The simplification of the neural dynamics in the LIF formulation is certainly

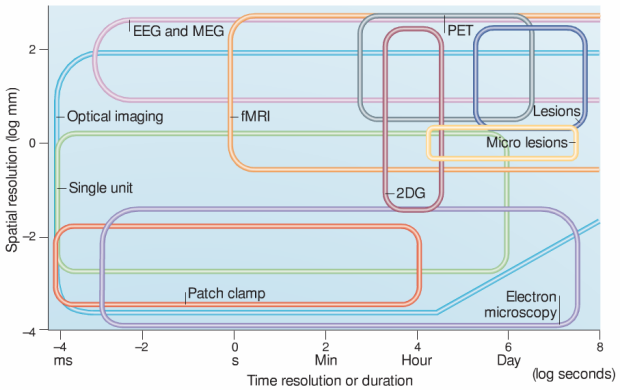

Figure 1.1: Spatio-temporal scale resolution of some of the most widely used neural engineering techniques. Vertical (horizontal) axis depicts the scale of spatial (temporal) resolution. EEG: Electroencephalography; fMRI: Functional Magnetic Resonance Imaginig; PET: Positron Emission Tomography; 2DG: 2-deoxy-D-glucose Imaging. Figure taken from [1]

a drawback from the single cell dynamics viewpoint. However this simplified form allows for the study of the behavior of large number of interacting neurons. Understanding how the neurons interact among them is a fundamental process when formulating a network model. The communication among neurons occurs via the transmission of electrical pulses termed action potentials. Action potentials are delivered by specialized structures: the *synapses*. The action potential emitted by the pre-synaptic neuron, arrives to the axon terminal and produces the release of neurotransmitters. After release, these neurotransmitters are bound to specialized receptors at the post-synaptic neuron which allows the flow of specific types of ions. If the ionic current at the synapse contributes to the depolarization of the membrane potential in the post-synaptic neuron it is called Excitatory Post-synaptic Potential (EPSP), if it hyperpolarizes the membrane potential it is termed Inhibitory Post-synaptic Potential (IPSP) [23]. The whole process of the synapse takes place in a finite time which represents a time scale to be included in the mathematical formulation of a system of interacting neurons (neural networks). Simpler formulation of the interaction of LIF neurons, where the synaptic time scale is neglected, and the Post-Synaptic Potentials are assumed to be described by δ-functions, permit a simpler analytic (and numerical) treatment, but it over-simplifies important features that may arise as a consequence of synaptic dynamics [24, 25, 26, 27]. We will address this issue by considering the LIF neurons coupled via α-shaped pulses which captures some of the realistic aspects of synaptic dynamics (see Fig. 1.2), and such description will be maintained throughout all this dissertation.

The final aim of modeling neural circuits is to mimic the different phenomena observed experimentally, explain the mechanisms underlying such observations, and hopefully provide some predictive strategies. Modeling should include the most important aspects of neural dynamics. However, it is also a trade-off between the inclusion of (too many) realistic aspects and the necessity to limit the

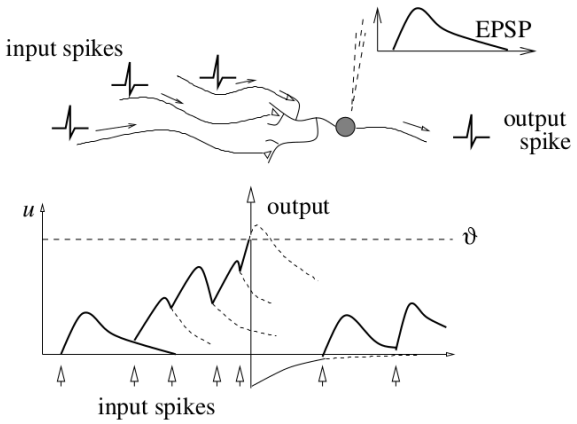

Figure 1.2: Scheme of neuronal interaction. At the top: Action potentials arrive to the neuron represented by the grey circle. At the synapse, the pre-synaptic signal is transformed into a post-synaptic potentials (in this case excitatory post-synaptic potential EPSP) with a prototypical shape of an α function. Bottom: Membrane potential (u) of the neuron in time. At each time of spike arrival the membrane potential integrates the EPSP increasing the value of u until it reaches the threshold value. Figure taken from [12].

number of parameters and variables entering in the model. Inevitably, this leads to the question: Can a simple/minimalist model such as the α-pulse coupled LIF network model account for biologically relevant applications? And if so, which are the structural properties of the model that allows for such biological significance? These two questions will be fundamental in our study. To answer them, we will present a detailed description of the role of several features of the α-LIF network in shaping collective emergent dynamics, and how these dynamics are compatible with experimental evidences.

Processing and coding of information in the brain necessarily imply the coordinated activity of large ensembles of neurons. Recent experiments in cognitive neuroscience have demonstrated how population related dynamical phenomena, such as information-carrying modulations of neural coherence, phase coding, etc. play a decisive role in the encoding and processing of information [28, 29]. A remarkable instance of population coding, whose study was awarded with the Nobel prize in 2014, is the encoding of the rat's position in the environment represented by Θ phase precession in hippocampal neuronal populations [28, 30, 31]. This and other evidences suggest that information is encoded in the population response, and therefore neuronal networks should be organized in a configuration that allow them to perform such encoding tasks. In this context connectivity between neurons plays a crucial role: A network set-up in which all neurons are connected to all the others (globally coupled) generates an extremely poor computation substrate to encode any type of input. In models of all-to-all pulse-coupled neural networks, the input encoding is trivialized as the response of the network converges to very regular (non-chaotic) states. For example, in the case of an homogeneous globally coupled neural network with excitatory feedback connections, the network syn-

chronizes completely for synapses with instantaneous rise time [32]or, in the case finite rise time synapses it may lead either to a partially synchronized regime or the so-called splay state [25]. Also, homogeneous globally coupled inhibitory neural networks are characterized by regular regimes: for very slow α synapses it has been demonstrated that inhibition produces synchronous firing [33], intermediate values of the time decay produces partial synchronization in the form of perfectly synchronized clusters of neurons [25, 27] and instantaneous rise time yields to splay states [25]. Although introducing heterogeneity either in the connection strength or neuron excitability may induce some irregularity (see for example [34, 35]), the states elicited in globally coupled systems are not very useful in terms of population coding, hence the need of topologies capable of realize more complex encoding strategies. This leads to a further characteristic ubiquitous in almost any neural circuit, and that is the *sparse* connection between neurons [36, 37]. From a biological perspective, a sparse network is one in which the number of synapses per neuron is much smaller than the total population. A sparsely connected network produces a sufficient heterogeneity to enhance the computational capabilities for population encoding. Sparseness and the role of connectivity in excitatory networks will be critically examined in chapter 2. Sparse networks will be consistently used during the discussion of the main chapters.

Sparse connectivity, however, is not a sufficient condition to generate non-trivial patterns in the response spiking activity [38]. It is widely known that spike trains recorded from cortical cells present a high variability in their spiking times [39]. This variability has been explained in terms of the *balanced* contribution of excitatory and inhibitory activity acting over a neuron [40, 41]. In few words, the excitatory feedback provided by pyramidal excitatory neurons is, on average, canceled out by the action of inhibitory interneurons. These two counteracting forces yield the neuron to have an average value of the membrane potential just below threshold. However, fluctuations of the balanced input persist and drive the neuron to fire in a seemingly stochastic way. For this reason, this type of behavior has been termed *fluctuation driven* regime, in opposition to the *mean driven* state where the excitatory input current prevails over inhibition and the neuron fires with low variability [21]. In chapter 3, the action of inhibitory synapses will be discussed, and a detailed comparison between mean driven and fluctuation driven networks will be carried out in terms of linear and non-linear stability analysis. The results will be analyzed in the context of experimental evidence reported for the rat's barrel cortex [42].

All these characteristics converge to form neuronal circuits capable of performing complex tasks. One of the most outstanding examples of the joint combination of these features is the encoding of cortico-thalamic input in the Basal Ganglia, through its main substructure, the *striatum*. The role of basal ganglia as an important locus for controlling motor functions [43], timing tasks [44] and reward based learning [45] has been widely studied both in behaving animals [46, 47] and *in-vitro* set ups [48, 49]. The striatum, the principal input of the basal ganglia conveying information from the cortex via excitatory cortico-striatal synapses, is mainly composed (around 90%) by GABAergic Medium Spiny Neurons (MSNs)

[50, 51]. At a topological level, the MSN circuitry appears as a sparsely connected network, in which the MSN form unidirectional collateral connections with a probability of connection between 10% - 25% [52, 53]. Studies *in vitro* have also shown that the collateral connections between MSN are *weak* [54, 55], in comparison to the Fast Spiking Neuron Synapses which also mediate the activity in the striatum [56]. A simple model accounting for the dynamical evolution of the striatum will be then introduced in chapter 4.

In searching for the answer to the relevance of simple network models in elucidating relevant neuro-physiological experimental results, this dissertation employs several disciplines: Through all the chapters, the results will be inspected from a nonlinear dynamics point of view, paying special attention to linear/non-linear stability analysis of the models that are presented. The aim is to present a methodical discussion on the possible role of chaos in shaping the studied dynamics. Furthermore, graph theory approaches will be applied, since the problems that will be analyzed concern random networks [57]. Also, in chapter 4, state of the art graph theory [58] will be used to deal with activity clusterization in neural ensembles. Finally, methods of statistical physics will be also applied, specially in chapter 2 through the reformulation of the deterministic dynamics of a sparse network via a noisy ensemble of globally coupled neurons.

Specifically, the dissertation is organized as follows: In chapter 2, we will consider pulse-coupled excitatory LIF neural networks with randomly distributed synaptic couplings. This random dilution induces fluctuations in the evolution of the macroscopic variables (corresponding to the local field potential measured by the EEG) and deterministic chaos at the microscopic (single neuron) level. Our main aim is to mimic the effect of the dilution as a noise source acting on the dynamics of a globally coupled non-chaotic system. Indeed, the evolution of a diluted neural network can be well approximated as a fully pulse coupled stochastic network, where each neuron is driven by a mean synaptic current plus additive noise. These terms represent the average and the fluctuations of the local field potential in the diluted system. The main microscopic and macroscopic dynamical features can be retrieved via this stochastic formulation. Furthermore, the microscopic stability of the diluted network can be also reproduced, as demonstrated from the almost coincidence of the measured Lyapunov exponents in the deterministic and stochastic cases for an ample range of system sizes. Our results strongly suggest that the fluctuations in the synaptic currents are responsible for the emergence of chaos in this class of pulse coupled networks.

A comparison in terms of stability analysis between excitatory and inhibitory sparse networks will be carried out in chapter 3. More specifically, we study the dynamical stability of pulse coupled networks of LIF neurons against infinitesimal and finite perturbations. In particular, we compare mean versus fluctuation driven networks, the former (latter) is realized by considering purely excitatory (inhibitory) sparse neural circuits. In the excitatory case the instabilities of the system can be completely captured by a standard linear stability (Lyapunov) analysis, whereas the inhibitory networks can display the coexistence of linear and

nonlinear instabilities. The nonlinear effects are associated to finite amplitude instabilities, which have been characterized in terms of suitable indicators. For inhibitory coupling one observes a transition from chaotic to non chaotic dynamics by increasing the synaptic time scale. For sufficiently fast synapses the evolution of the system remains erratic even though the system is linearly stable. This type of behavior is attributed to the *Stable Chaos* mechanism, in which linearly stable systems present seemingly chaotic behavior due to extremely long transients where firing occurs irregularly [59]. Although the stationary state is a stable attractor, the duration of such transients scales exponentially with the system size, therefore representing a quasi-stationary solution. In chapter 3, we demonstrate that the trajectories of the transient dynamics are destabilized by finite size perturbations, in agreement with a stable chaos picture of the underlying dynamics [60, 59].

In chapter 4, we propose a biologically inspired application of the the LIF network model coupled with inhibitory synapses to simulate the dynamics of MSNs in the striatum. Striatal projection neurons form a sparsely-connected inhibitory network, and this arrangement may be essential for the appropriate temporal organization of behavior. In this chapter we show that a sparse inhibitory network of artificial LIF neurons can reproduce key features of striatal population activity, as observed in brain slices [48]. In particular, we develop a new metric to determine the conditions under which sparse inhibitory networks display anti-correlated cell assembly dynamics, associated with highly variable firing rates of the individual neurons. We find that under these conditions the network displays an input-specific sequence of cell assembly switching, that effectively discriminates similar inputs. Our results support the proposal [*Ponzi and Wickens, PLoS Comp Biol* **9** *(2013) e1002954*] that GABAergic connections between striatal projection neurons allow stimulus-selective, temporally-extended sequential activation of cell assemblies. Furthermore, our results can help to show how altered intrastriatal GABAergic signaling may produce aberrant network-level information processing in disorders such as Parkinson's and Huntington's diseases.

The final chapter will be devoted to further discussion of the results and future perspectives. Finally, in appendix A we briefly present the computational approaches to integrate in an exact manner the evolution of our models, both in parallel and serially.

Chapter 2

Stochastic mean field formulation of the dynamics of diluted neural networks

2.1 Introduction

In pioneering studies devoted to excitatory pulse-coupled networks of leaky integrate-and-fire (LIF) neurons [61, 25], Abbott and van Vreeswiijk have shown that these models in a globally coupled configuration can exhibit only two kinds of evolution, both regular. The first one, termed splay state, is associated to collective asynchronous dynamics and the second one called partial synchronization (PS) corresponds to coherent periodic activity in the network. The latter regime is characterized by periodic oscillations in the neural activity and by quasi-periodic motions of the single neuron membrane potentials [25]. PS dynamics resembles the behaviour of developing brain networks, where synchronous population activity emerges in the form of Giant Depolarizing Potentials (GDPs), due to the excitatory action of the GABA neurotransmitter [62, 63]. The introduction of random dilution in a network with PS dynamics, achieved by considering an Erdös-Rényi distribution for the connectivity degrees, induces chaoticity in the system and fluctuations in the collective activity [64]. Fluctuations and chaos are due to the non equivalence of the neurons in the network. However, for *massively* connected networks, where the average in-degree is proportional to the system size [65], the dynamics becomes regular in the thermodynamic limit, recovering the evolution of the globally coupled system [64, 66]. On the other hand, for *sparse network*s, where the in-degree value is constant independently of the network size [65], the system remains chaotic even in the thermodynamic limit [67].

A fundamental question which we would like to address in this chapter is whether the effect of the frozen network heterogeneity can be reproduced in terms of a homogeneous model with additive noise. In particular, we are interested in reproducing the chaotic behavior observed in the diluted system. As homogeneous model we consider a fully coupled (FC) network displaying only regular motions and we focus on the PS regime, where the macroscopic variables are periodic [25]. The addition of noise to the membrane potential evolution induces irregular oscillations in the dynamics, observable both at the neuronal and at the macroscopic

level. To reproduce the dynamics of a specific deterministic diluted (DD) network, we employ as noise amplitudes in the stochastic model the ones measured in the original system. As a result, the stochastic model is able to mimic the main microscopic and macroscopic features of the original diluted system and even the chaoticity properties of the deterministic system. Furthermore, we are able to mimic the dynamics of networks composed by thousands of neurons by employing a stochastic model with only one hundred elements.

Previous studies have been devoted to the dynamical equivalence among the effect induced by noise on a system of identical excitable units and by quenched disorder in the model parameters (*diversity*) [68, 69]. In our analysis the diversity among neurons arises from the fact that each network element has a different (randomly chosen) set of connections. In particular, our study finds placement in the framework of the research works devoted to noise induced chaotic dynamics [70, 71, 72], however we are now dealing with a high dimensional system with a non trivial collective behavior. Furthermore, our approach, despite being developed for a simple network model, can be easily extended to a large class of complex networks.

The chapter is organized as follows, Sect. 2.2.1 is devoted to the introduction of the DD model as well as of dynamical indicators able to characterize microscopic and macroscopic dynamics in this system. In the same Subsection, the results concerning the dynamical evolution of deterministic FC and diluted networks are briefly revisited. In Sect. 2.2.2 the stochastic model developed to mimic the dynamics of the diluted system is introduced. Three methods to estimate the Lyapunov spectrum in pulse-coupled neural networks are revised in Sect. 2.3. In the same Section the three methods are compared by applying them to deterministic systems. Furthermore, the generalization of two of such methods to stochastic pulse-coupled networks with white and colored noise is also presented. Sect. 2.4.1 deals with the analysis of the reconstructions of the microscopic and macroscopic features of the DD network via the stochastic approach. The Lyapunov analysis for the stochastic models is reported in Sect. 2.4.2 and the results are compared with the ones obtained for the corresponding DD systems. Finally, a summary and a brief discussion of the obtained results is reported in Sect. 2.5 together with a sketch of possible future developments.

2.2 Models and Methods

2.2.1 Diluted Deterministic network

The Model

We will focus our study on a diluted network of N_D Leaky Integrate-and-Fire neurons (LIF). The membrane potential v_i of each neuron evolves according to the following first order differential equation

$$\dot{v}_i(t) = a - v_i(t) + gE_i(t) \qquad i = 1, \ldots, N_D \quad ; \tag{2.1}$$

where $a > 1$ represents a supra-threshold DC current and gE_i the synaptic current, with $g > 0$ being the excitatory synaptic coupling. Whenever the membrane potential of the i-th neuron reaches a fixed threshold $v_{th} = 1$, the neuron emits

a pulse $p(t)$ transmitted, without any delay, to all the post-synaptic neurons and its potential is reset to $v_R = 0$. In particular, the field $E_i(t)$ is given by the linear superposition of the pulses $p(t)$ received at the previous spike times $\{t_n\}$ by the i-th neuron from the pool of its pre-synaptic neurons. In this chapter, in analogy with previous studies [61, 25, 73], we assume that the transmitted pulse is an α-function, namely $p(t) = \alpha^2 t \exp(-\alpha t)$, where α^{-1} is the width of the pulse. In this case, the evolution of each field $E_i(t)$ is ruled by the following second order differential equation

$$\ddot{E}_i(t) + 2\alpha\dot{E}_i(t) + \alpha^2 E_i(t) = \frac{\alpha^2}{K} \sum_{n|t_n<t} C_{j,i}\delta(t - t_n) \quad ; \tag{2.2}$$

where $C_{j,i}$ is a $N_D \times N_D$ random matrix whose entries are 1 if there is a synaptic connection from neuron j to neuron i, and 0 otherwise and K is the number of pre-synaptic connections of the i-th neuron. For a FC network $K = N$ and all the fields are identical, since each neuron receives exactly the same sequence of spikes. By introducing the auxiliary variable $P_i \equiv \alpha E_i + \dot{E}_i$, the second order differential equation (2.2) can be rewritten as

$$\dot{E}_i = P_i - \alpha E_i, \qquad \dot{P}_i = -\alpha P_i + \frac{\alpha^2}{K} \sum_{n|t_n<t} C_{j,i}\delta(t - t_n) \; . \tag{2.3}$$

Therefore, the network evolution is ruled by the $3N_D$ Eqs. (2.1) and (2.3) which can be exactly integrated between spike events thus defining the following event driven map [74, 64]:

$$E_i(n+1) = E_i(n)\mathrm{e}^{-\alpha\tau(n)} + P_i(n)\tau(n)\mathrm{e}^{-\alpha\tau(n)} \tag{2.4a}$$

$$P_i(n+1) = P_i(n)\mathrm{e}^{-\alpha\tau(n)} + C_{m,i}\frac{\alpha^2}{K} \tag{2.4b}$$

$$v_i(n+1) = v_i(n)\mathrm{e}^{-\tau(n)} + a(1 - \mathrm{e}^{-\tau(n)}) + gH_i(n) \, . \tag{2.4c}$$

The m-th neuron is the next firing neuron, which will reach the threshold at time t_{n+1}, i.e. $v_m(n+1) \equiv 1$. One should notice that the event driven map is an exact rewriting of the continuous time evolution of the system evaluated in correspondence of the spike emissions, therefore it can be considered as a Poincaré section of the original flux in $3N_D$ dimension. Indeed the event driven map is $3N_D - 1$ dimensional, since the membrane potential of the firing neuron is always equal to one in correspondence of the firing event. Here, $\tau(n) = t_{n+1} - t_n$ is the time between two consecutive spikes, which can be determined by solving the implicit transcendental equation

$$\tau(n) = \ln\left[\frac{a - v_m(n)}{a + gH_m(n) - 1}\right] \; ; \tag{2.5}$$

where the expression $H_i(n)$ appearing in equations (2.4c) and (2.5) has the form

$$\begin{aligned} H_i(n) \;\; = \;\; & \frac{\mathrm{e}^{-\tau(n)} - \mathrm{e}^{-\alpha\tau(n)}}{\alpha - 1}\left(E_i(n) + \frac{P_i(n)}{\alpha - 1}\right) \\ & - \frac{\tau(n)\mathrm{e}^{-\alpha\tau(n)}}{(\alpha - 1)} P_i(n) \, . \end{aligned} \tag{2.6}$$

In this chapter, we consider connectivity matrices $C_{j,i}$ corresponding to random graphs with directed links and a fixed in-degree K for each neuron [75]. This amounts to have a δ-distribution centered at K for the in-degrees, and a binomial distribution with average K for the out-degrees. In particular, we examine massively connected networks, where the in-degree grows proportionally to the system size, namely our choice has been $K = 0.2 \times N_D$. As we have verified, the main results are not modified by considering Erdös-Rényi distributions with an average in-degree equal to K. A few tests are also devoted to the dynamics of sparse networks, in particular this has been done by maintaining the in-degree constant to $K = 100$ and by increasing the system size N_D up to 10,000.

Microscopic and Macroscopic Dynamical Indicators

In contrast to FC systems, the presence of dilution in the network induces fluctuations among the instantaneous values of the fields $\{E_i(t)\}$ [64, 66]. These fluctuations can be estimated by evaluating the instantaneous standard deviation $\sigma_E(t)$ of the individual fields $E_i(t)$ with respect to their instantaneous average value $\bar{E}(t)$, defined as follows

$$\bar{E}(t) = \frac{1}{N_D} \sum_{i=1}^{N_D} E_i(t) \tag{2.7}$$

$$\sigma_E(t) = \left[\frac{1}{N_D} \sum_{i=1}^{N_D} d_i(t)^2 \right]^{1/2} \quad ; \tag{2.8}$$

where $d_i(t) = E_i(t) - \bar{E}(t)$ denotes the instantaneous fluctuation of the i-th field with respect to their average over the network. Similarly we can define $\bar{P}$ and σ_P. Obviously, for a FC network $E_i \equiv \bar{E}$, $P_i \equiv \bar{P}$ and $\sigma_E = \sigma_P \equiv 0$. In the following, we will consider an unconstrained time average of the fluctuations $\langle \sigma_E \rangle$, as well as a conditional time average $\langle \sigma_E(\bar{E}, \bar{P}) \rangle$ evaluated whenever the value of the average fields falls within a box of dimension $\Delta\bar{E} \times \Delta\bar{P}$ centered at $(\bar{E}, \bar{P})$.

To measure the level of correlation present in the field fluctuations $d_i(t)$, we measure the associated autocorrelation function

$$C_E(\tau) = \frac{\left\langle \frac{1}{N_D} \sum_{i=1}^{N_D} d_i(t+\tau) d_i(t) \right\rangle}{\langle (\sigma_E(t))^2 \rangle} \, . \tag{2.9}$$

where $\langle \cdot \rangle$ indicates the average over time. The time interval over which the fluctuations are correlated can be estimated by measuring the decorrelation time τ_d from the the initial decay of $C_E(\tau)$.

The collective activity in the network can be studied by examining the macroscopic attractor in the $(\bar{E}, \bar{P})$-plane as well as the distributions of the average fields $F(\bar{E})$ and $F(\bar{P})$. On the other hand, the microscopic dynamics has been characterized by considering the distribution $F(ISI)$ of the single neuron inter-spike intervals (ISIs) as well as the associated first return map.

Diluted versus Fully Coupled Dynamics

As already mentioned in the Introduction, the dynamical regimes observable for FC LIF networks, with post-synaptic potentials represented as α-function, have

been analyzed in [61, 25]. These regimes are the so-called splay state and partial synchronization. The splay state is characterized by a constant value for the field E and by a perfectly periodic evolution of the single neurons, on the other hand in the PS regime, the common field reveals a perfectly periodic evolution, while the single neuron dynamics is quasi periodic [73]. In the present chapter we will focus in the latter regime, where collective oscillations in the network activity are present, in this case the macroscopic attractor corresponds to a closed curve in the two dimensional $(\bar{E}, \bar{P})$-plane. The introduction of random dilution in the system induces fluctuations d_i in the fields E_i with respect to their network average $\bar{E}$. Therefore the collective attractor still resembles a closed orbit, but it has now a finite width whose value depends on the values of $(\bar{E}, \bar{P})$ (see Fig. 2.1 (a)). As shown in Fig. 2.1 (b), the fluctuations d_i are approximately Gaussian distributed for any point $(\bar{E}, \bar{P})$ along the curve. Therefore, the d_i can be characterized in terms of their standard deviation $\langle \sigma_E \rangle$ averaged in time, this quantity, as previously shown in [64, 66], vanishes in the thermodynamic limit for massively connected networks. Indeed this is verified also in the present case as shown in Fig. 2.1 (c), thus indicating that for sufficiently large system sizes one recovers the regular motion observed for FC systems. It should be recalled that for sparse networks the fluctuations do not vanish, even for diverging system sizes [66]. Furthermore, the field fluctuations present a decorrelation time $\tau_c \simeq 0.1$, measured from the decay of the autocorrelation function $C_E(\tau)$ (see Fig. 2.1 (d)), which is essentially independent from the system size, as we have verified.

Another relevant aspect of the diluted system dynamics is that the random dilution of the links renders the finite network chaotic. In particular, for a massively connected network the system becomes regular in the thermodynamic limit, while a sparse network remains chaotic even for $N_D \to \infty$ [73]. This result suggests that the degree of chaoticity in the system is related to the amplitude of the fluctuations $d_i(t)$ of the macroscopic fields.

2.2.2 Fully Coupled Stochastic Network

The question that we would like to address is whether the dynamics of the DD network can be reproduced in terms of an equivalent FC network with additive stochastic terms. As a first approximation, we assume that the erratic dynamics of the DD system is essentially due to the field fluctuations $d_i(t)$. Therefore, we rewrote the dynamics of the diluted system as follows

$$\dot{E}(t) = P(t) - \alpha E(t) \tag{2.10a}$$

$$\dot{P}(t) = -\alpha P(t) + \frac{\alpha^2}{N_S} \sum_{n|t_n<t} \delta(t - t_n) \tag{2.10b}$$

$$\dot{v}_i(t) = a - v_i(t) + gE(t) + g\xi_i(t) \quad i = 1, \ldots, N_S \tag{2.10c}$$

where each neuron is driven by the same mean field term $E(t)$, generated by the spikes emitted by all the neurons, plus an additive stochastic term $\xi_i(t)$. Notice also that we use a different number of neurons in the reduced model $N_S < N_D$ since the asymptotic evolution of a FC system is fairly well retrieved already with a relatively small number of neurons. We will consider both white noise as well as

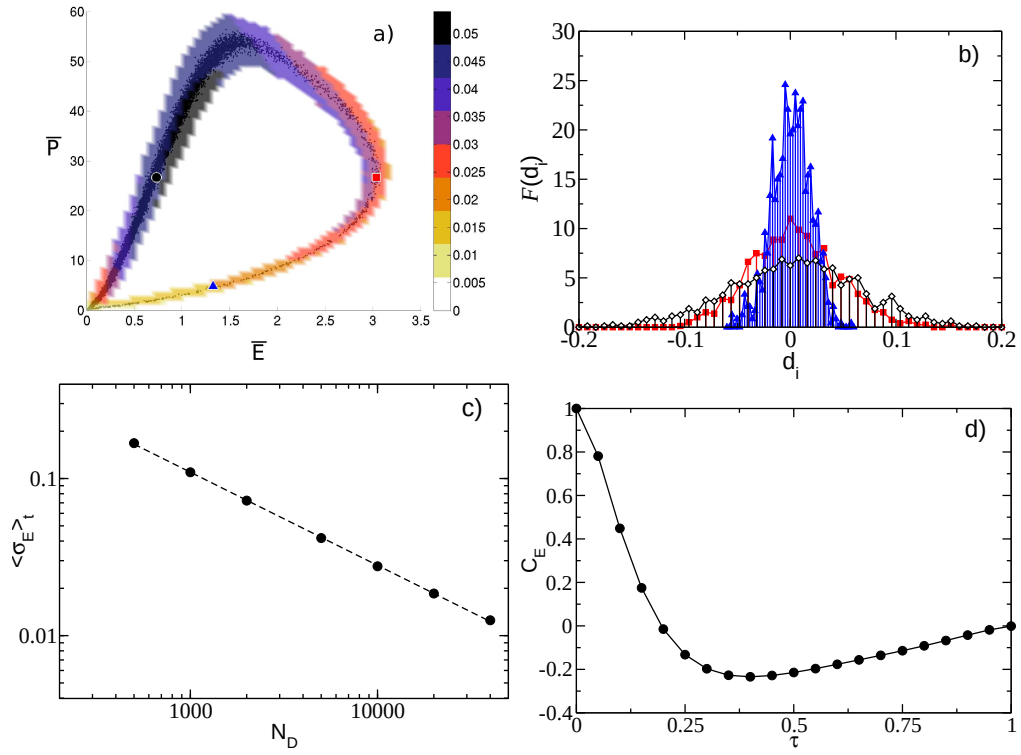

Figure 2.1: Characterization of the field fluctuations for a DD network. (a) Macroscopic attractor reported in the $(\bar{E}, \bar{P})$) plane (black dots), the colormap (superimposed on the attractor) quantifies the time averaged values of the fluctuations $< \sigma_E(\bar{E}, \bar{P}) >$. These are estimated over a grid 100×100 with resolution $\Delta\bar{E} = 0.06$ and $\Delta\bar{P} = 0.8$. (b) PDFs $F(d_i)$ of the deviation from the average field d_i estimated in three different points along the attractor. These points are indicated in panel (a) with the same symbol and color code. (c) Fluctuations of the fields $< \sigma_E >$ averaged both in time and all along the whole attractor as a function of the system size N_D (filled circles). The dashed line indicates a power law fitting to the data, namely $< \sigma_E > \propto N_D^{-0.6}$. (d) Autocorrelation function $C_E(\tau)$ of the fluctuations of the fields d_i. For all the reported data the parameters are fixed to $g = 0.5$, $\alpha = 9$, $a = 1.05$ and $K = 0.2N_D$. The system size is set to $N_D = 500$, apart in panel c). The reported quantities have been evaluated over $10^5 - 10^6$ spikes, after discarding an initial transient of 10^6 spikes.

colored one. In particular, for white Gaussian noise

$$\left\langle \xi_{w_i}(t)\xi_{w_j}(t')\right\rangle = \kappa^2\delta_{i,j}\delta(t-t') \tag{2.11}$$

with a zero average value, namely $\langle \xi_{w_i}\rangle = 0$. For colored noise, we considered exponentially time correlated noise as follows

$$\left\langle \xi_{OU_i}(t)\xi_{OU_j}(t')\right\rangle = \frac{\kappa^2}{2\tau_d}\delta_{i,j}\mathrm{e}^{-|\mathrm{t}-\mathrm{t}'|/\tau_\mathrm{d}} \tag{2.12}$$

where the average of the noise term is again zero. This is the so-called Ornstein-Uhlenbeck (OU) noise, which can be obtained by integrating the following ordinary differential equation

$$\dot{\xi}_{OU_i}(t) = -\frac{1}{\tau_d}\xi_{OU_i} + \frac{1}{\tau_d}\xi_{w_i} \tag{2.13}$$

where ξ_{w_i} is a Gaussian white noise, with the correlation defined in Eq. (2.11).

The main issue is to estimate the value of the noise amplitude κ to insert in Eqs. (2.11) and (2.12) and of the correlation time of the OU process τ_d to obtain a good reconstruction of the original dynamics. The latter parameter can be straightforwardly quantified from the autocorrelation function decay, in particular we set $\tau_d = \tau_c = 0.1$. For the former quantity, as a first attempt, we set κ equal to the time averaged standard deviation of the fields $\langle\sigma_E\rangle$. However, the quality of the reconstruction was not particularly good and this can be explained by the fact that the fluctuation amplitude is state dependent, as shown in Fig. 2.1 (b). Therefore, we evaluated $\langle\sigma_E(\bar{E},\bar{P})\rangle$ during simulations of DD systems and we employed these quantities in the stochastic integration of the FC system. In particular, we set $\kappa = \langle\sigma_E(E,P)\rangle$, where E and P are now the values of the fields obtained during the simulation of the FC stochastic system.

The integration of the SDEs (2.10) for the white and OU noise is performed as follows: The integration of the ODEs for the fields E and P can be performed without any approximation analogously to what done for the event driven map (2.4a) and (2.4b), since their evolution is completely deterministic. The integration of the equation for the membrane potential (2.10) is instead performed in two steps, first the deterministic part is integrated from time t to $t+h$ as

$$\mathcal{F}_i(v) = v_i(t)\mathrm{e}^{-h} + a(1-\mathrm{e}^{-h}) + gH(h) \quad . \tag{2.14}$$

Then the stochastic part is considered, for the white noise case, due to the linearity of the SDE the stochastic process can be integrated exactly [76], and the solution reads as

$$v_i(t+h) = \mathcal{F}_i(v) + \kappa\sqrt{\frac{1}{2}(1-\mathrm{e}^{-2h})}\eta_i(t) \quad . \tag{2.15}$$

Here, the stochastic variable $\eta_i(t)$ is a spatio-temporal uncorrelated random number, normally distributed with zero average and unitary variance.

For the colored noise, instead, the integration of the SDE with accuracy $\mathcal{O}[h^2]$ leads to the following set of equations [77]

$$\begin{aligned} \xi_{OU_i}(0) &= \tfrac{\kappa}{\sqrt{\tau_d}}\eta_i(0) \\ \xi_{OU_i}(t+h) &= \xi_{OU_i}(t)\mathrm{e}^{-h/\tau_d} + \kappa\sqrt{\tfrac{1-\mathrm{e}^{-2h/\tau_d}}{\tau_d}}\eta_i(t) \\ v_i(t+h) &= \mathcal{F}_i(v) + h\xi_{OU_i}(t) \ . \end{aligned} \tag{2.16}$$

The integration is performed with a constant time step $h \simeq 10^{-5} - 10^{-6}$. In particular, we integrate exactly the equations for the field variables E and P for a time interval h, while the membrane potential is evaluated employing the stochastic propagators reported in Eqs. (2.15) or (2.16), depending whether we consider white or OU noise. Whenever the membrane potential of one neuron overcomes threshold, we evaluate the crossing time t^* and the values of all the membrane potentials at t^* via a linear interpolation. We then restart the integration with the values of the field variables and of the membrane potentials evaluated at t^*, after resetting the potential of the neuron which has just fired.

We have performed the stochastic integration by employing extremely small time steps. Such a choice is not due requirements related to the the precision of the integration scheme (in particular in the white noise case the integration is exact), but to the fact that for the evolution of our system is crucial to detect the spike emissions with extremely accuracy. Therefore, instead of recurring to more elaborate integration schemes [76], we decided to use small integration time steps h in order to accurately determine the threshold crossing of the membrane potentials even in presence of noise.

2.3 Linear Stability Analysis

We are not only interested in the reconstruction of the macroscopic and microscopic dynamical features of the DD system via the stochastic approach, but also in the reproduction of the linear stability properties of the original model. The latter can be quantified in terms of the Lyapunov Spectrum $\{\lambda_i\}$, which can be related to the average growth rates of infinitesimal volumes in the tangent space. The Lyapunov spectrum has been estimated by considering the linearized evolution of the original system and by applying the usual procedure developed by Benettin et al. [78]. Therefore, let us start from the formulation of the linearized evolution of the DD case by differentiating (2.1) and (2.3), this reads as:

$$\delta\dot{E}_i = \delta E_i - \alpha\delta P_i \tag{2.17a}$$

$$\delta\dot{P}_i = -\alpha\delta P_i \tag{2.17b}$$

$$\delta\dot{v}_i = -\delta v_i + g\delta E_i \qquad i = 1, \ldots, N_D \qquad ; \tag{2.17c}$$

where $\{\delta E_i, \delta P_i, \delta v_i\}$ is a $3 \times N_D$ vector in the tangent space. In the following we will limit our analysis to the maximal non zero Lyapunov exponent λ_M.

It should be noted that two discontinuous events are present in the evolution of the original orbit: namely, the spike emission, which affects the field variables $\{P_i\}$, and the reset mechanism acting on the membrane potentials $\{v_i\}$. However, these discontinuities are not explicitly present in the Ordinary Differential Equations (ODEs) representing the tangent space evolution (2.17). In the next sub-sections we will report three different approaches on how to deal with these discontinuities in deterministic systems, and the possible extension to Stochastic Differential Equations (SDEs) for two of them. The first approach requires the formulation of the dynamics in terms of an exact event driven map so we do not see the possibility to extend it to stochastic systems. Instead, the other two methods concern the integration of ODEs with discontinuities and they can be easily extended to SDEs.

2.3.1 Linearization of the Event Driven Map (LEDM)

This approach can be applied whenever it is possible to write the evolution between two successive events in an exact manner, and the expression (even implicit) of the time interval $\tau(n)$ between two events is known. Here, we will focus on the method introduced in [74] for networks of pulse coupled LIF neurons. In this case it is possible to write explicitly the linearization of the event driven map by differentiating Eqs. (2.4), (2.5) and (2.6).

The linearized map reads as:

$$\begin{aligned}
\delta E_i(n+1) &= \mathrm{e}^{-\alpha\tau(n)}\left[\delta E_i(n) + \tau(n)\delta P_i(n)\right] \\
&\quad - \mathrm{e}^{-\alpha\tau(n)}\left[\alpha E_i(n) + (\alpha\tau(n)-1)P_i(n)\right]\delta\tau(n)\,, && \text{(2.18a)}\\
\delta P_i(n+1) &= \mathrm{e}^{-\alpha\tau(n)}\left[\delta P_i(n) - \alpha P_i(n)\delta\tau(n)\right]\,, && \text{(2.18b)}\\
\delta v_i(n+1) &= \mathrm{e}^{-\tau(n)}\left[\delta v_i(n) + (a - v_i(n))\delta\tau(n)\right] + g\delta H_i(n) \\
&\quad i = 1,\ldots,N_D \quad ; \quad \delta v_m(n+1) \equiv 0\,. && \text{(2.18c)}
\end{aligned}$$

where m is the index of the neuron firing at time t_{n+1}, while the condition $\delta v_m(n+1) \equiv 0$ is a consequence of the Poincaré section we are performing to derive the event driven map.

The evolution of the LEDM is completed by the expression for $\delta\tau(n)$:

$$\delta\tau(n) = \tau_v\delta v_m(n) + \tau_E\delta E_m(n) + \tau_P\delta P_m(n)\,, \tag{2.19}$$

where

$$\tau_v := \frac{\partial\tau}{\partial v_m} \quad , \quad \tau_E := \frac{\partial\tau}{\partial E_m} \quad , \quad \tau_P := \frac{\partial\tau}{\partial P_m} \quad . \tag{2.20}$$

Further details regarding this method can be found in [64] for a DD system.

2.3.2 Müller-Dellago-Posch-Hoover (MDPH) Method

A well known method used for the calculation of Lyapunov exponents for discontinuous flows has been introduced in [79, 80] and it has been recently extended to integrate and fire neural models with refractory periods in [81] and to piece-wise linear models of spiking neurons [82]. Here we will present an application of this method to our DD neuronal model. The approach consists of integrating in parallel the linearized evolution (2.17) and the ODEs describing the evolution of the orbit, namely (2.1) and (2.3), until one of the neurons reaches threshold. At this point the tangent vector value should be updated, due to a discontinuous event, as explained below.

By following the notation used in [79], let us consider a dynamical system described by a flow equation $\dot{\mathbf{x}} = \mathbf{f_1}(\mathbf{x})$ with a discontinuity defined by some implicit equation in terms of the state variables $l(\mathbf{x}) = 0$. The evolution at the discontinuity is defined in terms of a function $\mathbf{g}(\mathbf{x})$ mapping the state of the system from the time immediately previous to the discontinuity to the one immediately after, i.e $\mathbf{x}_+ = \mathbf{g}(\mathbf{x}_-)$. Finally, let us assume that the dynamics after the discontinuity is ruled by a different flow equation, namely $\dot{\mathbf{x}} = \mathbf{f_2}(\mathbf{x})$.

In this way the evolution in the real space is perfectly defined, while the correction to the tangent space vector $\delta\mathbf{x}$, due to the discontinuity, can be expressed as follows

$$\delta\mathbf{x}_+ = \boldsymbol{G}(\boldsymbol{x}_-)\delta\boldsymbol{x}_- + [\boldsymbol{G}(\boldsymbol{x}_-)\boldsymbol{f_1}(\boldsymbol{x}_-) - \boldsymbol{f_2}(\boldsymbol{x}_+)]\,\delta t, \tag{2.21}$$

where, provided that specific solvability conditions are met [79]

$$\delta t = -\frac{\boldsymbol{L}(\boldsymbol{x}_-)\delta\boldsymbol{x}_-}{\boldsymbol{L}(\boldsymbol{x}_-)\boldsymbol{f_1}(\boldsymbol{x}_-)}. \tag{2.22}$$

The notation $\mathbf{x}_-$ ($\mathbf{x}_+$) indicates the state of the system right in the moment t^* of reaching the discontinuity (just after t^*). Moreover,

$$\mathbf{L}(\mathbf{x}) = \frac{\partial l(\mathbf{x})}{\partial \mathbf{x}} \qquad \mathbf{G}(\mathbf{x}) = \frac{\partial \mathbf{g}(\mathbf{x})}{\partial \mathbf{x}}\ .$$

It is easy to show that for our DD system the flux is given by

$$\mathbf{f_1}(\mathbf{x}) = \mathbf{f_2}(\mathbf{x}) = [\dot{\mathbf{E}}, \dot{\mathbf{P}}, \dot{\mathbf{v}}] \quad ,$$

and the map at the discontinuity reads as

$$\begin{aligned}\mathbf{g}(\mathbf{x}) &= [E_{1_+}, E_{2_+}, ..., P_{1_+}, P_{2_+}, ..., v_{1_+}, v_{2_+}, ..., v_{m_+}, ...] \\ &= [E_{1_-}, E_{2_-}, ..., P_{1_-} + \frac{\alpha^2}{K}C_{m,1}, P_{2_-} + \frac{\alpha^2}{K}C_{m,2}, ..., \\ &\quad v_{1_+}, v_{2_-}, ..., 0, ...]\,,\end{aligned} \tag{2.23}$$

where m indicates the neuron firing at time t^*. Furthermore, the firing condition can be expressed as the scalar function

$$l(\mathbf{x}) = v_m - 1\,.$$

Therefore, a straightforward calculation gives us the corrections to perform in the tangent space to take into account the firing event at time t^*:

$$\delta E_{i_+} = \delta E_{i_-} - C_{m,i}\frac{\alpha^2}{K}\delta t\,, \tag{2.24a}$$

$$\delta P_{i_+} = \delta P_{i_-} + C_{m,i}\frac{\alpha^3}{K}\delta t\,, \tag{2.24b}$$

$$\delta v_{m_+} = -\dot{v}_{m_+}\delta t\,, \tag{2.24c}$$

with

$$\delta t = -\frac{\delta v_{m_-}}{\dot{v}_{m_-}} \quad . \tag{2.25}$$

Here, δt is the (linear) correction to apply to the spike time of the reference orbit to obtain the firing time of the perturbed trajectory. This quantity can be evaluated from the linearization of the threshold condition $v_m = 1$, and this leads to the following expression

$$\delta t = -\frac{1}{\dot{v}_{m_-}}\left(\left.\frac{\partial v_m}{\partial E_m}\right|_- \delta E_{m_-} + \left.\frac{\partial v_m}{\partial P_m}\right|_- \delta P_{m_-}\right) \quad , \tag{2.26}$$

where all the quantities entering in the rhs of the above equation are evaluated exactly at the spiking time.

2.3.3 Olmi-Politi-Torcini (OPT) Method

Recently, another approach has been proposed to deal with the discontinuities occurring in the context of pulse-coupled neural networks [83]. In this context the dynamical evolution in the tangent space between two spike events is ruled by the $3 \times N_D$ ODEs reported in (2.17). Whenever a spike is emitted in the network the tangent space vector components should be updated as follows:

$$\delta E_{i_+} = \delta E_{i_-} + \dot{E}_{i_-} \delta t \,, \tag{2.27a}$$

$$\delta P_{i_+} = \delta P_{i_-} + \dot{P}_{i_-} \delta t \,, \tag{2.27b}$$

$$\delta v_{i_+} = \delta v_{i_-} + \dot{v}_{i_-} \delta t \,, \tag{2.27c}$$

where the expression for δt is reported in Eq. (2.25) and the corrective terms appearing in (2.27) account for the difference in the spiking times of the perturbed and unperturbed orbit. It is clear that in this case, just after the firing event, the component of the tangent vector corresponding to the membrane potential of the firing neuron is exactly zero, i.e. $\delta v_{m_+} \equiv 0$. In this approach, the evolution in tangent space is still performed by taking into account the constraint due to the Poincaré section associated to the event driven map, meaning that this method is completely analogous to the LEDM.

2.3.4 Comparison of the Different Methods

In order to verify the agreement among the different approaches introduced above, we perform numerical estimation of the maximal non zero Lyapunov exponent by employing such methods for a FC deterministic network. In this case the system is never chaotic and in particular we consider two situations where the microscopic neuronal dynamics is either periodic or quasi-periodic. The first regime corresponds to the so-called splay state (observable for $\alpha = 3$ for the chosen parameters) and the latter one to the PS regime (observable for $\alpha = 9$). In both cases, it has been shown that the whole branch of the Lyapunov spectrum corresponding to the membrane potentials vanishes as $1/N^2$ in the thermodynamic limit [64]. In order to test for the accuracy of the employed methods, we decided to consider finite size networks, with $N_D = 50 - 200$, where the Lyapunov exponents are extremely small.

It is important to remember that the definition of the LEDM and OPT methods require a Poincaré section. Therefore, one degree of freedom, associated with the motion along the reference orbit, is removed from the dynamical evolution and also the corresponding zero Lyapunov exponent from the Lyapunov spectrum. Conversely, the MDPH method is not based on a Poincaré section. This means that, for a periodic motion the largest Lyapunov exponent, evaluated with LEDM and OPT methods, corresponds to the second Lyapunov exponent estimated with the MDPH. Similarly, when the neurons evolve quasi-periodically in time, the maximal non-zero Lyapunov exponent obtained with LEDM and OPT is the second one, while being the third one with the MDPH method. In summary, to test the accuracy of the algorithms we compare in the periodic (quasi-periodic) case, the second (third) Lyapunov exponent as obtained by the MDPH method with the first (second) one obtained with the other two methods. We measured these exponents

	$\alpha=3$, $g=0.4$, $a=1.3$, $K=N_D$				$\alpha=9$, $g=0.4$, $a=1.3$, $K=N_D$			
N_D	LEDM	OPT	MDPH	Max. Abs. Error	LEDM	OPT	MDPH	Max. Abs. Error
50	-1.70×10^{-4}	-1.67×10^{-4}	-1.70×10^{-4}	2.00×10^{-6}	-1.83×10^{-3}	-1.75×10^{-3}	-1.76×10^{-3}	5.17×10^{-5}
100	-4.25×10^{-5}	-4.30×10^{-5}	-4.38×10^{-5}	7.43×10^{-7}	-4.73×10^{-4}	-4.60×10^{-4}	-4.66×10^{-4}	6.87×10^{-6}
200	-1.07×10^{-5}	-1.14×10^{-5}	-9.10×10^{-6}	1.29×10^{-6}	-1.19×10^{-4}	-1.18×10^{-4}	-1.28×10^{-4}	5.87×10^{-6}
	$\alpha=3$, $g=0.5$, $a=1.05$, $K=0.2N_D$				$\alpha=9$, $g=0.5$, $a=1.05$, $K=0.2N_D$			
N_D	LEDM	OPT	MDPH	Max. Abs. Error	LEDM	OPT	MDPH	Max. Abs. Error
200	9.4676×10^{-3}	9.4676×10^{-3}	9.4608×10^{-3}	4.50×10^{-6}	2.9515×10^{-1}	2.9515×10^{-1}	2.9514×10^{-1}	6.67×10^{-6}

Table 2.1: Comparison of the maximal (non zero) Lyapunov exponents obtained with the three methods introduced in Sec. 2.3, namely Linearization of the Event Driven Map (LEDM), Olmi-Politi-Torcini (OPT) and Müller-Dellago-Posch-Hoover (MDPH) methods. Upper panel: For a deterministic FC network in the periodic splay state regime (left set of parameters), and in the quasi periodic PS regime (right set of parameters). Lower panel: For a chaotic DD network in the asynchronous regime (left set of parameters) and in the PS regime (right set of parameters). In all cases, the system is first relaxed through a transient of 10^4 spikes, after which the Lyapunov exponents are obtained by averaging over a period corresponding to $\simeq 10^7$ spike events. The reported errors are calculated as the maximal (absolute) difference between the average of the values obtained with the three methods and each single value. The MDPH and OPT estimates are obtained in the upper panel by integrating the system (2.4) with a fixed time step $h = 5 \times 10^{-6}$, while in the lower panel by employing an event driven integration scheme, where the time step is variable and given by (2.5).

for different system sizes, namely $N_D = 50$, 100 and 200. For all the considered parameter values and system sizes the agreement among the three methods is very good, the discrepancies among the different estimations are always of the order of $10^{-5} - 10^{-6}$, as reported in Table 2.1.

We also tested the three algorithms for a diluted deterministic system where the maximal Lyapunov exponent is definitely positive and its value is 2-3 orders of magnitude larger than the absolute values of the Lyapunov exponents measured in the non chaotic situations. In this case to improve the precision of the integration scheme, we employed an event driven technique, where the integration time step is variable and given by the solution of Eq. (2.5). This implementation allows to avoid the interpolations required to find the firing times when the integration schemes with a fixed time step are used. Also for the DD systems the discrepancies among the three methods are of order $10^{-5} - 10^{-6}$ (as shown in Table 2.1), thus suggesting that these differences are most probably due to the slow convergence of the Lyapunov exponents to their asymptotic value rather than to the precision of the numerical integration. Nonetheless, these results confirm that the three approaches are essentially equivalent for the analysis of deterministic systems.

2.3.5 Implementation for SDEs

Let us explain in detail how we implement the evolution in the tangent space associated to the SDEs Eqs. (2.10). For SDEs the estimation of the maximal Lyapunov exponent has been performed by employing the MDPH and the OPT methods, since the LEDM cannot be used in the case of a stochastic evolution, because it requires an exact knowledge of the next firing time. For white additive

noise, the linearized equations for both methods have exactly the same form and they coincide with the expression in absence of noise reported in (2.17). Notice that in this case we have a common field, therefore there are only two equations for the evolution of the infinitesimal perturbations $(\delta E, \delta P)$ of the field. The stochastic nature of the process is reflected only in the evolution of the reference orbit around which the linearization is performed. The only *approximation* we have done in this case is the same adopted during the integration of the real space. Namely, at each firing time the values of the membrane potentials (entering in the tangent space evolution) are simply evaluated as a linear interpolation between the values taken at the time step before and after the firing event and not by employing some accurate stochastic propagator taking in account the presence of absorbing boundaries [76].

In the case of OU noise the situation is more delicate, in particular the equations for the evolution of the common field correspond to Eqs. (2.17a) and (2.17b). On the other hand the linearized equations for the membrane potentials and the OU noise terms now read as

$$\delta \dot{v}_i = -\delta v_i + g\delta E + g\delta \xi_{OU_i} \tag{2.28a}$$

$$\delta \dot{\xi}_{OU_i} = -\frac{1}{\tau_d}\delta \xi_{OU_i} \qquad i = 1, \ldots, N_D \quad . \tag{2.28b}$$

It is easy to verify via (2.21) and (2.22) that the evolution of the Ornstein-Uhlenbeck process does not require extra corrections in correspondence of the firing events when the MDPH method is used, i.e $\delta \xi_{OU_{i+}} = \delta \xi_{OU_{i-}}$.

Instead, with the OPT approach each noise term $\delta \xi_{OU_i}$ should be updated whenever a neuron spikes as follows

$$\delta \xi_{OU_{i_+}} = \delta \xi_{OU_{i_-}} + \dot{\xi}_{OU_{i_-}} \delta t \tag{2.29}$$

and δt is now defined as

$$\delta t = -\frac{\delta v_{m_-}}{\dot{v}_{m_-}} = \tag{2.30}$$
$$\frac{-1}{\dot{v}_{m_-}} \left(\left.\frac{\partial v_m}{\partial E}\right|_- \delta E_- + \left.\frac{\partial v_m}{\partial P}\right|_- \delta P_- + \left.\frac{\partial v_m}{\partial \xi_{OU_m}}\right|_- \delta \xi_{OU_{m_-}} \right)$$

2.4 Results

In this Section we examine the quality of the reconstruction of the macroscopic and microscopic features and of the stability properties of the DD system in terms of SDEs representing a FC system subject to additive noise. In particular, we consider a massively connected DD network with $K = 0.2N_D$ for various system sizes. namely $500 \leq N_D \leq 10,000$. We reconstruct the dynamics of these systems by employing a small FC stochastic system of size $N_S = 100$, as we have verified that finite size effects are of limited relevance for FC systems. For each size of the DD system, we employ as noise amplitude in the stochastic FC system the standard deviation of the fluctuations of the corresponding DD fields. In particular, for the chosen set-up (massively connected) as the system size of the DD increases the amplitude of the fluctuations of the fields decreases, vanishing in the thermodynamic limit (as shown in Fig.2.1 (c)).

2.4.1 Macroscopic and Microscopic Dynamics

In order to test for the quality of the reconstruction of the macroscopic dynamics, we proceed to calculate the PDFs of the common field variables E and P in the FC set up, and compare them with the histograms of the average fields $\bar{E}$ and $\bar{P}$ as obtained in the DD case. These are reported in Fig. 2.2 (a-d) for two system sizes of the diluted system, namely $N_D = 500$ and $N_D = 5,000$. The agreement between the original PDFs and the reconstructed ones improve by passing from white to colored noise. In particular, this is evident for the $F(E)$, since in the case of white noise these distributions presents oscillations which are absent in the original ones. The origin of these oscillations can be ascribed to the fact that in presence of white noise of equal amplitude along the whole macroscopic orbit the field can be driven occasionally far from the original attractor.

When the colored noise is employed one observes a better overall reconstruction of the macroscopic attractors with respect to white noise. This is evident from Fig. 2.2 (e-f), the attractors obtained with OU noise show less deviations from the DD attractor with respect to the white noise case, in particular around the maximal $\bar{P}$. This is confirmed by considering the evolution in time of the original and reconstructed fields. The time traces of the fields are compared in Fig. 2.2 (g-h), by matching the time occurrence of the first maximum of each field. As one can see from the figure the OU reconstructed field follows reasonably well the original evolution, at least in the considered time window, while the field of the system driven by white noise shows, already after few oscillations period, a retard/advance with respect to the original one.

To render more quantitative this analysis, we have measured the average oscillation period of the field $\langle T_E \rangle$ for various system sizes N_D of the DD networks and for the corresponding stochastic reconstructions with white and OU noise. The results for all the considered system sizes are displayed in Fig. 2.2 (i). In the DD case $\langle T_E \rangle$ increases for increasing N_D and tends towards the corresponding deterministic FC value (dot-dashed line in the figure), this value will be reached in the thermodynamic limit, as expected [64]. Both the stochastic estimations slightly underestimate the DD value, however while the periods obtained by employing OU noise exhibit errors with respect to the DD values of the order $\simeq 0.4 - 0.9\%$, the errors made with the white noise reconstruction are usually larger, namely between 1.0 and 1.5%.

Let us now examine the microscopic dynamics of the DD system, this is quite peculiar for the chosen parameters, corresponding to quasi-periodic evolution of the membrane potentials of the single neurons. Indeed, the single neuron motion become exactly quasi-periodic only in the thermodynamic limit, where the regular FC dynamics is recovered. For DD systems, as the ones here examined, the neurons evolve on an almost quasi-periodic orbit, apart small chaotic fluctuations. These motions can be analyzed by considering the inter-spike-interval (ISI) of the single cell, in particular we will estimate the associated PDF $F(ISI)$ as well as the first return maps for the ISIs of the single neurons.

The distributions $F(ISI)$ are reported in Figs. 2.3(a) and 2.3(c) for the same level of dilution and two different system sizes, namely $N_D = 500$ and $N_D = 5,000$. The $F(ISI)$ are defined over a finite range of values, corresponding to the values taken by the ISIs during the neuron evolution. By increasing N_D, which

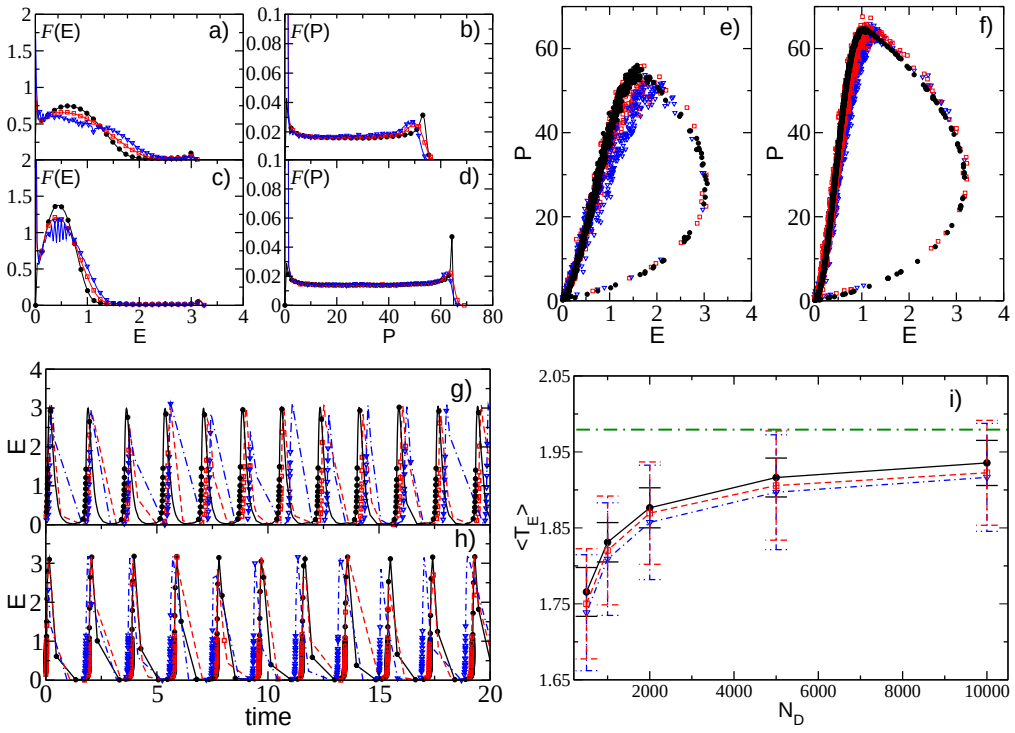

Figure 2.2: Reconstruction of the macroscopic dynamics of the DD system (black filled circles) in terms of white (blue empty triangles) and colored noise (red empty squares). (a-d) Histograms of the macroscopic fields E and P; (e-f) macroscopic attractors; (g-h) time traces of the field E; (i) average period of the field $\langle T_E \rangle$ as a function of the system size N_D of the DD system. Panels (a),(b),(e), and (g) refer to $N_D = 500$, while panels (c), (d), (f), and (h) to $N_D = 5,000$. In (g) and (h) the time traces have been shifted in order to ensure for the coincidence of the time of occurrence of the first maximum in each trace, also the colored (white) noise has been identified with a dashed (dashed-dotted) line, for the sake of visualization in (g), (h) and (i). The periods reported in (i) have been obtained by measuring the time lapse between two consecutive maxima, the number of samples used for the calculation of T_E is 5,000 data points, and the (green) dot-dashed line is the field period in a corresponding FC deterministic network equal to 1.98. Reconstructed dynamics have been obtained with $N_S = 100$ with an integration step $h = 5 \times 10^{-6}$. Other parameters are as in Fig. 2.1.

corresponds to have smaller fluctuations $\langle \sigma_E \rangle$, the $F(ISI)$ exhibit a sharper peak at large ISI and at the same time the return map appears to better approach a closed line, as expected for quasi-periodic motions (see Figs. 2.3(b) and 2.3(d)).

As far as the corresponding SDEs are concerned, the stochastic reconstruction is fairly good for the $F(ISI)$, despite the fact that the distributions are now covering a slightly wider range with respect to the original PDFs. The reconstructed return maps are *noisy* closed curves following closely the DD ones. By increasing N_D the reconstruction improves both with white and colored noise (as shown in Fig. 2.3(a-d)), however it is difficult to distinguish among the two approaches relying on these indicators. Therefore, we have measured the average ISI for different N_D in the DD case and for the corresponding stochastic dynamics. The results are reported in Fig. 2.3(e). In the DD case, the $\langle ISI \rangle$ increases with N_D approaching the FC deterministic limit (green dot dashed line in the figure). The reconstructed $\langle ISI \rangle$ are slightly under-estimating the deterministic results, however they reproduce quite closely the deterministic values. From the figure it is clear that the OU reconstruction represents a better approximation of the DD results for all the considered N_D, with errors ranging from 0.1 to 0.6%, with respect to the white noise results exhibiting discrepancies between $0.6 - 0.8\%$ with respect to the DD values.

From the analysis of the macroscopic and microscopic features we can conclude that the stochastic reconstruction improves by passing from white to Ornstein-Uhlenbeck noise. This is particularly evident for the field E. The reason for this can be understood by considering the evolution of the macroscopic field: E displays a rapid rising phase of duration $\simeq 0.1 - 0.2$ followed by a relaxation period $\simeq 0.9 \times T_E$ (as shown in Figs. 2.2(g) and 2.2(h)). Therefore, in order to properly reproduce this fast rise induced by the firing of the most part of the neurons in the network, the time correlation of the fluctuations (on a time scale $\tau_c \simeq 0.1$) should be taken into account.

We have also considered the so-called sparse limit, in particular we examined the DD networks obtained by fixing $K = 100$ and by increasing the system size from $N_D = 500$ to 10,000. As it can be appreciated from Fig. 2.4, the quality of the stochastic reconstruction obtained at the microscopic and macroscopic level is comparable with the one obtained for the massively connected networks. Thus suggesting that our approach holds also for extremely diluted systems.

On the other hand, we have verified that the proposed stochastic reconstruction fails whenever the system does not support a collective dynamical evolution, in the specific case this corresponds to partial synchronization. In fully coupled excitatory systems partial synchronization emerges only in a certain range of parameters, otherwise one observe asynchronous dynamics [25]. However, even within this range of parameters, the diluted system cannot sustain the collective motion if the average in-degree becomes too small [66, 67]. This is what happens also for the present choice of parameters for $K < 40$, notice that this critical connectivity is strongly dependent on the model parameters, but not on N_D whenever the system size becomes sufficiently large (for more details see Ref. [66]).

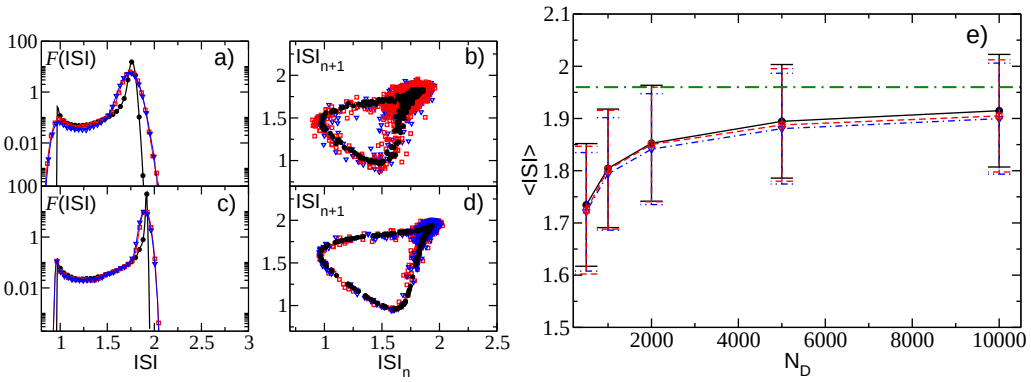

Figure 2.3: Reconstruction of the microscopic dynamics of the DD system (black filled circles) in terms of white (blue empty triangles) and colored noise (red empty squares). (a) and (c) PDF $F(ISI)$ of the ISIs, (b) and (d) ISIs return maps. Panels (a) and (b) refer to $N_D = 500$, while panels (c) and (d) to $N_D = 5,000$. (e) Average ISI as a function of the DD system size N_D, the thick (green) dot-dashed line refers to the asymptotic value of the average ISI in the corresponding FC deterministic set up, equal to 1.96 time units. Also the colored (white) noise has been identified with a dashed (dashed-dotted) line, for the sake of visualization in (e). The reconstructed dynamics are obtained with $N_S = 100$ by employing an integration step $h = 5 \times 10^{-6}$. The other parameters are as in Fig. 2.1

2.4.2 Lyapunov Exponents

As already mentioned, the system is chaotic for the DD system and the largest Lyapunov exponent vanishes in the thermodynamic limit following a power law decay with N_D [66]. In particular, in the considered case we observe a decay $\lambda_M \propto N^{-\gamma}$ with $\gamma \simeq 0.25$ (as shown in the inset of Fig. 2.5 (a)), which corresponds to a divergence of the maximal Lyapunov exponent with the averaged field fluctuations given by $\lambda_M \propto \langle \sigma_E \rangle^{0.43}$. On the other hand the FC deterministic counter-part exhibits a perfectly regular dynamics for any system size. Our aim is to reproduce the level of chaoticity present in the DD system by perturbing stochastically the FC system with noise terms whose amplitude corresponds to that of the fluctuations of the deterministic fields $\{E_i\}$, thus demonstrating that these fluctuations are at the origin of the chaotic behavior.

The maximal Lyapunov exponents in the DD case have been estimated by employing the LEDM method, while for the stochastic reconstructions we have used the MDPH and OPT methods with white and OU noise. As it is evident from Fig. 2.5 (a), the MDPH largely fails in reproducing the DD data, both for white and colored noise, apart for the smallest system size here considered (namely, $N_D = 500$) and white noise. On the other hand, the OPT approach works quite well both with white and OU noise over all the examined range of network sizes. The values obtained from the reconstructed dynamics are always larger than the DD values, but while in the OU case the error in the estimation increases with N_D and ranges from 2% at $N_D = 500$ to 13% at $N_D = 10,000$, for the SDEs with white noise the error is of the order of $\simeq 5 - 9\%$ and it seems not to depend on the considered system size. Furthermore, the OPT estimation of the maximal

Lyapunov exponent is able to recover the correct power law scaling with N_D, in particular in the white (OU) noise case we have found an exponent $\gamma \simeq 0.25$ ($\gamma \simeq 0.22$). The exponent found for the white noise reconstruction coincides with the deterministic value.

Furthermore, we have verified that for sparse networks all the considered stochastic reconstructions show that the maximal Lyapunov exponent saturates to a constant value in the thermodynamic limit (see Fig. 2.5 (b)). As expected due to the fact that the fluctuations of the fields remain essentially constant by increasing N_D, since $\langle \sigma_E \rangle \propto K^{-1/2}$ [73]. However, as it can be appreciated from Fig. 2.5 (b), the OPT estimation with OU noise provides in this case the best reconstruction of λ_M obtained for the DD system, with a maximal discrepancy of $\simeq 7$ % by fixing $K = 100$ and by varying $500 \leq N_D \leq 10,000$.

A possible explanation for the worse performances of the MDPH method with respect to the OPT one for the estimation of λ_M for a stochastic process with discontinuities relies on the definition and implementation of the method. As shown in Eq. (2.24c) and Eq. (2.25) the *corrections* to be applied at each firing event depends only on the value of the derivative of the membrane potential of the firing neuron estimate just before ($\dot{v}_{m_-}$) and after ($\dot{v}_{m_+}$) the event. These quantities depend on the actual value of the membrane potential at threshold and reset, as a matter of fact we have assumed that these values are not affected by noise. Maybe this assumption is too restrictive, however no better results have been obtained by the inclusion of stochastic terms. Instead, for the OPT approach the occurrence of a spike is taken into account by modifying the values of the linearized variables in the tangent space on the basis of the time derivatives of the corresponding variables (in the real space) evaluated just before the spike emission (see Eq. (2.27)). These time derivatives have been estimated as a linear interpolation between the values taken at the integration step immediately before and after the spike, therefore in their evaluation the stochastic evolution is somehow taken in account.

2.5 Final Summary

We have shown that the effect of the randomness in the distribution of the connections among neurons can be reproduced in terms of a perfectly regular (FC) network, where an additive noise term is introduced in the evolution equations for the membrane potentials. This suggests that either noise or dilution can lead to similar effects on the network dynamics (at least) in systems exhibiting collective oscillations. These results open new interesting directions for the study of the macroscopic activity of large sparse (neural) networks, which can be mimicked in terms of few collective noisy variables. Furthermore, our analysis has revealed that the stochastic approach is extremely convenient from a computational point of view, since it allows to mimic the dynamics of a deterministic system with $3 \times N_D$ variables by employing $N_S + 2$ variables, where $N_S = 100$, irrespectively of the size of the original network. We have also employed larger N_S, namely $N_S = 400$, without observing any substantial improvement with respect to the smaller size.

We have also discussed and critically re-examined the existing methods to evaluate Lyapunov exponents for deterministic dynamical models with discontinuities, and specifically for pulse-coupled systems. In particular, we have introduced

a novel method to estimate stochastic Lyapunov exponents for dynamical systems with discontinuities. Furthermore, we have applied this novel approach in order to give a convincing evidence that the fluctuations of the macroscopic variables acting on the membrane potentials are indeed responsible for the presence of chaotic activity in diluted networks of LIF excitatory neurons exhibiting collective oscillations. This is not obvious for any kind of LIF circuits, recent works [84, 85, 86, 87] have shown the existence of linearly stable dynamics in sparse inhibitory networks where the fluctuations of the currents are responsible for the irregular activity of the system, in absence of chaotic motion.

The approach presented here appears to work reasonably well in presence of collective oscillations in the macroscopic field (i.e. partial synchronization in the network), while we have verified that, when the global activity is asynchronous the reconstructions do not perform equally good. The origin of this discrepancy can be traced back to the fact that the fluctuations of the fields are, in the asynchronous situation, almost periodic with decorrelation times $\mathcal{O}(10^2)$. Such slow decorrelation demands for more refined treatment of the noise term, like e.g. by considering harmonic noise terms [88]. Furthermore, a higher fidelity is needed in the tangent space reconstruction since the maximal Lyapunov exponent is, in this case, two orders of magnitude smaller than for the PS dynamics.

Our approach can be considered a sort of *stochastic mean field* version of the original system, in this regard it should be mentioned that in recent works, the reconstruction of the dynamics of a diluted neural model quite similar to the one analyzed here, has been successfully attempted by employing a deterministic heterogeneous mean field (HMF) approach [89]. The HMF amounts to introduce mean field variables associated to equivalence classes of neurons with the same in-degree, but it still maintains the heterogeneous character of the diluted system, thus not allowing to clearly single out the source of the chaotic activity.

The results presented in this chapter have been published in reference [90].

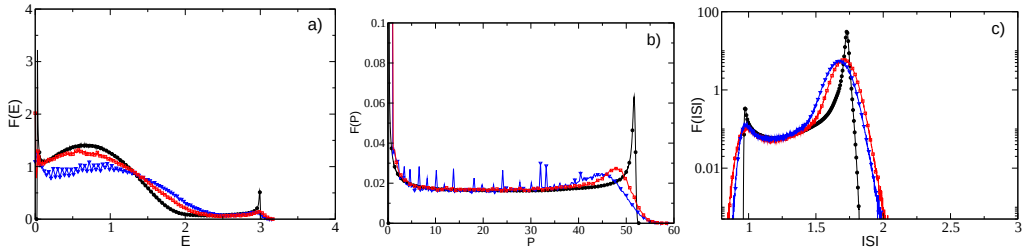

Figure 2.4: Reconstruction of the microscopic and macroscopic dynamics for a representative size of the DD system in the limit of large dilution. From left to right, reconstruction of the distributions of the instantaneous fields E, P and of the single-neuron ISIs. The considered DD network (black filled circles) has a size $N_D = 10,000$ and an in-degree $K = 100$, while the reconstructed dynamics, both for the white noise (blue empty triangles) and the colored noise (red empty squares) are obtained with $N_S = 100$, integrated with a step $h = 5 \times 10^{-6}$. Other parameters as in Fig. 2.1.

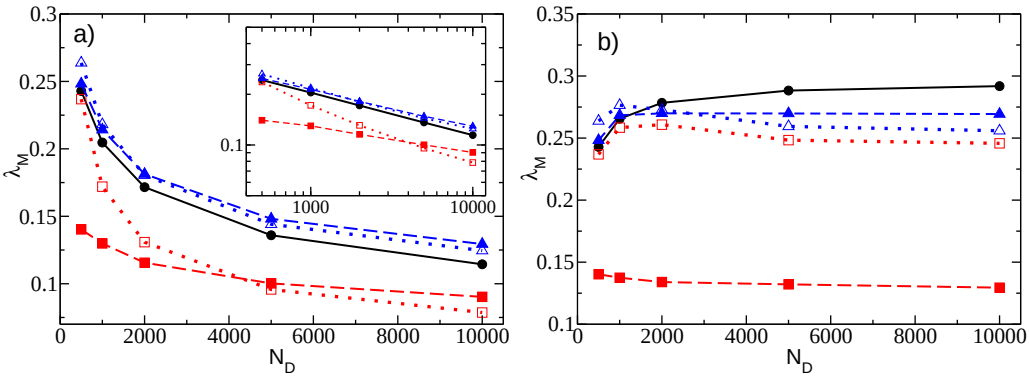

Figure 2.5: Maximal Lyapunov exponent λ_M as a function of the system size N_D for the DD case (black filled circles and solid line) and the corresponding stochastic reconstructions evaluated with the MDPH method (red squares) and the OPT approach (blue triangles). The stochastic results are reported for white (empty symbols and dotted lines) and Ornstein-Uhlenbeck (filled symbols and dashed lines) noise. In panel (a) we report the results for massively connected networks, where $K = 0.2 \times N_D$ and in (b) for sparse networks where $K = 100$ independent from the value of N_D. The inset of panel (a) shows in double logarithmic scale λ_M versus N_D for the massively connected networks. Reconstructed dynamics obtained with $N_S = 100$ and an integration step of $h = 5 \times 10^{-6}$. In all cases, the system is relaxed during a transient of 10^6 spikes and the Lyapunov exponents are calculated by integrating the tangent space for a period corresponding to $10^7 - 10^8$ spikes. Other parameters as in Fig. 2.1.

Chapter 3

Stable chaos in fluctuation driven neural circuits

3.1 Introduction

It is known that cortical neurons *in vivo* present a high discharge variability, even if stimulated by current injection, in comparison with neurons *in vitro* [91, 92]. In particular, these differences are peculiar of pyramidal neurons, while inter-neurons reveal a high neuronal firing variability in both settings [93]. This variability is usually measured in terms of the coefficient of variation CV of the single neuron inter-spike interval (ISI), defined as the normalized standard deviation of the ISI [94]. For cortical pyramidal neurons $CV \simeq 1.0$ *in vivo* [91] and $CV < 0.3$ *in vitro* [92], while for cortical inter-neurons $CV \simeq 1.0-1.2$ [93] in both settings. The variability of the spike emissions *in vivo* resembles a stochastic (Poissonian) process (where $CV = 1$), however the neural dynamics features cannot be accounted by simple stochastic models [91]. These phenomena can be instead modelized by considering a deterministically balanced network, where inhibitory and excitatory activity on average compensate one another [61, 40, 41, 95]. Despite the many papers devoted in the last two decades to this subject, it is still unclear which is the dynamical phenomenon responsible for the observed irregular dynamics [96, 20, 97, 19].

A few authors pointed out the possibility that *Stable Chaos* [59] could be intimately related to the dynamical behavior of balanced states [84, 85, 60, 98, 35, 86]. Stable chaos is a dynamical regime characterized by linear stability (i.e. the maximal Lyapunov exponent is negative), yet displaying an erratic behavior over time scales diverging exponentially with the system size. Stable chaos has been discovered in arrays of diffusively coupled discontinuous maps [99] and later observed also in inhibitory neural networks [84]. This phenomenon is due to the prevalence of nonlinear instabilities over the linear (stable) evolution of the system. This leads in diffusively coupled systems to propagation of information (driven by nonlinear effects) and in diluted inhibitory networks to abrupt changes in the firing order of the neurons [59].

Clear evidences of stable chaos have been reported in inhibitory δ–coupled networks by considering conductance based models [84] as well as current based models with time delay [85, 60, 98, 35]. In particular, these analyses focused on

the characterization of the time needed for the transient irregular dynamics to relax to the final stable state, the authors convincingly show that these transients diverge exponentially with the system size, a key feature of stable chaos. Furthermore, in [60, 98] it has been shown that, considering time extended post-synaptic pulses, a transition from stable to regular chaos is present, where fluctuation driven dynamics is apparently maintained [98].

In this chapter, we would like to compare the dynamics of a balanced network, whose dynamics is driven by fluctuations in the synaptic inputs, with neural networks composed of tonically firing neurons. Similar comparisons have been performed in some previous studies [100, 21], however here we would like to focus on the role of nonlinear instabilities and in particular on indicators capable of measuring finite amplitude instabilities in such networks. The effect of finite perturbations is relevant from the view point of neuroscience, where the analysis is usually performed at the level of spike trains, and a *minimal* perturbation corresponds to the removal or addition of a spike. This kind of perturbations can produce a detectable modification of the firing rate *in vivo* in the rat barrel cortex [42]. This has been reported as the first experimental demonstration of the sensitivity of an intact network to perturbations *in vivo*, or equivalently of an erratic behavior in neural circuits. However, it is unclear whether this sensitivity should be associated to linear or nonlinear effects. In particular the authors in [42] considered a network composed of excitatory and inhibitory neurons, where an extra spike in the excitatory network is soon compensated by an extra spike in the inhibitory network, indicating a sort of balance in the activity of the studied neural circuit. The ability of a perturbed balanced network to restore rapidly the steady firing rate has been also discussed in [86] for a minimal model. Furthermore, Zillmer *et al.* [60] have shown that a finite perturbation in a stable regime can cause a divergence of the trajectories.

These latter numerical studies, together with the fact that the addition of an extra spike is clearly a finite perturbation from the point of view of dynamical systems, strongly demand for further experimental investigations to clarify whether the erratic behavior reported in [42] is due to infinitesimal or finite amplitude instabilities.

Even though all these findings are congruent with the nature of stable chaos [59], it must be noted that a careful characterization of this regime in neural networks in terms of finite amplitude indicators is still lacking. The only previous study examining this aspect in some detail concerns a purely inhibitory recurrent Leaky Integrate-and-Fire (LIF) neural network with an external excitatory drive, which can sustain balanced activity [86]. Starting from this analysis, which was limited to δ-pulses, we have considered an extension of the model to finite width pulses. Furthermore, we have characterized the linearized evolution via usual Lyapunov exponents and the nonlinear effects in terms of the response of the system to finite perturbations. This analysis has been performed by employing previously introduced indicators such as Finite Size Lyapunov Exponents (FSLEs) [101] or the probability that a finite perturbation can be (exponentially) expanded [86], and new indicators capable of capturing nonlinear instabilities.

3.2 Model and methods

In this chapter we will again consider a network of N Leaky Integrate-and-Fire (LIF) neurons, here rewritten for simplicity: The membrane potential v_i of the i-th neuron evolves as

$$\dot{v}_i(t) = a - v_i(t) + gE_i(t) \qquad i = 1, \cdots, N \quad , \tag{3.1}$$

where $a > 1$ is the supra-threshold neuronal excitability, and gE_i represents the synaptic current due to the pre-synaptic neurons projecting on the neuron i. Whenever a cell reaches the threshold value $v_{th} = 1$ a pulse is emitted instantaneously towards all the post-synaptic neurons, and its potential is reset to $v_r = 0$. The synaptic current gE_i is the superposition of the pre-synaptic pulses $p(t)$ received by the neuron i with synaptic strength g, therefore the expression of the field E_i reads as

$$E_i(t) = \frac{1}{K^\gamma} \sum_{j \neq i} \sum_{n|t_n<t} C_{ij} \Theta(t - t_n) p(t - t_n) \quad . \tag{3.2}$$

Here the sum extends to all the spikes emitted in the past in the network, $\Theta(t-t_n)$ is the Heaviside function and the parameter γ controls the scaling of the normalization factor with the number K of pre-synaptic neurons. Proper normalization ensures homeostatic synaptic inputs [102, 103]. The elements of the $N \times N$ connectivity matrix C_{ij} are one (zero) in presence (absence) of a connection from the pre-synaptic j-th neuron to the post-synaptic i-th one. In this chapter we limit our analysis to random sparse networks, where each neuron receives exactly K pre-synaptic connections and this number remains fixed for any system size N. The model appearing in Eqs. (3.1) and (3.2) is adimensional, and the transformation to physical units is discussed in chapter 4

Following [61], we assume that the pulses are α-functions, $p(t) = \alpha^2 t \exp(-\alpha t)$, in this case the dynamical evolution of the fields $E_i(t)$ is ruled by the following second order differential equation (ODE):

$$\ddot{E}_i(t) + 2\alpha \dot{E}_i(t) + \alpha^2 E_i(t) = \frac{\alpha^2}{K^\gamma} \sum_{j \neq i} \sum_{n|t_n<t} C_{ij} \delta(t - t_n) \qquad , \tag{3.3}$$

which can be conveniently rewritten as two first order ODEs, as

$$\dot{E}_i = P_i - \alpha E_i, \qquad \dot{P}_i = -\alpha P_i + \frac{\alpha^2}{K^\gamma} \sum_{j \neq i} \sum_{n|t_n<t} C_{ij} \delta(t - t_n) \; ; \tag{3.4}$$

by introducing the auxiliary field $P_i = \dot{E}_i - \alpha E_i$.

The equations (3.1) and (3.4) can be exactly integrated from the time $t = t_n$, just after the deliver of the n-th pulse, to time $t = t_{n+1}$ corresponding to the emission of the $(n+1)$-th spike, with the event driven map introduced in (2.4):

$$E_i(n+1) = E_i(n) \mathrm{e}^{-\alpha\tau(n)} + P_i(n)\tau(n)\mathrm{e}^{-\alpha\tau(n)} \tag{3.5a}$$

$$P_i(n+1) = P_i(n)\mathrm{e}^{-\alpha\tau(n)} + C_{im}\frac{\alpha^2}{K^\gamma} \tag{3.5b}$$

$$v_i(n+1) = v_i(n)\mathrm{e}^{-\tau(n)} + a(1 - \mathrm{e}^{-\tau(n)}) + gH_i(n)\,, \tag{3.5c}$$

where $\tau(n) = t_{n+1} - t_n$ is the inter-spike interval associated with two successive neuronal firing in the network, which can be determined by solving the transcendental equation

$$\tau(n) = \ln\left[\frac{a - v_m(n)}{a + gH_m(n) - 1}\right] , \tag{3.6}$$

here m identifies the neuron which will fire at time t_{n+1} by reaching the threshold value $v_m(n+1) = 1$.

The explicit expression for $H_i(n)$ appearing in equations (3.5c) and (3.6) is

$$H_i(n) = \frac{\mathrm{e}^{-\tau(n)} - e^{-\alpha\tau(n)}}{\alpha - 1}\left(E_i(n) + \frac{P_i(n)}{\alpha - 1}\right) - \frac{\tau(n)e^{-\alpha\tau(n)}}{\alpha - 1}P_i(n)\,. \tag{3.7}$$

The model is now rewritten as a discrete-time map with $3N - 1$ degrees of freedom, since one degree of freedom $v_m(n+1) = 1$, is lost due to the event driven procedure, which corresponds to perform a Poincaré section at any time a neuron fires.

Our analysis will be devoted to the study of sparse networks, this is, we will consider a constant number K of afferent synapses for each neuron, namely $K = 20$. Therefore, the normalization factor K^γ appearing in the definition of the pulse amplitude is somehow irrelevant, since here we limit the study to a specific value of the in-degree connectivity, without varying K. However, to compare with previous studies, we set $\gamma = 1$ for purely excitatory neurons, where $g > 0$, similarly to what done in [66, 67], and $\gamma = 1/2$ for purely inhibitory networks, where $g < 0$, following the normalization employed in [85, 98, 104, 86]. The reasons for these different scalings rely on the fact that in the excitatory case, the dynamics of the system are *mean driven* (i.e. all neurons are tonically firing even in the absence of coupling, being supra-threshold), therefore the synaptic input should be normalized with the number of afferent neurons to maintain an average homeostatic synaptic input [102, 103]. The situation is different in presence of inhibitory coupling, here the supra-threshold excitability of the single neuron can be *balanced* by the inhibitory synaptic currents, which maintains the neurons in the proximity of the firing threshold. In this case, the network dynamics are *fluctuation driven*, because the fluctuations in the synaptic inputs are responsible of the neuronal firing. In order to keep the amplitude of the fluctuations of the synaptic current constant, the normalization is now assumed proportional to the square root of the number of the synaptic inputs [97]. In the present analysis we have tuned the model parameters in order to be in a fluctuation driven regime whenever the inhibitory coupling is considered. In particular, we will study not only the dependence of the dynamics on the pulse shape, but also on the system size, while maintaining a constant number of incoming connections K. However, we will not assume that the excitatory external drive (in our case represented by the neuronal excitability a) will diverge proportionally to $\sqrt{K}$, as done in [105, 86], since we are not interested in the emergence of a *self-tuned* balanced state in the limit $K \to \infty$, for $1 \ll K \ll N$ [105, 86].

3.2.1 Linear Stability Analysis

To perform the linear stability analysis of the system, we follow the evolution of an infinitesimal perturbation in the tangent space, through the set of equations derived in (2.18)

$$\begin{aligned}
\delta E_i(n+1) &= \mathrm{e}^{-\alpha\tau(n)}\left[\delta E_i(n) + \tau(n)\delta P_i(n)\right] \\
&\quad - \mathrm{e}^{-\alpha\tau(n)}\left[\alpha E_i(n) + (\alpha\tau(n)-1)P_i(n)\right]\delta\tau(n)\,, \qquad (3.8a)\\
\delta P_i(n+1) &= \mathrm{e}^{-\alpha\tau(n)}\left[\delta P_i(n) - \alpha P_i(n)\delta\tau(n)\right]\,, \qquad (3.8b)\\
\delta v_i(n+1) &= \mathrm{e}^{-\tau(n)}\left[\delta v_i(n) + (a - v_i(n))\delta\tau(n)\right] + g\delta H_i(n) \\
i &= 1,\ldots,N \quad ; \quad \delta v_m(n+1) \equiv 0\,. \qquad (3.8c)
\end{aligned}$$

The boundary condition $\delta v_m(n+1) \equiv 0$ is a consequence of the event driven evolution. The expression of $\delta\tau(n)$ can be computed by differentiating (3.6) and (3.7)

$$\delta\tau(n) = \tau_v\delta v_m(n) + \tau_E\delta E_m(n) + \tau_P\delta P_m(n)\,, \qquad (3.9)$$

where

$$\tau_v := \frac{\partial\tau}{\partial v_m} \quad , \quad \tau_E := \frac{\partial\tau}{\partial E_m} \quad , \quad \tau_P := \frac{\partial\tau}{\partial P_m} \quad . \qquad (3.10)$$

In this chapter, we will limit to measure the maximal Lyapunov exponent λ_M to characterize the linear stability of the studied models. This is defined as the the average growth rate of the infinitesimal perturbation

$$\boldsymbol{\delta} = (\delta v_1 \ldots \delta v_N,\, \delta E_1 \ldots \delta E_N,\, \delta P_1 \ldots \delta P_N),$$

through the equation

$$\lambda_M = \lim_{t\to\infty}\frac{1}{t}\log\frac{\mid \boldsymbol{\delta}(t) \mid}{\mid \boldsymbol{\delta}_0 \mid} \quad , \qquad (3.11)$$

where $\boldsymbol{\delta}_0$ is the initial perturbation at time zero. The evolution of the perturbation $\boldsymbol{\delta}(t)$ has been followed by performing at regular time intervals the rescaling of its amplitude to avoid numerical artifacts, as detailed in [78]. Furthermore, since our system is time continuous one would expect to have always a zero Lyapunov exponent, which in fact is the maximal Lyapunov if the system is not chaotic. However, this does not apply to the event driven map because the evolution is based on a discrete time dynamics, where the motion along the orbit between two successive spikes is no more present due to the performed Poincaré section.

3.2.2 Finite Size Stability Analysis

Besides the characterization of the stability of infinitesimal perturbations, we are also interested in analyzing how a perturbation grows according to its amplitude. To perform this task several indicators have been introduced in the last years, ranging from *Finite Size Lyapunov Exponents* (FSLE) [101, 106, 107, 108] to the propagation velocity of finite perturbations [109]. FSLEs have been mainly employed to charaterize stable chaos in spatially extended systems [59] and Collective Chaos in globally coupled systems [110, 111, 24].

We have performed several tests using the usual FSLE definition [108]. In particular FSLE can be defined considering an unperturbed trajectory $\boldsymbol{x} = (v_1 \dots v_N,\, E_1 \dots E_N,\, P_1 \dots P_N)$ and a perturbed trajectory $\boldsymbol{x'} = (v'_1 \dots v'_N,\, E'_1 \dots E'_N,\, P'_1 \dots P'_N)$, obtained by randomly perturbing all the coordinates (both the fields E and P as well as the membrane potentials) of the generic configuration $\boldsymbol{x}$. In order to ensure that the dynamics of the trajectory $\boldsymbol{x'}$ will also occur on the attractor associated to the studied dynamics, we have considered extremely small initial perturbations $\Delta_0 = \Delta(0) \simeq 10^{-8} - 10^{-10}$ of the reference orbit. Furthermore, we have discarded an initial transient to allow $\boldsymbol{x'}$ to relax on the attactor. Then we follow the evolution of the two trajectories in time and measure their distance $\Delta(t) = \parallel \boldsymbol{x}(t) - \boldsymbol{x'}(t) \parallel$, by employing the absolute value norm, at fixed sampling time intervals $dt = 0.2$. Whenever $\Delta(t_k)$ crosses (for the first time) a series of exponentially spaced thresholds θ_k, where $\theta_k = r\theta_{k-1}$, the crossing times t_k are registered. After averaging the time separation between consecutive crossings over different pairs of trajectories, one obtains the FSLE [108, 101]

$$\lambda_F(\Delta(t_k)) = \frac{r}{\langle t_k - t_{k-1} \rangle}, \qquad \text{where} \quad \Delta(t_k) = \theta_k \qquad . \tag{3.12}$$

For small enough thresholds, one recovers the usual maximal Lyapunov exponent, while for large amplitudes, FSLE saturates to zero, since a perturbation cannot be larger than the size of the accessible phase-space. In the intermediate range, λ_F tells us how the growth of a perturbation is affected by nonlinearities. However, as a general remark, we have noticed that it is extremely difficult to get reliable results from the FSLE analysis. The reason is most likely due to the fact that the definition of λ_F relies on averaging different passage times through a threshold θ_k. Each passage time estimation is, in turn, based on single trajectory realization, where the distance $\Delta(t)$ presents huge fluctuations. These fluctuations can induce, within a single sampling time interval dt, the crossing of several thresholds. In order to overcome this problem, each single realization of the distance $\Delta(t)$ has been smoothed before estimating the corresponding passage time from one threshold to the next. Unfortunately, we realized that the results strongly depend on the smoothing procedure (mainly, on the chosen time window) and that the effect is particularly evident in the fluctuation driven case.

In light of the aforementioned issues, we decided to adopt different indicators rather than the FSLE, in order to investigate the growth rate of finite amplitude perturbations. In particular, an estimation of finite size stability can be measured defining the following indicator

$$D(\Delta(t)) = \frac{d \langle \log \Delta(t) \rangle}{dt} \ ; \tag{3.13}$$

where, analogously to the FSLE, the average $\langle \cdot \rangle$ is performed over many different pairs of trajectories with initial distances $\Delta_0 = \Delta(0) \simeq 10^{-8} - 10^{-10}$. In the limit $\Delta(t) \to 0$ we expect to recover the maximal Lyapunov exponent λ_M. As we will show, after a transient needed for the perturbed trajectory $\boldsymbol{x'}$ to relax to the attractor, $D(\Delta)$ measures effectively the maximal Lyapunov exponent. However, if nonlinear mechanisms are present $D(\Delta)$ can become larger than λ_M for finite amplitude perturbations. Analogously to the FSLE, for perturbations of the size

of the attractor the indicator $D(\Delta)$ decays towards zero due to the trajectory folding. In contrast to the FSLE, the indicator (3.13) has shown to be less affected by fluctuations, most likely because its definition is based on the averaged profile of the disturbance.

The studied models present discontinuities of $\mathcal{O}(1)$ in the membrane potentials v_i, due to the reset mechanisms, and of $\mathcal{O}(\alpha^2/K^\gamma)$ in the fields P_i, due to the pulse arrival. In order to reveal, without any ambiguity, the presence of nonlinear instabilities at finite amplitudes, for the estimation of the FSLE and of the indicator D we mainly limit our analysis to the continuous fields $\{E_i\}$. In particular, to characterize the finite amplitude instabilities, we consider the following distance between the perturbed and unperturbed orbits

$$\Delta^{(E)}(t) = \frac{1}{N}\sum_{i=1}^{N} |E_i(t) - E_i'(t)| \ . \tag{3.14}$$

In some cases we have also analyzed the distance $\Delta^{(v,E,P)}$ between all the variables associated to the unperturbed and perturbed state with a clear meaning of the adopted symbol.

Unfortunately, we cannot employ the previously given procedure to measure the indicator $D(\Delta)$ as well as the FSLE in the case of stable chaos, because when λ_M is negative, small perturbations are quickly damped. In this case, one is forced to employ larger perturbation to observe nonlinear instabilities, and to perform measurement over (short) finite times, to avoid folding effects. Therefore, there is no guarantee that the evolution of the perturbed orbit will sample the phase space accordingly to the natural invariant measure. In particular, we will use indicators that are quite similar to the ones introduced in [106, 112] to study stable chaos coupled map lattices. Specifically, we proceed as follow: we consider two orbits at an initial distance Δ_0 and we follow them for a time interval T, then we measure the amplitude of the perturbation at the final time, namely $\Delta(T)$. We rescale one of the two orbits to a distance Δ_0 from the other one, keeping the direction of the perturbation unchanged, and we repeat the procedure several times and for several values of Δ_0. Then, we estimate the finite amplitude growth rate, as

$$R_T(\Delta_0) = \frac{1}{T}\left\langle \log\frac{|\Delta(T)|}{|\Delta_0|}\right\rangle, \tag{3.15}$$

where the angular brackets denote the average over a sufficiently large number of repetitions. To allow the perturbed orbit to relax on the attractor, we initially perform $\simeq 10^3$ rescalings, which are not included in the final average. However, also this procedure does not guarantee that the attractor is always reached, in particular for very large perturbations. Furthermore, the perturbed dynamics is no more constrained to evolve along the tangent space associated to the event driven map. As a matter of fact, whenever $\lambda_M < 0$ the indicator $R_T(\Delta_0)$ converges to zero and not to the Lyapunov exponent associated to the discrete time map evolution.

Finally, following the analysis reported in [86], we consider the probability $P_\theta(\Delta_0)$ that a perturbation of amplitude Δ_0 induces an exponential separation between the reference and perturbed trajectory. In particular, we perturb the

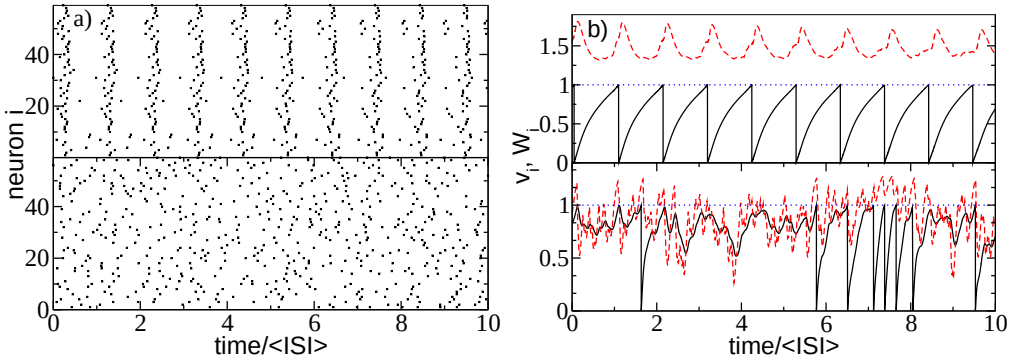

Figure 3.1: Comparison between mean driven (upper panels) and fluctuation driven (lower panels) activity. (a) Raster plots for a pool of 60 neurons. (b) Membrane potential traces $v_i(t)$ (black solid line) and the corresponding effective current W_i (red dashed line) for a typical neuron. The blue dotted line indicates the firing threshold. For the mean driven case, $a = 1.3$, $g = 0.2$, $\alpha = 9$ and $\gamma = 1$, corresponding to the situation studied in [67]; for the fluctuation driven network the parameters are the same, apart $g = -0.8$, $\alpha = 5$ and $\gamma = 1/2$. For both networks, $K = 20$ and $N = 400$ and the results for both systems are reported for the same *rescaled* time intervals $t/ < ISI >= 10$, after discarding a transient of 10^4 spikes.

reference orbit with an initial perturbation Δ_0 and we follow the evolution of the trajectories for a time span T. Whenever $\Delta(T)$ is larger than a certain threshold θ_L this trial contributes to the number of expanding initial perturbations $N_\theta(\Delta_0)$, otherwise is not counted. We repeat this procedure N_T times for each perturbation of amplitude Δ_0, then $P_\theta(\Delta_0) = N_\theta(\Delta_0)/N_T$. For the two latter indicators, namely R_T and P_θ, we have always employed the total distance $\Delta^{(v,E,P)}$, to confront our findings with the results reported in [86].

3.3 Results

As already mentioned, we will compare a mean driven excitatory network and a fluctuation driven inhibitory network. In particular, the excitatory network is studied in a regime where it presents a collective non trivial *partial synchronization* [25, 67]. This state is characterized by quasi-synchronous firing events, as revealed by the raster plot reported in the upper panel of Fig. 3.1(a), and almost periodic oscillations of the effective current $W_i(t) \equiv a+gE_i(t)$ (see Fig. 3.1(b), upper panel). In this particular case $W_i > 1$ therefore the neurons are always supra-threshold. In this situation the measure of the CV gives quite low values, namely for the studied case (with $a = 1.3$, $g = 0.2$ and $\alpha = 9$) $CV \simeq 0.17$, similar to pyramidal neurons in *vitro*. Despite this low level of variability in the neuronal dynamics, the sparseness in the matrix connectivity induces chaotic dynamics in the network, which persists even in the thermodynamic limit [67]. At variance with diluted networks, where the average connectivity scales proportionally to the system size ($K \propto N^z$, with $1 \geq z > 0$). In this latter case, in the limit $N \to \infty$ the system will recover a regular evolution, similarly to fully coupled networks [64, 66].

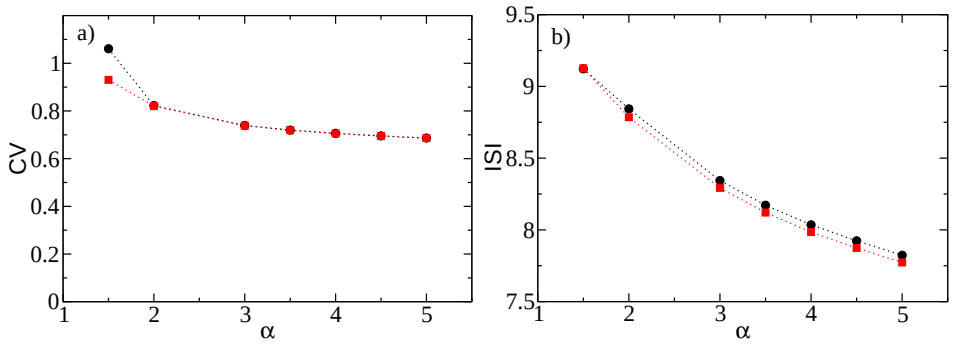

Figure 3.2: Dependence of the coefficient of variation CV (a) and of the inter-spike time interval ISI (b) on the pulse width for the fluctuation driven case. The data refer to $N = 400$ (black circles) and $N = 1600$ (red squares). The data have been averaged over 10^8 spikes, once a transient of 10^7 spikes has been discarder. The other parameters are as in the caption of Fig. 3.1

For the inhibitory network, we observe radically different dynamics, this because now $W_i(t)$ oscillates around one, therefore the neurons fire in a quite irregular manner, driven by the fluctuations of the fields $E_i(t)$, as shown in the lower panels of Figs. 3.1 (a) and (b). In this case we have examined the dynamics of the model for $a = 1.3$, $g = -0.8$ and different pulse-widths $1/\alpha$. For $\alpha \in [1 : 5]$ the neuronal dynamics are always quite erratic, being characterized by $CV \simeq 0.7 - 1$ (see Fig. 3.2(a)). Narrower pulses (larger α values) are associated to somehow more regular dynamics and smaller ISI, moreover we have verified that the ISI and CV saturates to some finite value in the thermodynamic limit (as shown in Fig. 3.3 (a) and (b)). This suggests that fluctuations will not vanish for $N \to \infty$ and that the system will remain fluctuation driven even in such a limit. Furthermore, the two α-values examined in Figs. 3.3(a) and 3.3(b) correspond to two different dynamical regimes, further discussed in Section 3.3.1, namely, a chaotic ($\alpha = 3$) and a non-chaotic ($\alpha = 5$) state.

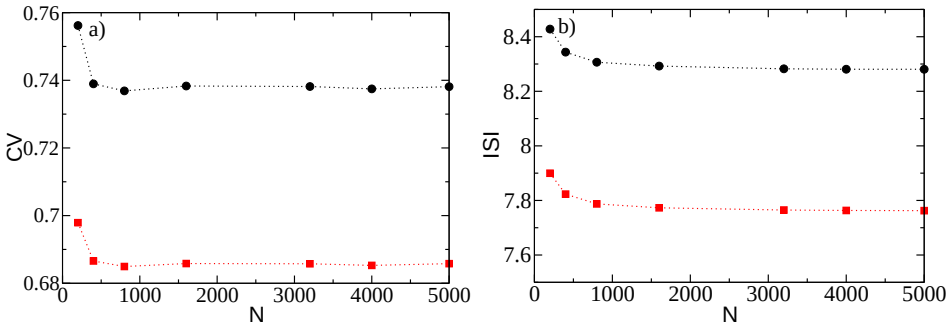

Figure 3.3: Dependence of the coefficient of variation CV (a) and of the inter-spike time interval ISI (b) on the size of the network for fluctuation driven networks in two representative situations corresponding to the chaotic ($\alpha = 3$, black circles) and the stable chaos ($\alpha = 5$, red squares) regimes. The reported data have been averaged over 10^8 spikes, once a transient of 10^7 spikes has been discarded. The other parameters are as in the caption of Fig. 3.1.

3.3.1 Lyapunov analysis

As previously shown, the fluctuation driven regime is observable for the inhibitory network for all the considered pulse widths. In this Subsection we would like to investigate whether such variability is related to a linear instability of infinitesimal perturbations (measured by the maximal Lyapunov exponent λ_M) or to other (nonlinear) instabilities present in the system. Let us start examining the Lyapunov exponent for such systems, as a first result we observe a strong dependence of λ_M on the pulse-width (see Fig. 3.4(a)): the system is chaotic for wide pulses and becomes stable for sufficiently narrow ones. These results are in agreement with previously reported results in [60, 98] for an inhibitory network of LIF neurons with delayed synapses. In these papers the authors show that chaos can arise only for sufficiently broad pulses, conversely for δ-pulses the system is always stable. It is worth to notice that the critical α-value at which occurs the transition to chaos becomes larger as the system size increases, pointing to the question whether the stable regime still exists for finite pulses in the thermodynamic limit or if it is merely a finite size property [98]. Extensive simulations for sizes of the network up to $N = 15,000$ have shown that the stable regime is present even for such a large size (see Fig.3.4(b)). Furthermore, we have found an empirical scaling law describing the increase of λ_M with N, i.e.

$$\lambda_M(N) = \lambda_\infty - cN^{-\eta} \tag{3.16}$$

where λ_∞ denotes the asymptotic value in the thermodynamic limit and η is the scaling exponent. For the two representative cases here studied, the exponents were quite similar, namely $\eta \simeq 0.24$ ($\eta \simeq 0.21$) for $\alpha = 3$ ($\alpha = 5$), however η depends definitely on the chosen parameters, indeed for $\alpha = 9$ the scaling exponent was $\eta \simeq 0.28$ (see inset). Furthermore, these exponents are different from the one measured for the mean driven case, in such situation for sparse connectivity λ_M converged to its asymptotic value as $1/N$ [67]. An exponent $\eta = 1$ has been previously measured for diffusively coupled map lattices exhibiting spatio-temporal chaos and theoretically justified in the framework of the Kardar-Parisi-Zhang equation [113]. The scalings we are reporting in this chapter are associated to random networks, therefore they demand for a new theoretical analysis. Furthermore, the asymptotic values $\lambda_\infty = 0.335(1)$ ($\lambda_\infty = -0.034(1)$) indicate that a critical threshold separating stable from chaotic dynamics persists in the thermodynamic limit.

3.3.2 Finite size perturbation analysis

Stable chaos in spatially extended systems is due to the propagation of finite amplitude perturbations, while infinitesimal ones are damped. In inhibitory neural networks, the origin of stable chaos has been ascribed to abrupt changes in the firing order of neurons induced by a discontinuity in the dynamical law, while infinitesimal perturbations leave the order unchanged [84, 59, 98]. In particular, by examining a conductance based model, in [59] it has been shown that a spike was able to induce a finite perturbation in the evolution of two (not-symmetrically) connected neurons, given that the inhibitory effect of a spike was related to the actual value of the membrane potential of the receiving neuron. Therefore two

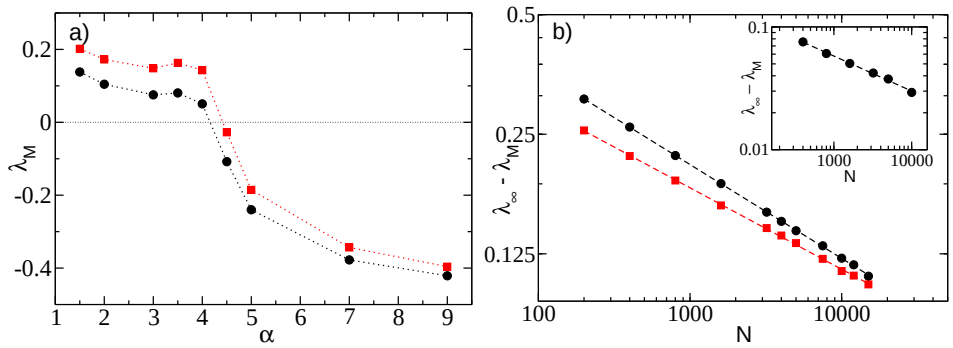

Figure 3.4: Linear stability analysis of the fluctuation driven state. (a) Maximal Lyapunov exponent λ_M as a function of pulse-width α, for two representative system sizes: $N = 400$ (black circles) and $N = 1600$ (red squares); thin dashed lines are drawn for eye guide only. (b) $\lambda_\infty - \lambda_M(N)$ as a function of the system size N in a double logarithmic scale for two representative pulse widths: $\alpha = 3$ (black circles) and $\alpha = 5$ (red squares). Thick dashed lines correspond to the nonlinear fitting (3.16), which predicts the asymptotic values λ_∞ (see text). The fitting parameters entering in Eq. (3.16) are $c = 1.07$ ($c = 0.75$) and $\eta \simeq 0.24$ ($\eta \simeq 0.21$) for $\alpha = 3$ ($\alpha = 5$). The inset illustrates that the law persists for even narrower pulses: for $\alpha = 9$, $\lambda_\infty = -0.3456(3)$ and $\eta = 0.28$. In both figures, λ_M is calculated by integrating the evolution in the tangent space together with the unperturbed orbit dynamics during a time interval equivalent to 10^8 spikes, after discarding a transient of 10^7 spikes. Remaining parameters as in Fig. 3.1.

ingredients are needed to observe stable chaos in neural models, a non symmetric coupling among neurons, together with the fact that the amplitude of the transmitted pulses should depend on the neuron state. These requirements are fulfilled also in the present model, since the effect of a spike received by neuron i (e.g. on delaying its next firing time) depends on its actual state (v_i, E_i, P_i) as shown in Eqs. (3.5) and (3.6). However, the problem is to quantify this effect in terms of some indicator, similarly to what done for spatially extended systems, where stable chaos has been characterized in terms of the FSLE and of the velocity of propagation of information [109, 112].

As a first indicator we consider the FSLE, associated with the norm $\Delta^{(E)}$, the corresponding results are reported in Fig. 3.5 for the mean and fluctuation driven cases. In the former case the FSLE is never larger than the usual Lyapunov exponent λ_M, with which it coincides over a wide range of perturbation amplitudes. In particular, $\lambda_F(\Delta^{(E)}) < \lambda_M$ for small amplitudes, due to the fact that initially the perturbation needs a finite time to align along the maximal expanding direction. Furthermore, due to the folding mechanism, the perturbation is contracted also for large perturbations of the order of the attractor system size. In summary, for mean driven dynamics only the instability associated to infinitesimal perturbations is present, as reported also in [24]. In the fluctuation driven case the situation is quite different as shown in Fig. 3.5, the FSLE essentially coincides with λ_M for small $\Delta^{(E)}$, but it becomes definitely larger than λ_M for finite perturbations, revealing a peak around $\Delta^{(E)} \simeq \mathcal{O}(1/N)$. These are clear indications

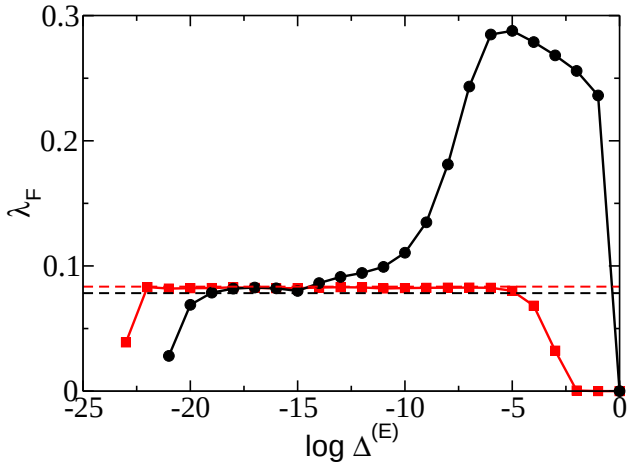

Figure 3.5: FSLE indicator λ_F for the fluctuation driven (black circles) and mean driven (red squares) chaotic set-ups. An initial perturbation of 10^{-9} (10^{-7}) is applied to the excitatory (inhibitory) network. The distance between the perturbed and unperturbed trajectory $\Delta^{(E)}$ is sampled during 300 time units, at fixed time intervals $dt = 0.2$. The sampled curve is smoothed over a sliding window of 20 time units and the resulting curve is used to obtain the times t_k at which the system crosses the corresponding thresholds θ_k, with $r = 1$ (see the definition (3.12)). This procedure is averaged in the mean (fluctuation) driven case over 5000 (15000) realizations. Thick dashed lines indicate the value of λ_M for each one of the two cases. The mean and fluctuation driven cases have been examined for the same parameter values reported in Fig. 3.1, apart that for the inhibitory case the inverse of the pulse width is set to $\alpha = 3$.

that finite amplitude instabilities coexist with infinitesimal ones and they could be in principle even more relevant.

The estimation of the FSLE, as already mentioned, suffers of several numerical problems in these systems. Therefore we decided to consider the indicator $D(\Delta^{(E)}(t))$, for simplicity denoted as $D^{(E)}$, which is less affected by the single orbit fluctuations, since its estimation is based on the time derivative of the averaged distance $\langle \log \Delta(t) \rangle$. In Fig. 3.6 we report $\left\langle \log \Delta^{(E)}(t) \right\rangle$ and $D^{(E)}$ as a function of time for a mean driven and a fluctuation driven case, in both situations after an initial transient, the indicator $D^{(E)}$ coincides with λ_M. However, in the mean driven case it coincides with λ_M for a very long time before decreasing due to the folding of the trajectories, while in the fluctuation driven situation it becomes soon larger than the maximal Lyapunov exponent and it shows a clear peak at finite amplitudes, before the folding effect sets in. The same results are reported in the upper panel of Fig. 3.7 as a function of $\left\langle \log \Delta^{(E)}(t) \right\rangle$, the peak in the fluctuations driven case is located around 4×10^{-4} thus at a smaller amplitude with respect to the FSLE, despite the system size and parameters are the same in both cases. Furthermore, in the lower panel in Fig. 3.7 we report the indicator $D(\Delta^{v,E,P}(t))$ ($D^{(v,E,P)}$ from now on) estimated for the total distance among the perturbed and unperturbed orbit. As expected, the discontinuities present in the evolution of the membrane potentials and of the auxiliary field P due to pulse emission and pulse

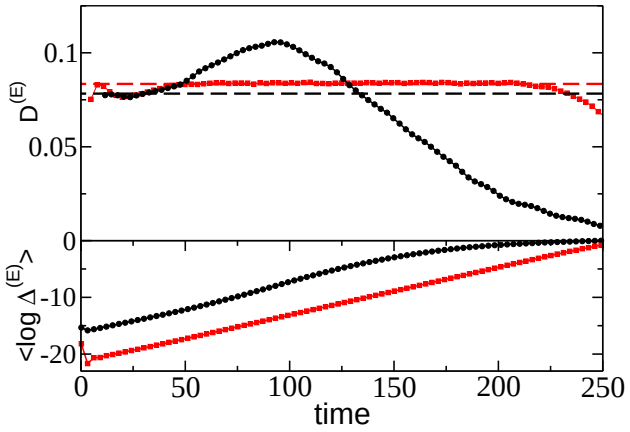

Figure 3.6: Lower panel: Evolution of the average distance $< \log \Delta^{(E)} >$ as a function of time, for the mean (red square) and the fluctuation (black circle) driven cases. The curves are obtained by averaging the distances between the perturbed and unperturbed trajectories over 5000 (15000) realizations, after applying an initial perturbation of $\mathcal{O}(10^{-8})$. Upper panel: Indicator $D^{(E)}$ as a function of time for the same cases, calculated as the time derivative of $< \log \Delta^{(E)} >$. For small perturbations, $D^{(E)}$ is close to λ_M (thick dashed lines), while observing a finite size effect in the fluctuation driven case. The mean and fluctuation driven cases have been examined for the same parameter values reported in Fig. 3.5.

arrival, induce a small increase on $D^{(v,E,P)}$ with respect to the infinitesimal value λ_M at finite amplitudes even in the mean driven case. However, in this case the peak of $D^{(v,E,P)}$ is definitely smaller with respect to the one observed in the fluctuation driven case and it is located at larger perturbations $\mathcal{O}(1)$. Similar effects are observable also by considering the FSLE associated to $\Delta^{(v,E,P)}$, data not shown. Nevertheless, in order to keep ourselves in a consistent framework, in what follows we will consider the distance between the perturbed and unperturbed continuous fields $\Delta^{(E)}$. By choosing this norm, we will avoid the presence of (trivial) peaks due to discontinuities as in the mean driven system, but instead, the presence of these peaks will be a genuine indication of nonlinear instabilities, as those present in a fluctuation driven regime.

The indicator $D^{(E)}$ is reported in Fig. 3.8 for various system sizes, ranging from $N = 400$ to $N = 1600$ for the mean and fluctuation driven cases. We observe that in the mean driven case $D^{(E)}$ always gives a value around the corresponding λ_M at all scales, apart the final saturation effect (see Fig. 3.8(a)). Notice that λ_M, for these system sizes, strongly depends on N (as shown in [67]), the saturation at the asymptotic value is expected to occur for $N > 5000$. For the fluctuation driven set-up, a peak (larger than λ_M) is always present in $D^{(E)}$ at finite amplitudes (see Fig. 3.8(b)). The peak broadens for increasing N extending to larger amplitudes and also its height increases. The presence of more neurons in the network renders stronger the finite amplitude effects, while nonlinear instabilities are present at larger and larger perturbation amplitudes.

So far we have considered only chaotic regimes, both in the fluctuation driven and in the mean driven case. However, even in linearly stable cases the dynamics

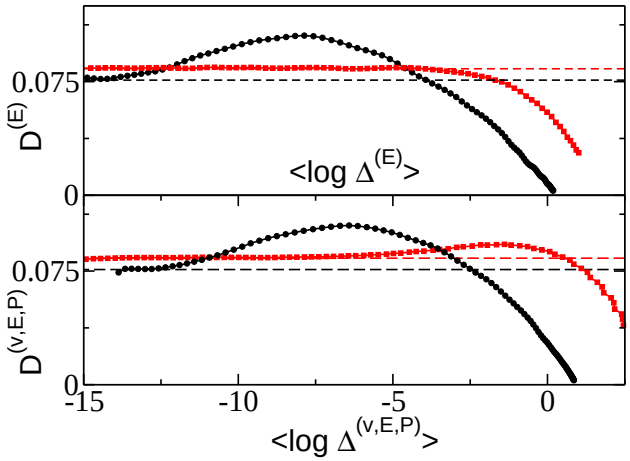

Figure 3.7: Indicator $D(\Delta)$ versus the complete distance $\Delta^{(v,E,P)}$ (lower panel) and versus the distance $\Delta^{(E)}$ (upper panel) for the mean (red squares) and fluctuation (black circles) driven cases. The curves are obtained with the same procedure described in the caption of Fig. 3.6. In both panels, thick dashed lines illustrate the corresponding value of λ_M. The mean and fluctuation driven cases have been examined for the same parameter values reported in Fig. 3.5.

can be erratic, as shown in Fig. 3.1 for the fluctuation driven case corresponding to $\alpha = 5$ for which the maximal Lyapunov is negative at any system size (see Fig. 3.4 (b)). This kind of erratic behavior, known as stable chaos [59], is one the most striking examples of dynamics driven by nonlinear effects, since the linear instabilities are asymptotically damped. In this situation neither the FSLE nor the indicator $D(\Delta)$ can be measured. The reason is that, in order to ensure that the dynamics will take place on the associated attractor, finite amplitude perturbations are reached only by starting from very small initial perturbations, which in this case are damped. Therefore, we should employ different indicators, namely the finite amplitude growth rate $R_T(\Delta_0)$ and the probability $P_\theta(\Delta_0)$.

As shown in Fig. 3.9(a), for the linearly stable fluctuation driven case corresponding to $\alpha = 5$, $R_T(\Delta_0) \to 0$ for sufficiently small perturbations, as expected. However $R_T(\Delta_0)$ becomes soon positive for finite amplitude perturbation and it reveals a large peak R_T^M located at an amplitude Δ_0^M. For increasing system size N, as shown in Fig. 3.10(a) a linear decrease of Δ_0^M with N is clearly observable, while R_T^M reveals a logarithmic increase with N. Thus suggesting that this indicator will diverge to infinity in the thermodynamic limit, similarly to the results previously reported in [105, 86]. However, at variance with these latter studies, in the present context the connectivity remains finite even in the limit $N \to \infty$.

The analysis of $P_\theta(\Delta_0)$, reported in Fig. 3.9(b), reveals that the curve can be well fitted as

$$P_\theta(\Delta_0) = 1 - \exp(-\Delta_0/\beta)^\mu \qquad ; \tag{3.17}$$

analogously to what done in [86]. The parameter β can be considered as a critical amplitude, setting the scale over which nonlinear instabilities take place. At variance with the results reported by Monteforte & Wolf in [86], we observe a linear decrease with N of the critical amplitude β (see Fig. 3.10(b)) and an exponent

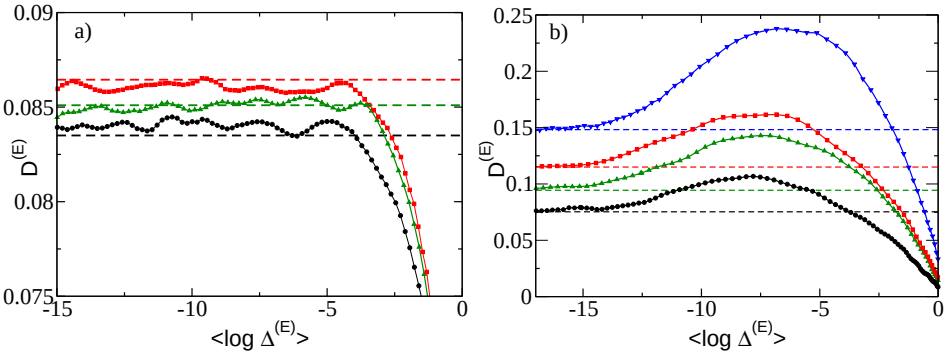

Figure 3.8: Finite amplitude perturbation analysis for several sizes of the network using the procedure described in Fig. 3.7 for the distance Δ^E for the mean (a) and fluctuation (b) driven setups. In both cases the studied sizes correspond to $N = 400$ (black circles), $N = 600$ (green up-triangles), $N = 800$ (red squares) and $N = 1600$ (blue down-triangles), averaged through 7500 realizations. Remaining parameters as in Fig. 3.5.

$\mu \simeq 2.3 - 2.5$, depending on the employed system size. Instead, Monteforte & Wolf reported a scaling $\beta \propto 1/\sqrt{N}$ and an exponent $\mu = 1$. Furthermore, we have verified for various continuous α pulses, with $\alpha \in [4; 7]$, that the measured exponent μ does not particularly depend on α. The model here studied differs for the shape of the post-synaptic currents from the one examined in [86], where δ-pulses have been considered.

In our opinion, these two latter indicators, R_T and P_θ bear essentially the same information: they measure the propensity of a perturbation Δ_0 to be amplified on a short time scale T. This is confirmed by the fact that (as shown in Fig. 3.10) the values of Δ_0^M and β, which set the relevant amplitude scales for the two indicators, both decrease with the same scaling law (namely, $1/N$) with the system size. A possible explanation for this scaling could be found by assuming that the main source of nonlinear amplification is associated to a spike removal (addition) in the perturbed orbit. A missing (extra) spike will perturb, to the leading order, the distance $\Delta^{(v,E,P)}$ by an amount $\propto \alpha^2\sqrt{K}/N$, since the lost (added) post-synaptic pulses are K each of amplitude $\alpha^2/\sqrt{K}$. This argument explains as well the logarithmic increase of R_T^M with the system size and the dependence of Δ_0^M with varying α as discussed in Fig. 3.11(b). Furthermore, the decrease of Δ_0^M and β with N seems to indicate that in the thermodynamic limit any perturbation, even infinitesimal, will be amplified. This is apparently in contradiction with the fact that the system is linearly stable and it appears to remain stable by increasing N (as shown in Fig. 3.4(b)). In systems exhibiting stable chaos, it has been reported many times the fact that the thermodynamic limit and the infinite time limit do not commute [99]. For finite system size, at sufficiently large times (diverging exponentially with N) a stable state is always recovered, while if the thermodynamic limit is taken before the infinite time one, the system will remain erratic at any time [59]. In the present case, it seems that a different non commutativity between the thermodynamic limit and the limit of vanishingly small perturbations is present, similar conclusions have been inferred

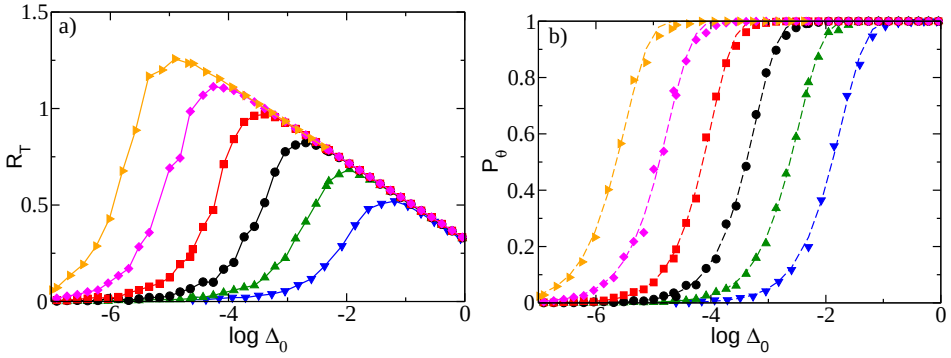

Figure 3.9: Characterization of the stable chaos regime: finite amplitude instabilities for different network sizes. (a) R_T indicator as a function of the initial perturbation Δ_0. (b) Probability P_θ to observe an exponential increase of the distance between a perturbed and an unperturbed orbit versus the initial perturbation Δ_0. Thick dashed lines refer to the fit to the data with the expression $P_\theta = 1 - e^{-(\Delta_0/\beta)^\mu}$. The studied sizes are $N = 100$ (blue down-triangle), $N = 200$ (green up-triangles), $N = 400$ (black circles), $N = 800$ (red squares), $N = 1600$ (magenta diamonds) and $N = 3200$ (orange right-triangles). For each perturbation Δ_0, R_T and P_θ are calculated after $T = 5$ time units, threshold defining expanding trajectories $\theta_L = -2$ and averaging over $N_T = 5000$ realizations. Remaining parameters as reported in Fig. 3.1.

also in [86]. Therefore, we can apparently conclude that a fluctuation driven system, which is linearly stable, but presents nonlinear instabilities, will become unstable at any amplitude and time scales in the thermodynamic limit. However, one should be extremely careful in deriving any conclusion from these indicators, since they are not dynamical invariant and their values depend not only on the considered variables, but also on the employed norm. This is due to the fact that growth rates associated to finite amplitude perturbations can be defined only over finite time lapses, due to the folding processes taking place on the attractor. Furthermore, in the present context there is an additional problem related to the meaningful definition of the norm in an infinite space, as that achieved in the thermodynamic limit.

To understand the differences between the indicator R_T and $D^{(E)}$, we have estimated R_T also in the chaotic fluctuation driven case, namely for $\alpha = 3$. Also in this case we observe that Δ_0^M will vanish for diverging system size, but with a different scaling law, namely $\Delta_0^M \simeq N^{-0.6}$. Furthermore, R_T^M increases with N, but this time it appears to saturate in the thermodynamic limit as $R_T^M = 3.09 - 5.60N^{-0.27}$, as shown in the inset of Fig. 3.10(a). Unlike the stable regime, in the chaotic one we cannot justify with the simple spike addition (removal) argument the scaling with N neither for Δ_0^M nor for R_T^M. It is highly probable that in this regime the interactions of the linear and nonlinear instabilities lead to more complicated mechanisms. The evolution of the indicator R_T suggests that for increasing N its peak will move down to smaller and smaller amplitude scale. However, this result is in contradiction with the behavior of $D^{(E)}$ reported in Fig. 3.8(b), for this latter indicator the position of the peak is not particularly

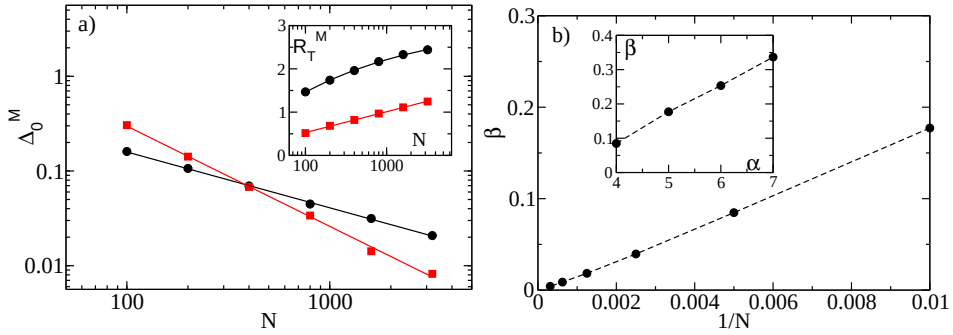

Figure 3.10: a) Peak position Δ_0^M as a function of N in a log-log scale for $\alpha = 3$ (black circles) and $\alpha = 5$ (red squares). The continuous line are the power law fittings $\Delta_0^M \propto N^{-\Phi}$, with exponents $\Phi = -0.59$ ($\Phi = -1.05$) for $\alpha = 3$ ($\alpha = 5$). Inset, maximum value of R_T as a function of the number of neurons in the network N in a log-lin scale. The solid lines refer to fittings of the data, namely $R_T^M = 3.09 - 5.60N^{-0.27}$ for $\alpha = 3$; $R_T^M = 0.23 + 0.28\log(N)$ for $\alpha = 5$. R_T calculated after a time span $T = 1$ ($T = 5$) for $\alpha = 3$ ($\alpha = 5$). b) Amplitude scale β associated to the indicator P_θ as a function of $1/N$. In the inset, β is reported as a function of α for parameter values associated to non chaotic dynamics. In the same range the exponent $\mu \sim 2.32$ (not shown). The model parameters refer to the fluctuation driven case studied in Fig. 3.1. Inset is obtained with $N = 100$

affected by N. In particular, finite amplitude instabilities affect larger and larger scales, contrary to what seen for R_T (see Fig. 3.9(a)). The same behavior is observable for $D^{(v,E,P)}$, data not shown. These contradictory results are probably due to the fact that while the indicator $D^{(E)}$ is based on a sampling of the phase space performed accordingly to the natural measure, the indicators R_T and P_θ can well be inconsistent with such measure. This is an unavoidable point when employing indicators based on short times and large perturbations.

Finally, in order to study the effect of the pulse shape on the finite amplitude behavior as measured by R_T, we proceeded to calculate this indicator for various α-values. As shown in Fig. 3.11, for increasing α (corresponding to narrower peaks) the position of the maximum Δ_0^M moves towards larger amplitudes. This effect can be explained by the fact that the maximal Lyapunov exponent decreases with α (as shown in Fig. 3.4(a)) and therefore perturbations of bigger and bigger amplitudes are required to destabilize the system for vanishingly pulse width. Consistently also the parameter β associated to P_θ increases for increasing α-values, as shown in the inset of Fig. 3.10 (b). Remarkably, the growth of the peak position for $N = 100$ obeys a quadratic power law (see Fig. 3.11 (b)), as expected from the previously reported argument concerning the spike addition (removal) that also explained the scaling of β and Δ_0^M with the system size. Unfortunately, for $N = 400$ where the states are chaotic for almost all the considered α-values, we cannot employ such argument, as previously explained, and indeed the scaling of of Δ_0^M with α is now slower than quadratic, namely $\Delta_0^M \propto \alpha^{1.67}$. Furthermore, from Fig. 3.11(a) it is also evident that the maximum of the indicator R_T^M grows with α. A possible explanation can be related to the fact that Δ_0^M can be considered as the initial perturbation needed to reach the *size of the attractor*, indeed for

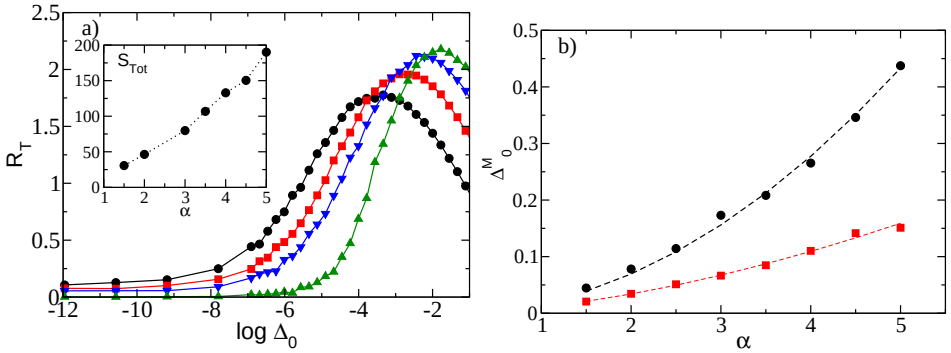

Figure 3.11: Finite size instabilities for fluctuation driven dynamics, for different pulse widths. (a) R_T as a function of the initial perturbation Δ_0, for $\alpha = 2$ (black circle), $\alpha = 3$ (red square), $\alpha = 4$ (blue down-triangle), $\alpha = 5$ (green up-triangle). The system size is fixed to $N = 400$. Inset, effective size of the attractor S_{Tot} as a function of α. (b) Peak location Δ_0^M as a function of α, for two sizes of the network: $N = 100$ (black circles) and $N = 400$ (red squares). The dashed lines correspond to the power law fitting $\Delta_0^M \propto \alpha^{\Phi}$, with exponents $\Phi = 2$ ($\Phi = 1.67$), for $N = 100$ ($N = 400$). R_T is calculated as described in the caption of Fig. 3.9. Remaining parameters as in Fig. 3.1.

$\Delta > \Delta_0^M$ the corresponding value of the indicator R_T decreases due to folding effects. Furthermore, as shown in the inset in Fig. 3.11(a), the size of the attractor, measured as $S_{Tot} = \sum \mid x_{max} - x_{min} \mid$, where $x = \{E_i, P_i, v_i\}$, increases with α. Therefore, the increase in R_T^M can be, to some extent, related to the enlargement of the attractor size with α.

3.4 Final Summary

We have investigated the dynamics and stability of mean and fluctuation driven neural networks, the former (latter) have been realized as a purely excitatory (inhibitory) pulse coupled network of leaky integrate-and-fire (LIF) neurons with a sparse architecture. In particular, we considered random networks with a constant in-degree $K = 20$ for any examined size.

The excitatory network, despite being chaotic, reveals a low spiking variability. On the other hand, in the fluctuation driven case the variability is high for any considered pulse width and system size (CV $\simeq 0.7 - 1.0$). However, a different picture arises when studying the stability of infinitesimal perturbations: the system is chaotic for slow synapses and it becomes stable for sufficiently fast synaptic times (≤ 4 ms). Furthermore, a chaotic state for the inhibitory network is observable already at small connectivity $K \sim O(10^1)$ contradicting what reported in [60], where the authors affirmed that a large connectivity is a prerequisite to observe chaotic motion in these models.

The maximal Lyapunov exponent λ_M tends towards an asymptotic value for increasing system sizes with a power-law scaling. The exponent η associated to this scaling is different in the two studied regimes, in particular $\eta \simeq 1$ for the mean driven set up [67], while, in the fluctuation driven case η present different

values according to the set of parameters chosen. The origin of the observed scaling demands for new theoretical analysis, similar to the one developed for spatio-temporal chaotic systems [113].

Remarkably, even in the linearly stable regime an erratic evolution of the network is observable. A similar phenomenon has been already observed in several systems ranging from diffusively coupled chaotic maps to neural networks, and it has been identified as stable chaos [59]. In this context, finite amplitude perturbations are responsible for the erratic behavior observed in the system. In diffusively coupled systems these nonlinear instabilities have been characterized in terms of the propagation velocity of the information and of suitable Finite Size Lyapunov Exponents (FSLEs) [109, 112]. FSLEs have been previously employed in the context of fully coupled neural networks, where they revealed that the origin of the chaotic motion observed in two symmetrical coupled neural populations was due to collective chaos in the mean-field variables driving the single LIF neurons [64]. In the context of randomly coupled systems the concept of propagation velocity on a lattice looses its sense, while FSLEs reveal serious problems in their numerical implementation.

However, FSLEs clearly show also in our case that in the mean driven case the observed instabilities have a purely linear origin, while in the fluctuation driven situation nonlinear mechanisms are present even when the system is chaotic. This analysis is confirmed by a novel indicator we have introduced, namely the local derivative $D(\Delta)$ of the averaged logarithmic distance $< \log \Delta >$ between the reference and the perturbed trajectory. This quantity suffers less than the FSLE the trial to trial fluctuations, since it is based on an averaged profile. For the fluctuation driven case this indicator is larger than the maximal Lyapunov exponent at finite amplitudes and this effect is present for all the examined system sizes. The position of the peak in $D(\Delta)$ seems not to be particularly influenced by the system size, while the peak itself broadens towards larger amplitudes for increasing N. Unfortunately, all these indications cannot tell us if the nonlinear mechanisms are prevailing on the linear ones, but just that the nonlinear effects are present. To measure the influence of linear versus nonlinear effects on the system dynamics, novel indicators are required, similar to linear and nonlinear information velocities for diffusively coupled systems [59].

As a final point we have studied nonlinear instabilities in linearly stable systems emerging in fluctuation driven inhibitory networks for sufficiently narrow postsynaptic currents. For the characterization of these instabilities we have employed the average finite amplitude growth rate $R_T(\Delta_0)$, measured after a finite time interval T, analogously to what what done in [106, 112], and the probability $P_\theta(\Delta_0)$ that an initial perturbation induces an exponential separation between the perturbed and the reference orbits, previously introduced in [86]. Both these indicators reveal the existence of instabilities associated to finite perturbations, in particular the characteristic amplitude scales associated to these indicators vanish in the thermodynamic limit as $1/N$. Thus suggesting that instabilities in these systems can occur even for infinitesimal perturbations in apparent contradiction with the fact that these systems are linearly stable at any system size, as revealed by the Lyapunov analysis. This contradiction has lead Monteforte & Wolf to conjecture in [86] that the thermodynamic limit and the limit of vanishingly small

perturbations do not commute in these models. Furthermore, we measure a logarithmic divergence with the system size of the peak height of $R_T(\Delta_0)$, suggesting that in the thermodynamic limit the value of these indicator will become infinite, similarly to what found in the high connectivity limit for a binary neuronal model in the balanced state [105] and for LIF with δ-pulses in [86]. However, in our study the connectivity remains finite and small in the limit $N \to \infty$.

Our opinion, based on the comparison of the indicators $D(\Delta)$ and $R_T(\Delta_0)$ performed in a fluctuation driven chaotic situation, is that the above results can be due to the fact that the dynamics considered for the estimation of $R_T(\Delta_0)$ and $P_\theta(\Delta_0)$ do not take place on the attractor of the system. This because the indicators are estimated at short times, without allowing the perturbed dynamics to relax onto the attractor. The development of new indicators is required to analyze more in depth the phenomenon of stable chaos in randomly connected networks.

The results presented in this chapter have been published in reference [87].

Chapter 4

Cell assembly dynamics of sparsely-connected inhibitory networks: a simple model for the collective activity of striatal projection neurons

4.1 Introduction

The basal ganglia are critical brain structures for behavioral control, whose organization has been highly conserved during vertebrate evolution [114]. Altered activity of the basal ganglia underlies a wide range of human neurological and psychiatric disorders, but the specific computations normally performed by these circuits remain elusive. The largest component of the basal ganglia is the striatum, which appears to have a key role in adaptive decision-making based on reinforcement history [115], and in behavioral timing on scales from tenths of seconds to tens of seconds [116].

The great majority ($> 90\%$) of striatal neurons are GABAergic medium spiny neurons (MSNs), which project to other basal ganglia structures but also make local collateral connections within striatum [50, 51]. These local connections were proposed in early theories to achieve action selection through strong winner-take-all lateral inhibition [117, 118], but this idea fell out of favor once it became clear that MSN connections are actually sparse (nearby connection probabilities $\simeq 10 - 25\%$ [52, 53]), unidirectional and relatively weak [54, 55]. Nonetheless, striatal networks are intrinsically capable of generating sequential patterns of cell activation, even in brain slice preparations without time-varying external inputs [48, 119]. Following previous experimental evidence that collateral inhibition can help organize MSN firing [120], an important recent set of modeling studies argued that the sparse connections between MSNs, though individually weak, can collectively mediate sequential switching between cell assemblies [121, 122]. It was further hypothesized that these connections may even be optimally configured for this purpose [123]. This proposal is of high potential significance, since sequential

dynamics may be central to the striatum's functional role in the organization and timing of behavioral output [124, 49].

In their work [121, 122, 123], Ponzi and Wickens used conductance-based model neurons (with persistent Na^+ and K^+ currents [16]), in proximity to a bifurcation from a stable fixed point to a tonic firing regime. We show here that networks based on simpler leaky integrate-and-fire (LIF) neurons can also exhibit sequences of cell assembly activation. This simpler model, together with a novel measure of structured bursting, allows us to more clearly identify the critical parameters needed to observe dynamics resembling that of the striatal MSN network. Among other results, we show that the duration of GABAergic post-synaptic currents is crucial for the network′s ability to discriminate different input patterns. A reduction of the post-synaptic time scale, analogous to that observed for IPSCs of MSNs in mouse models of Huntington's disease (HD) [125], leads in our model to alteration of single neuron and population dynamics typical of striatal dynamics in symptomatic HD mice [46]. Finally, we qualitatively replicate the observed response of striatal networks in brain slices to altered excitatory drive and to reduction of GABAergic transmission between axon collaterals of striatal neurons [48]. The latter effect can be induced by dopamine loss [126], therefore our results may help generate new insights into the aberrant activity patterns observed in Parkinson's disease (PD).

4.2 Models and Methods

4.2.1 The model

In this chapter we will consider a network of N LIF inhibitory neurons coupled via α pulses, described by the following set of equations

$$\dot{v}_i(t) = a_i - v(t) - gE_i(t) \tag{4.1a}$$

$$\dot{E}_i(t) = P_i(t) - \alpha E_i(t) \qquad i = 1, \dots, N \tag{4.1b}$$

$$\dot{P}_i(t) = -\alpha P_i(t) + \frac{\alpha^2}{K} \sum_{n|t_n<t} \mathcal{C}_{i,j}\delta(t - t_n)\,. \tag{4.1c}$$

The difference between the model used here and the ones introduced in chapters 2 and 3 is that the membrane potential of neuron i evolves according to different input currents a_i, selected from an uniform distribution. The evolution can be exactly integrated between time $t = t_n$, just after the deliver of the n-th pulse, to time $t = t_{n+1}$ corresponding to the emission of the $(n+1)$-th spike, through the event driven map introduced in Eqs. (2.4), (2.5) taking into account the specific value of external input for each cell i:

$$\tau(n) \;=\; \ln\left[\frac{a_i - v_m(n)}{a_i + gH_m(n) - 1}\right]\,, \tag{4.2}$$

where H_m has been derived in (2.6).

In this chapter we want to focus on a biologically inspired application, which lead us to rewrite the evolution equations in terms of dimensional variables. The membrane potential (4.1a) can be re-expressed as

$$\tau_m \dot{V}_i(\tilde{t}) = I_i - V_j(\tilde{t}) - \tau_m G \tilde{E}_i(\tilde{t}) \quad i = 1, \cdots, N \quad ; \tag{4.3}$$

where we have chosen $\tau_m = 10$ ms as the membrane time constant in agreement with the values reported in literature for MSNs in the up state in mice [127, 128, 129], I_i represents the neural excitability and the external stimulations, which takes in account the cortico-thalamic inputs received by the striatal network. Furthermore, $\tilde{t} = t \cdot \tau_m$, the field $\tilde{E}_i = E_i/\tau_m$ has the dimensionality of a frequency and G of a voltage. The currents $\{I_i\}$ have also the dimensionality of a voltage, since they include the membrane resistance.

For the other parameters/variables the transformation to physical units is simply given by

$$V_i = V_r + (V_{th} - V_r)V_i \tag{4.4}$$
$$I_i = V_r + (V_{th} - V_r)a_i \tag{4.5}$$
$$G = (V_{th} - V_r)g \tag{4.6}$$

where $V_r = -60$ mV, $V_{th} = -50$ mV. The isolated i-th LIF neuron is suprathreshold whenever $I_i > V_{th}$, however due to the inhibitory coupling the effective input is $W_i = I_i - \tau_m G \tilde{E}_i$. Therefore, the neuron is able to deliver a spike if $\langle W_i \rangle > V_{th}$ (in what follows, the symbol $\langle \cdot \rangle$ denotes the time average), in this case the firing of the neuron can be considered as mean-driven. However, even if $\langle W_i \rangle < V_{th}$, the neuron can be lead to fire from fluctuations in the effective input and the firing is in this case fluctuation-driven. It is clear that the fluctuations $\sigma(W_i)$ are directly proportional to the strength of the inhibitory coupling for constant external currents I_i.

For what concerns the PSPs the associated time constant is $\tau_\alpha = \tau_m/\alpha$, and the peak amplitude is given by

$$A_{PSP} = \frac{\alpha}{K} G e^{-1} = g \times 92 \ \mu V \quad ; \tag{4.7}$$

where the last equality allows for a direct transformation from adimensional units to dimensional ones, for the connectivity considered in this chapter, namely $K = 20$, and for $\alpha = 0.5$, which is the value mainly employed in our analysis. The experimentally measured peak amplitudes of the inhibitory PSPs for spiny projection neurons ranges from $\simeq 0.16 - 0.32$ mV [52] to $\simeq 1 - 2$ mV [130]. These values depend strongly on the measurements conditions, a renormalization of all the reported measurements nearby the firing threshold gives for the PSP peak $\simeq 0.17 - 0.34$ mV [54]. Therefore from Eq. (4.7) one can see that realistic values for A_{PSP} can be obtained in the range $g \in [2 : 10]$. For $\alpha = 0.5$ one gets $\tau_\alpha = 20$ ms, which is consistent with the PSPs duration and decay values reported in literature for inhibitory transmission among spiny neurons [52, 131]

Our model does not take in account the depolarizing effects of inhibitory PSPs for $V \leq E_{cl}$ [130]. The GABA neurotransmitter has a depolarizing effect in mature projection spiny neurons, however this depolarization does not lead to a direct excitation of the spiny neurons. Therefore our model can be considered as an effective model encompassing only the polarizing effects of the PSPs for $V > E_{cl}$. This is the reason why we have assumed that the membrane potential varies in the range $[-60 : -50]$ mV, since $E_{cl} \simeq -60$ mV and the threshold is $\simeq -50$ mV [130].

In the chapter we have always employed dimensional variables (for simplicity we neglect the tilde on the time variable), apart for the amplitude of the synaptic coupling, where we have found more convenient to use the adimensional quantity g.

4.2.2 Characterization of the firing activity

We define a neuron as active if it emits more than S_Θ spikes within the system evolution, which we typically take as the time taken for the network to evolve through to 10^7 spikes. The fraction of active neurons is denoted by the symbol n^* and is the ratio between N_{act}, the number of acitve neurons, and N the total number of neurons.

The characterization of the dynamics of the active neurons is performed via the coefficient of variation CV, the local coefficient of variation CV_2 and the zero lag cross-correlation matrix of the firing rates $C(\nu_i, \nu_j)$. The coefficient of variation associated to the i-th neuron is then defined as the ratio:

$$CV^{(i)} = \frac{\sigma(ISI^{(i)})}{\langle ISI^{(i)} \rangle} ;$$

where $\sigma(\cdot)$ denotes the standard deviation. The distribution of the coefficient of variation $F(CV)$ reported in the chapter refer to the values of the CV associated to all the active cells in the network.

Another useful measure of the spike statistics is the local coefficient of variation. For each neuron i and each spike emitted at time $t_n^{(i)}$ from the considered cell the local coefficient of variation is measured as

$$CV_2^{(i)}(n) = \frac{|ISI_n^{(i)} - ISI_{n-1}^{(i)}|}{ISI_n^{(i)} + ISI_{n-1}^{(i)}}$$

where the n-th inter-spike interval is defined as $ISI_n^{(i)} = t_n^{(i)} - t_{n-1}^{(i)}$. The above quantity clearly ranges between zero and one: a zero value corresponds to a perfectly periodic firing, while the value one is attained in the limit $ISI_n^{(i)}/ISI_{n-1}^{(i)} \to 0$ (or $ISI_n^{(i)}/ISI_{n-1}^{(i)} \to \infty$). The probability distribution function $F(CV_2)$ is then computed by employing the values of the $CV_2^{(i)}(n)$ for all the active cells of the network estimated at each firing event.

The level of correlated activity between firing rates is measured via the cross-correlation matrix $C(\nu_i, \nu_j)$. The firing rate $\nu_i(t)$ of each neuron i is calculated at regular intervals $\Delta T = 50$ ms by counting the number of spikes emitted in a time window of $10\Delta T = 500$ ms, starting from the considered time t. For each couple of neuron i and j the corresponding element of the $N \times N$ symmetric cross-correlation matrix $C(i, j)$ is simply the Pearson correlation coefficient measured as follows

$$C(i, j) = \frac{cov(\nu_i, \nu_j)}{\sigma(\nu_i)\sigma(\nu_j)} ,$$

where $cov(\nu_i, \nu_j)$ is the covariance between signals $\nu_i(t)$ and $\nu_j(t)$, which has been calculated for statistical consistency by employing always spike trains containing 10^7 events. This corresponds to time intervals T_E ranging from 50 s to 350 s (from 90 s to 390 s) for $\Delta V = 5$ mV ($\Delta V = 1$ mV) and $g \in [0.1, 12]$.

4.2.3 Linear Stability Analysis

To compute the Maximal Lyapunov Exponent (MLE) we make use of the linearization of (4.1), which describes the evolution of infinitesimal perturbations in the reference orbits, this reads as:

$$\begin{aligned}
\delta E_i(n+1) &= \mathrm{e}^{-\alpha\tau(n)}\left[\delta E_i(n) + \tau(n)\delta P_i(n)\right] \\
&\quad - \mathrm{e}^{-\alpha\tau(n)}\left[\alpha E_i(n) + (\alpha\tau(n)-1)P_i(n)\right]\delta\tau(n)\,, \qquad (4.8a)\\
\delta P_i(n+1) &= \mathrm{e}^{-\alpha\tau(n)}\left[\delta P_i(n) - \alpha P_i(n)\delta\tau(n)\right]\,, \qquad (4.8b)\\
\delta v_i(n+1) &= \mathrm{e}^{-\tau(n)}\left[\delta v_i(n) + (a_i - v_i(n))\delta\tau(n)\right] + g\delta H_i(n) \\
&\quad i = 1,\ldots,N \quad ; \quad \delta v_m(n+1) \equiv 0\,. \qquad (4.8c)
\end{aligned}$$

The expression of $\delta\tau(n)$ is calculated by differentiating (4.2) and (2.6).

The MLE λ_M is defined as the the average exponential growth rate of the infinitesimal perturbation

$$\delta = (\delta v_1 \ldots \delta v_N,\, \delta E_1 \ldots \delta E_N,\, \delta P_1 \ldots \delta P_N)$$

measured through the equation

$$\lambda_M = \lim_{t\to\infty} \frac{1}{t} \log \frac{\mid \delta(t) \mid}{\mid \delta_0 \mid} \quad , \qquad (4.9)$$

where δ_0 is the initial perturbation. The evolution of the perturbation $\delta(t)$ at the following times can be obtained by integrating Eqs. (4.8) in the tangent space in parallel with the evolution in the real space and by performing at regular time intervals the rescaling of its amplitude to avoid numerical artifacts, as detailed in [78]. A positive λ_M denotes a chaotic dynamics, $\lambda_M = 0$ is associated to a periodic (or quasiperiodic) orbit, and a negative one to a stable fixed point. It is important to stress that, since we are dealing with an event driven map formulation of the dynamics, the zero Lyapunov exponent which is always present for continuous time evolution and associated to the growth rate of a perturbation along the orbit, is automatically discarded. This implies that, if the evolution is stable, either a fixed point or a periodic solution, we measure in both cases a MLE smaller than zero.

4.2.4 State Transition Matrix (STM) and measure of dissimilarity

The STM is constructed by calculating the firing rates $\nu_i(t)$ of the N neurons at regular time intervals $\Delta T = 50$ ms. At each time t the rates are measured by counting the the number of spikes emitted in a window $2\Delta T$, starting at the considered time. Notice that the time resolution here used is higher with respect to that employed for the cross-correlation matrix, since we are interested in the response of the network to a stimulus presentation evaluated on a limited time window. The firing rates can be represented as a state vector $R(t) = \{\nu_i(t)\}$ with $i = 1,\ldots,N$. For an experiment of duration T_e, we have $S = \lfloor T_e/\Delta T \rfloor$ state vectors $R(t)$ representing the network evolution ($\lfloor\cdot\rfloor$ denotes the integer part). In order to measure the similarity of two states at different times $t_m = m \times \Delta T$ and $t_n = n \times \Delta T$, we have calculated the normalized scalar product

$$\chi(m,n) = \frac{R(t_m)\cdot R(t_n)}{|R(t_m)||R(t_n)|} \qquad (4.10)$$

for all possible pairs $m, n = 1, \ldots, S$ during the time experiment T_e. This gives rise to a $S \times S$ matrix called the state transition matrix [132].

In the case of the two input experiment reported in the results section, the obtained STM has a periodic structure of period T_{sw} with high correlated blocks followed by low correlated ones. A useful assoacited matrix is the coarse grained version of the entire STM obtained by taking a $4T_{sw} \times 4T_{sw}$ block from the STM, where the time origin corresponds to the onset of one of the two stimuli. The block is then averaged over r subsequent windows of duration $4T_w$, whose origin is shifted each time by $2T_{sw}$. More precisely the averaged STM $\langle \chi(m,n) \rangle$ is obtained as follows:

$$\langle \chi(m,n) \rangle = \frac{1}{r^2} \sum_{i,j=1}^{r} \chi(4i+m, 4j+n) \qquad \forall\, m,n \leq \lfloor T_{sw}/\Delta T \rfloor \quad . \tag{4.11a}$$

In a similar manner we can define a dissimilarity measure to distinguish between the response of the network to two different inputs. We define a control input $I^c = \{I_i^c\} \in [V_{th},\, V_{th} + \Delta V]$, and we register the network state vectors $R^c(t)$ at S regular time intervals for a time span T_e. We repeat the numerical experiment by considering the same network realization and the same initial conditions, but with a new input $I^{(f)} = \{I_i^{(f)}\}$. The external inputs $I_i^{(f)}$ coincide with the control ones, apart from a fraction f which is randomly taken from the interval $[V_{th},\, V_{th} + \Delta V]$. For the modified input we register another sequence $R^f(t)$ of state vectors on the same time interval, with the same resolution. The instantaneous dissimilarity $d^f(t)$ between the response to the control and perturbed stimuli is defined as:

$$d^f(t_m) = 1 - \frac{R^c(t_m) \cdot R^f(t_m)}{|R^c(t_m)||R^f(t_m)|} \tag{4.12}$$

its average in time is simply given by $\langle d \rangle^f = \frac{1}{S} \sum_{i=1}^{S} d^f(t_i)$.

4.2.5 Distinguishability measure Q_d

Following [123] a metric of the ability of the network to distinguish between two different inputs ΔM_d can be defined in terms of the STM. In particular, let us consider the STM obtained for two inputs $I^{(1)}$ to $I^{(2)}$, each presented for a time lag T_{sw}. In order to define ΔM_d the authors in [123] have considered the correlations of the state vector R taken at a generic time t_{m_0} with all the other configurations, with reference to Eq. (4.10) this amounts to examine the elements $\chi(m_0, n)$ of the STM $\forall t_n$. By defining M_1 (M_2) as the average of $\chi(m_0, n)$ over all the times t_n associated to the presentation of the stimulus $I^{(1)}$ ($I^{(2)}$), a distinguishablity metric between the two inputs can be finally defined as

$$\Delta M_d = |M_1 - M_2| \,. \tag{4.13}$$

In order to take in account the single neuron variability and the number of active neurons involved in the network dynamics we have modified ΔM_d by multiplying this quantity by the fraction of active neurons and the average coefficient of variation, as follows

$$Q_d = \Delta M_d \times n^* \times \overline{CV}_N \,. \tag{4.14}$$

In the equation above and in what follows, the symbol $\overline{CV}_N$, denotes the average over the ensemble of N elements, of the quantity under the bar.

4.2.6 Principal Components Analysis (PCA)

The Principal Component Analysis (PCA) can be performed by collecting S state vectors $R(t)$, measured at regular intervals ΔT for a time interval T_e, then by estimating the covariance matrix $cov(\nu_i, \nu_j)$ associated to this state vectors. The principal components are the eigenvectors of this matrix, ordered from the largest to the smallest eigenvalue. Each eigenvalue represents the variance of the original data along the corresponding eigendirection. A reconstruction of the original data set can be obtained by projecting the state vectors along a limited number of principal eigenvectors, obviously by employing the first eigenvectors will allow to have a more faithful reconstruction.

4.2.7 Synchronized Event Transition Matrix (SETM)

In order to obtain a Synchronized Event Transition Matrix (SETM), we first coarse grain the raster plot of the network. This is done by considering a series of windows of duration $T_W = 50$ ms covering the entire raster plot. A bursting event is identified whenever a neuron i fires 3 or more spikes within the considered window. To signal the burst occurrence a dot is drawn at the beginning of the window. From this coarse grained raster plot we obtain the Network Bursting Rate (NBR) by measuring the fraction of neurons that are bursting within the considered window. When this fraction is larger or equal to the average NBR plus two standard deviation, a synchronized event is identified. Each synchronized event is encoded in the the synchronous event vector $W_s(t)$, a N dimensional binary vector where the i-th entry is 1 if the i-th neuron participated in the synchronized event and zero otherwise. To measure the similarity between two synchronous events, we make use of the normalized scalar product between all the pairs of vectors W_s obtained at the different times t_i and t_j in which a synchronized event occurred. This represents the element i, j of the SETM.

4.2.8 Clustering algorithm

The *k-means* algorithm is a widespread mining technique in which N data points of dimension M are organized in clusters as follows. As a first step a number k of clusters is defined a-priori, then from a sub-set of the data k samples are chosen randomly. From each sub-set a centroid is defined in the M-dimensional space. at a second step, the remaining data are assigned to the closest centroid according to a distance measure. After the process is completed, a new set of k centroids can be defined by employing the data assigned to each cluster. The procedure is repeated until the position of the centroids converge to their asymptotic value.

An unbiased way to define a partition of the data can be obtained by finding the optimal cluster division [58]. The optimal number of clusters can be found by

maximizing the following cost function, termed *modularity*:

$$\mathcal{M} = \frac{1}{A_{tot}} \sum_{ij} (A_{ij} - \mathcal{N}_{ij})\, \delta(c_i, c_j), \tag{4.15}$$

where, $A \equiv \{A_{i,j}\}$ is the matrix to be clusterized, the normalization factor is $A_{tot} = \sum_{ij} A_{ij}$; $\mathcal{N}_{ij}$ accounts for the matrix element associated to the *null model*; c_i denotes the cluster to which the i-th element of the matrix belongs to, and $\delta(i, j)$ is the Kronecker delta. In other terms, the sum appearing in Eq. (4.15) is restricted to elements belonging to the same cluster. In our specific study, A is the *similarity matrix* corresponding to the SETM previously introduced. Furthermore, the elements of the matrix $\mathcal{N}$ are given by $\mathcal{N}_{ij} = \Gamma_i \Gamma_j / A_{tot}$, where $\Gamma_i = \sum_j A_{ij}$, these correspond to the expected value of the similarity for two randomly chosen elements [133, 134]. If two elements are similar than expected by chance, this implies that $A_{ij} > \mathcal{N}_{ij}$, and more similar they are larger is their contribution to the modularity $\mathcal{M}$. Hence they are likely to belong to the same cluster. The problem of modularity optimization is NP-hard [135], nevertheless some heuristic algorithms have been developed for finding local solutions based on greedy algorithms [136, 137, 138, 139]. In particular, we make use of the algorithm introduced for connectivity matrices in [140, 133], which can be straightforwardly extended to similarity matrices by considering the similarity between two elements, as the weight of the link between them [141]. The optimal partition technique is used in subsection *Response of the network to an increased level of excitability*, where it is applied to the similarity matrix $\mathcal{S}_{ij} = 1 - \mathcal{E}_{ij}$ where the distance matrix $\mathcal{E}_{ij} = \frac{\|x_i^p - x_j^p\|_2}{\max(\mathcal{E})}$. Here x_i^p is the vector defining the i^{th} synchronized event projected in the first p principal components, which accounts for the 80% of the variance.

4.3 Results

4.3.1 Measuring cell assembly dynamics

The model is composed of N leaky integrate-and-fire (LIF) inhibitory neurons [17, 18], with each neuron receiving inputs from a randomly selected 5% of the other neurons (i.e. a directed Erdös-Renyi graph with constant in-degree $K = pN$, where $p = 5\%$) [19]. The inhibitory post-synaptic potentials (PSPs) are schematized as α-functions characterized by a decay time τ_α and a peak amplitude A_{PSP}. In addition, each neuron i is subject to an excitatory input current mimicking the cortical and thalamic inputs received by the striatal network. In order to obtain firing periods of any duration the excitatory drives are tuned to drive the neurons in proximity of the supercritical bifurcation between the quiescent and the firing state, similarly to [121]. Furthermore, our model is integrated exactly between a spike emission and the successive one by rewriting the time evolution of the network as an event-driven map [74] (for more details see Methods).

Since we will compare most of our findings with the results reported in a previous series of papers by Ponzi and Wickens (PW) [121, 122, 123] it is important to stress the similarities and differences between the two models. The model employed by PW is a two dimensional conductance-based model with a potassium and a sodium channel [16], our model is simply a current based LIF model. The

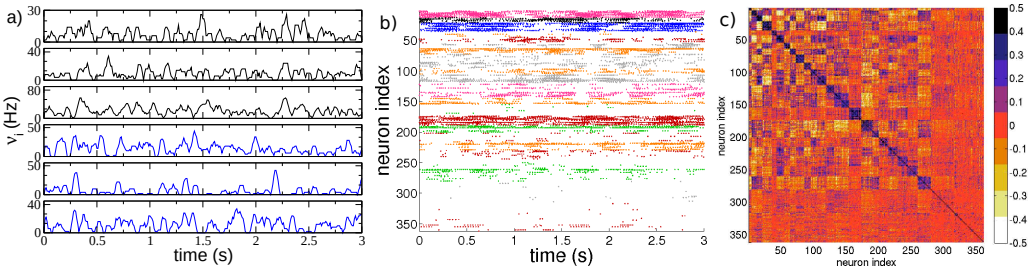

Figure 4.1: **Cell activity characterization.** a) Firing rates ν_i of 6 selected neurons belonging to two anti-correlated assemblies, the color identifies the assembly and the colors correspond to the one used in b) for the different clusters; b) raster plot activity, the firing times are colored according to the assembly the neurons belong to; c) cross-correlation matrix $C(\nu_i, \nu_j)$ of the firing rates. The neurons in panel b) and c) are clustered according to the correlation of their firing rates by employing the *k-means* algorithm; the clusters are ordered in terms of their average correlation (inside each cluster) from the highest to the lowest one (for more details see Methods). The firing rates are calculated over overlapping time windows of duration 1 s, the origins of successive windows are shifted by 50 ms. The system is evolved during 10^7 spikes, after discarding an initial transient of 10^5 spike events. Other parameters used in the simulation: $g = 8$, $K = 20$, $N = 400$, $k_{mean} = N_{act}/15$, $\Delta V = 5$ mV and $\tau_\alpha = 20$ ms. The number of active neurons is 370, corresponding to $n^* \simeq 93$ %.

parameters of the PW model are chosen so that the cell is in proximity of a saddle-node on invariant circle (SNIC) bifurcation to guarantee a smooth increase of the firing period when passing from the quiescent to the supra-threshold regime, without a sudden jump in the firing rate. Similarly, in our simulations the parameters of the LIF model are chosen in proximity of the bifurcation from silent regime to tonic firing. In the PW model the PSPs are assumed to be exponentially decaying, in our case we considered α-functions.

In particular, we are interested in selecting model parameters for which uniformly distributed inputs $I = \{I_i\}$, where $I_i \in [V_{th}, V_{th} + \Delta V]$, produce cell assembly-like sequential patterns in the network. The main aspects of the desired activity can be summarized as follows: (i) single neurons should exhibit large variability in firing rates ($CV > 1$); (ii) the dynamical evolution of neuronal assemblies should reveal strong correlation within an assembly and anti-correlation with neurons out of the assembly. As suggested by many authors [54, 130] the dynamics of MSNs cannot be explained in terms of a *winners take all* (WTA) mechanism, which would imply a small number of highly firing neurons, while the remaining would be silenced. Therefore we will search, in addition to the requirements (i) and (ii), for a regime where a substantial fraction of neurons are actively involved in the network dynamics. This represents a third criterion (iii) to be fulfilled to obtain a striatum-like dynamical evolution.

Fig. 4.1 shows an example of such dynamics for the LIF model, with three pertinent similarities to previously observed dynamics of real MSN networks [48]. Firstly, cells are organized into correlated groups, and these groups are mutually anticorrelated (as evident from the cross-correlation matrix of the firing rates re-

ported in Fig. 4.1 (c)). Secondly, individual cells within groups show irregular firing as shown in Fig. 4.1 (a). This aspect is reflected in a coefficient of variation (CV) of the inter-spike-intervals (ISIs) definitely greater than one (see the black curve in Fig. 4.5 (b)) as observed experimentally for the dynamics of rat striatum *in-vitro* [52, 54]. Thirdly, the raster plot reported in Fig. 4.1 (b) reveals that a large fraction of neurons (namely,$\simeq$ 93 %) is actively involved in the neural dynamics.

4.3.2 A novel measure for the structured cell assembly activity

The properties (i),(ii), and (iii), characterizing MSN activity, can be quantified in terms of a single scalar metric Q_0, as follows:

$$Q_0 \equiv \overline{CV}_N \times \sigma(C(\nu_i, \nu_j)) \times n^* \quad ; \tag{4.16}$$

We expect that good parameter values for our model can be selected by maximizing Q_0.

Our metric is inspired by a metric introduced to identify the level of cluster synchronization and organization for a detailed striatal microcircuit model [142]. However, that metric is based on the similarity among the point-process spike trains emitted by the various neurons, whereas Q_0 uses correlations between firing rate time-courses. Furthermore, Q_0 takes also in account the variability of the firing rates, by including the average CV in Eq. (4.16), an aspect of the MSN dynamics omitted by the metric employed in [142]. Within biologically meaningful ranges, we find values of the parameters controlling lateral inhibition (namely, the synaptic strength g and the the post-synaptic potential duration τ_α) that maximize Q_0. As we show below, the chosen parameters not only produce MSN-like network dynamics but also optimize the network′s computational capabilities, in the sense of producing a consistent, temporally-structured response, to a given pattern of inputs while discriminating between inputs which differ only for a few elements.

4.3.3 The role of lateral inhibition

In this sub-section we examine how network dynamics is affected by the strength of inhibitory connections. When these lateral connections are very weak (parameter g close to zero), the dominant input to each neuron is the constant excitation. As a result, most individual neurons are active (fraction of active neurons, n^*, is close to 1 as depicted in Fig 4.2 (a,e)) As lateral inhibition is made stronger, some neurons begin to slow down or even stop firing, and n^* declines towards a minimum fraction of $\simeq$ 50% (at $g = g_{min}$). As noted by Ponzi and Wickens [123], this is due to a winner-take-all (WTA) mechanism: faster-firing neurons depress or even silence the neurons to which they are connected. The activity for $g < g_{min}$ (blue triangled symbols in Fig 4.2) is characterized by a distribution of the average interspike intervals $F(\langle ISI \rangle)$ which is peaked at low firing periods (see blue triangled line in Fig 4.2(b) and (f)), and from the distribution of the CV exhibiting a single large peak at $CV \simeq 0$ (very regular firing) as shown in Figs. 4.2 and (c) and (g) with the same symbols.

As soon as $g > g_{min}$ (black circled symbols in Fig 4.2), the neuronal activity is no longer due only to the *winners*, but also the *losers* begin to play a role.

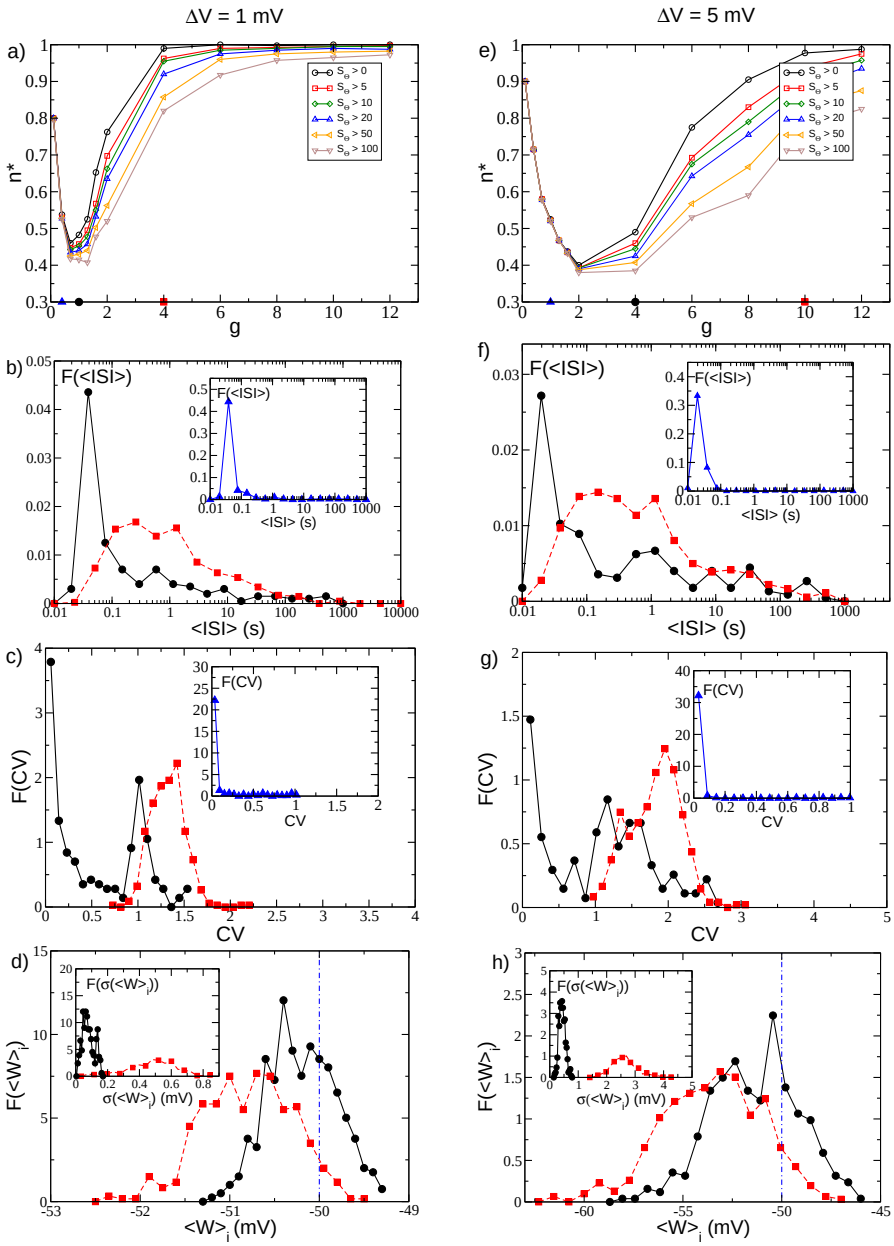

Figure 4.2: **Network statistics vs lateral inhibition**. a,e) Fraction of active neurons n^* vs the synaptic strength, for several thresholds S_θ. Three values of g are chosen for a detailed analysis indicated by the symbols along the x-axis. b,f) Neuronal distributions of the average $\langle ISI \rangle$ for the three values selected in the panel above (inset corresponds to the smallest g). c,g) Distributions of the CV for the same three cases. d,h) Distribution of the average synaptic input $\langle W \rangle_i$ for the two largest values of g; vertical line indicates the threshold; inset: Distribution of the average fluctuation in time for the same two values. Panels a-d) correspond to $\Delta V = 1$ mV and the chosen values of synaptic strength are $g = \{0.4, 1, 4\}$; e-h) correspond to $\Delta V = 5$ mV and $g = \{1, 4, 10\}$. For calculating the statistics, the system is evolved during 10^7 spikes, after discarding 10^5 spike events. Other parameters used in the simulation: $K = 20$, $N = 400$ and $\tau_\alpha = 20$ ms.

The *winners* are characterized by an effective input W_i which is on average supra-threshold, and their firing activity is driven by the mean current: *winners* are *mean-driven* [21]. On the other hand, *losers* are on average below-threshold, and their firing is due to current fluctuations: *losers* are *fluctuation-driven* [21], (see Figs. 4.2 (d) and (g)). This is reflected in the corresponding distribution $F(\langle ISI \rangle)$ (Fig. 4.2(b) and (f)). The *winners* have very short $\langle ISI \rangle$s (i.e. high firing rates), while the *losers* are responsible for the long tail of the distribution extending up to $\langle ISI \rangle \simeq 10^3$ s. In the distribution of the coefficients of variation (Fig. 4.2(c) and (g)) the *winners* generate a peak of very low CV (i.e. highly-regular firing), suggesting that they are not strongly influenced by the other neurons in the network and therefore have an effective input on average supra-threshold. By contrast the *losers* are associated with a smaller peak at $CV \simeq 1$, confirming that their firing is due to large fluctuations in the currents.

Counterintuitively however, further increases in lateral inhibition strength result in increased neuronal participation, with n^* progressively returning towards $\simeq 1$. The same effect was previously reported by Ponzi and Wickens [123] for a different, more complex, model. When the number of active neurons returns almost to 100%, i.e. for sufficiently large coupling $g >> g_{min}$ (red circled symbols in Fig 4.2), most of the neurons appear to be below threshold, as revealed by the distribution of the effective inputs W_i reported in Figs. 4.2(d) and (g). Therefore in this case the network firing is essentially fluctuation-driven, as a matter of fact the $F(\langle ISI \rangle)$ distribution is now characterized by a broader distribution and by the absence of the peak at short $\langle ISI \rangle$ (as shown in Fig. 4.2(b) and (f)). Furthermore the single neuron dynamics is definitely bursting, as shown by the fact that the CV distribution is now centered around $CV \simeq 2$ (Figs. 4.2(c) and (g)).

The transition between the two dynamical regimes, occurring at $g = g_{min}$, is due to a passage from a state where some *winner* neurons were mean-driven and were able to depress all the other neurons, to a state at $g >> g_{min}$ where almost all neurons are fluctuation-driven and contribute to the network activity. The transition occurs because at $g < g_{min}$ the fluctuations in the effective input currents W_i are small and insufficient to drive the *losers* towards the firing threshold (as shown in the insets of Fig. 4.2(d) and (g)). At $g \simeq g_{min}$ the amplitude of the fluctuations becomes sufficient for some *losers* to cross the firing threshold and contribute to the number of active neurons. This will also reduce the *winners'* activity. For $g >> g_{min}$ the fluctuations of W_i are sufficient to lead almost all *losers* to fire and no clear distinction between *losers* and *winners* remains. The transition is due to the fact that not only the average inhibitory action is proportional to the synaptic strength, but also the amplitude of the current fluctuations increases linearly with g, at least for $g > g_{min}$ (see Fig 4.3).

The reported results explain why the variability $\sigma(C)$ of the cross-correlation matrix has a non monotonic behaviour with g (as shown in the middle panel in Fig. 4.4(a)). At low coupling $\sigma(C)$ is almost zero, since the single neuron dynamics are essentially independent one from another, while the increase of the coupling leads to an abrupt rise of $\sigma(C)$. This growth is clearly associated with the inhibitory action which splits the neurons into correlated and anti-correlated groups. The variability of the cross-correlation matrix achieves a maximum value for coupling slightly larger than g_{min}, where fluctuations in the effective currents

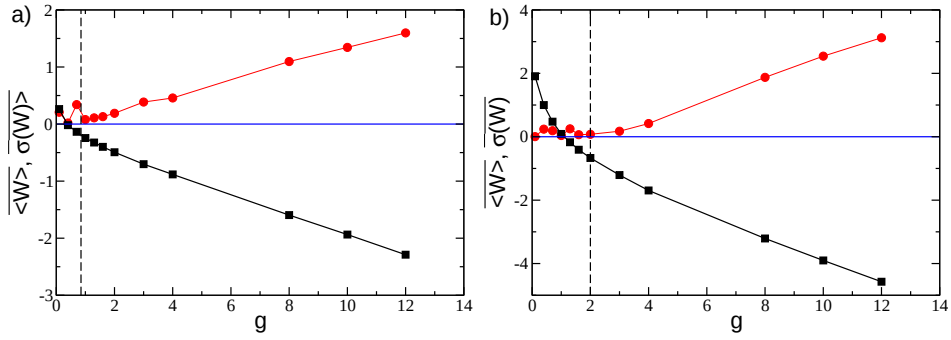

Figure 4.3: **Effective input currents and fluctuations.** Effective input currents $\overline{\langle W \rangle}$ (black filled squares) and the corresponding standard deviation $\overline{\sigma(W)}$ (red filled circles) averaged over all the neurons in the network for $\Delta V = 1$ mV (a) and $\Delta V = 5$ mV (b). The effective currents are shifted by V_{th}: negative (positive) values correspond to neurons on average below (above) threshold. The dashed vertical lines indicated the position of g_{min}. The system is evolved during 10^7 spikes, after discarding 10^5 spike events. Other parameters used in the simulation: $K = 20$, $N = 400$ and $\tau_\alpha = 20$ms.

begin to play a relevant role in the network dynamics. At larger coupling $\sigma(C)$ begins to decay towards a finite non zero value. These results confirm that the most interesting region to examine is the one with coupling $g > g_{min}$, as already suggested in [123].

The observed behaviour of $\overline{CV}$, n^* and $\sigma(C)$ suggests that we should expect a maximum in Q_0 at some intermediate coupling $g > g_{min}$, as indeed we have found for both studied cases, as shown in Fig. 4.4 (b) and (c). The initial increase in Q_0 is due to the increase in CV and n^*, while the final decrease, following the occurrence of the maximum, is essentially driven by the decrease of $\sigma(C)$. For larger ΔV the neurons tend to fire regularly in a wider range of coupling at small g (see Fig. 4.4 (c)), indicating that due to their higher firing rates a larger synaptic inhibition is required to influence their dynamics. On the other hand, their bursting activity observable at large g is more irregular (see the upper panel in Fig. 4.4 (a); dashed line and empty symbols).

To assess whether parameters that maximize Q_0 also allow discrimination between different inputs, we alternated the network back and forth between two distinct input patterns, each presented for a period T_{sw}. During this stimulation protocol, we evaluated the state transition matrix (STM) and the associated quantity ΔM_d. The STM measures the similarity among the firing rates of the neurons in the network taken at two different times. The metric ΔM_d, based on the STM, has been introduced in [123] to quantify the ability of the network to distinguish between two inputs. To verify whether the ability of the network to distinguish different stimuli is directly related to the presence of dynamically correlated and anti-correlated cell assemblies, we generated the new metric, Q_d. This metric is defined in the same way as Q_0, except that in in Eq. (4.16) the standard deviation of the correlation matrix is replaced by ΔM_d. As it can be appreciated from Figs. 4.4(b) and 4.4(c) the metrics Q_d and Q_0 behave similarly, indicating that indeed Q_0 becomes maximal in the parameter range in which the network is most

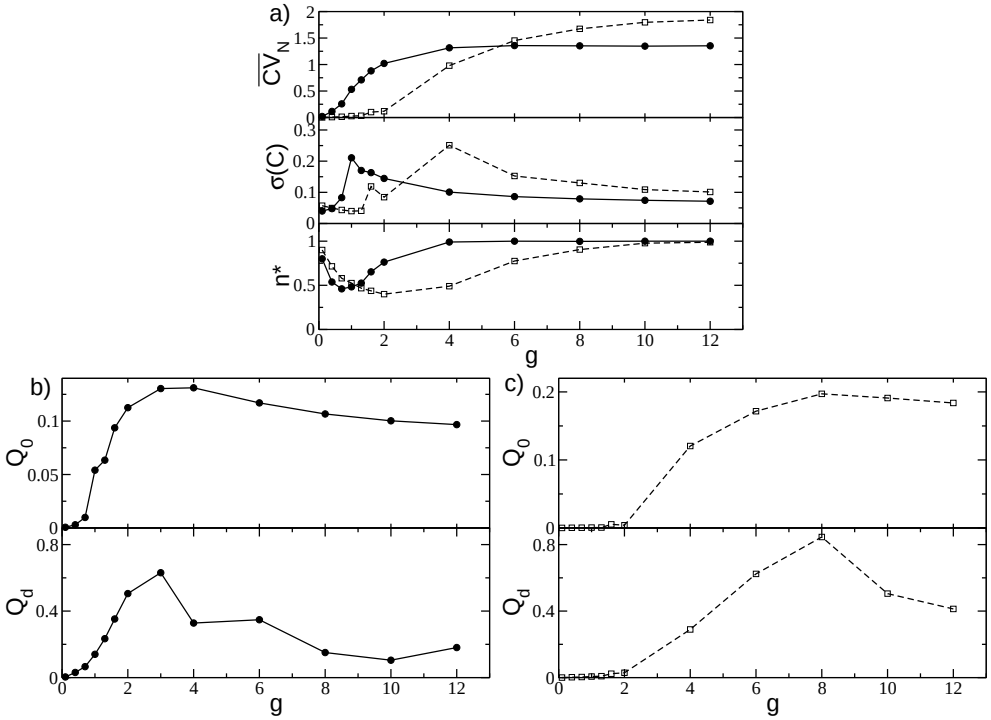

Figure 4.4: **Metrics of structured activity vs lateral inhibition strength.** a) Metrics entering in the definition of Q_0 versus the synaptic strength g. From top to bottom: Averaged coefficient of variation $\overline{CV}_N$, standard deviation of the cross-correlation matrix $\sigma(C)$, and the fraction of active neurons n^* with a threshold $S_\Theta = 2$. The solid (dashed) line refers to the case $\Delta V = 1$ mV ($\Delta V = 5$ mV). The minimum number of active neurons is achieved at $g = g_{min}$, this corresponds to a peak amplitude of the PSP $A_{PSP} = 0.064$ mV ($A_{PSP} = 0.184$ mV) for $\Delta V = 1$ mV ($\Delta V = 5$ mV). b) Q_0 and Q_d, as defined in Eqs. (4.16) and (4.14), versus g for $\Delta V = 1$ mV. c) Same as b) for $\Delta V = 5$ mV. Other parameters as in Fig. 4.1

effectively distinguishing different stimuli. We speculate that the emergence of correlated and anti-correlated assemblies contributes to this discriminative ability.

We note that we observed maximal values of Q_0 for realistic lateral inhibition strengths, as measured from the post-synaptic amplitudes A_{PSP}. Specifically, Q_0 reaches the maximum at $g = 4$ ($g = 8$) for $\Delta V = 1$ mV ($\Delta V = 5$ mV) corresponding to $A_{PSP} = 0.368$ mV ($A_{PSP} = 0.736$ mV), comparable to previously reported experimental results [52, 130, 54]

4.3.4 The role of the post-synaptic time scale

In brain slice experiments IPSCs/IPSPs between MSNs last 5-20 ms and are mainly mediated by the $GABA_a$-receptor [52, 131]. In this sub-section, we will examine the effect of the the post-synaptic time constant τ_α. As τ_α is increased from 2 to 50 ms, the values of of both metrics Q_0 and Q_d progressively increase (Fig. 4.5(a)), with the largest variation having already occurred by $\tau_\alpha = 20$ ms. To gain more insights on the role of the PSP in shaping the structured dynamical regime, we show for the same network the distribution of the single cell CV, for $\tau_\alpha = \{2, 9, 20\}$

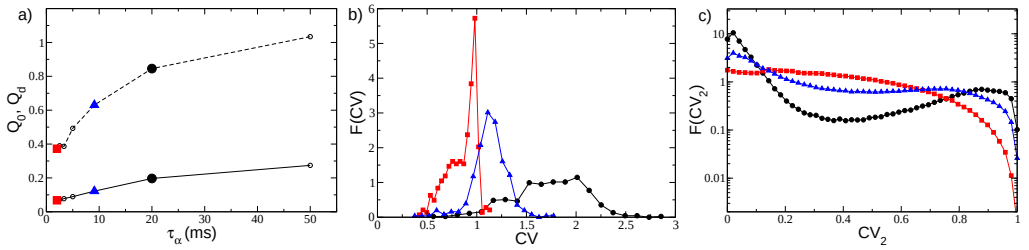

Figure 4.5: **Metrics of structured activity vs post-synaptic time duration.** a) Metrics Q_0 (in solid line) and Q_d (dashed) as a function of the pulse time scale for the parameter values $\{\Delta V, g\} = \{5 \text{ mV}, 8\}$ corresponding to the maximum Q_0 value in Fig. 4.4(d). Probability distribution functions $F(CV)$ ($F(CV_2)$) for the coefficient of variation CV (local coefficient of variation CV_2) are shown in b) (in c)) for three representative $\tau_\alpha = \{2, 9, 20\}$ ms, displayed by employing the same symbols and colors as indicated in a). For these three cases the average firing rate in the network is $\langle \nu \rangle = \{8.81, 7.65, 7.35\}$ Hz ordered for increasing τ_α-values. Other parameters as in Fig. 4.1

ms (Fig. 4.5(b)). Narrow pulses ($\tau_\alpha \simeq 2$ ms) are associated with a distribution of CV values ranging from 0.5 to 1, with a predominant peak at one. By increasing τ_α one observes that the CV distributions shift to larger and larger CV values. Therefore, one can conclude that at small τ_α the activity is mainly Poissonian, while increasing the duration of the PSPs leads to bursting behaviours, as in experimental measurements of the MSN activity [46]. In particular in [46], the authors showed that bursting activity of MSNs with a distribution $F(CV)$ centered around $CV \simeq 2$ is typical of awake wild-type mice. To confirm this analysis we have estimated also the distribution of the CV_2: A CV_2 distribution with a peak around zero denotes a very regular firing, while a peak around one indicates the presence of long silent periods followed by rapid firing events (i.e. a bursting activity). Finally a flat distribution denotes Poissonian distributed spiking. It is clear from Fig. 4.5(c) that by increasing τ_α from 2 to 20 ms this leads the system from an almost Poissonian behaviour to bursting dynamics, where almost regular firing inside the burst (intra-burst) is followed by a long quiescent period (inter-burst) before starting again.

The distinct natures of the distributions of CV for short and long-tailed pulses raises the question of what mechanism underlies such differences. To answer this question we analyzed the distribution of the ISI of a single cell in the network for two cases: in a cell assembly bursting regime (corresponding to $\tau_\alpha = 20$ ms) and for Poissonian unstructured behavior (corresponding to $\tau_\alpha = 2$ ms). We expect that even the single neurons should have completely different dynamics in these two regimes, since the distributions $F(CV)$ at $\tau_\alpha = 2$ ms and 20 ms are essentially not overlapping, as shown in Fig. 4.5(b). In order to focus the analysis on the effects due to the synaptic inhibition, we have chosen, in both cases, neurons receiving exactly the same external excitatory drive I_s. Therefore, in absence of any synapses, these two neurons will fire with the same period $\text{ISI}_0 = \tau_m \log[(I_s - V_r)/(I_s - V_{th})] = 12$ ms, corresponding to a firing rate of 8.33 Hz not far from the average firing rate of the networks (namely, $\overline{\nu}_N \simeq 7 - 8$ Hz). Thus

these neurons can be considered as displaying a typical activity in both regimes. As expected, the dynamics of the two neurons is quite different, as evident from the $F(ISI)$ presented in Fig. 4.6(a) and (b). In both cases one observes a long tailed exponential decay of $F(ISI)$ corresponding to a Poissonian like behaviour. However the decay rate ν_D is slower for $\tau_\alpha = 20$ ms with respect to $\tau_\alpha = 2$ ms, namely $\nu_D \simeq 2.74$ Hz versus $\nu_D \simeq 20.67$ Hz. Interestingly, the main macroscopic differences between the two distributions arises at short time intervals. For $\tau_\alpha = 2$ ms, (see Fig. 4.6(b)) an isolated and extremely narrow peak appears at ISI_0. This first peak corresponds to the supra-threshold tonic-firing of the isolated neuron, as reported above. After this first peak, a gap is clearly visible in the $F(ISI)$ followed by an exponential tail. The origin of the gap resides in the fact that $\mathrm{ISI}_0 >> \tau_\alpha$, because if the neuron is firing tonically with its period ISI_0 and receives a single PSP, the membrane potential has time to decay almost to the reset value V_r before the next spike emission. Thus a single PSP will delay the next firing event by a fixed amount corresponding to the gap in Fig. 4.6(b). Indeed one can estimate analytically this delay due to the arrival of a single α-pulse, in the present case this gives $\mathrm{ISI}_1 = 15.45$ ms, in very good agreement with the results in Fig. 4.6(b). No further gaps are discernible in the distribution, because it is highly improbable that the neuron will receive two (or more) PSPs exactly at the same moment at reset, as required to observe further gaps. The reception of more PSPs during the ramp up phase will give rise to the exponential tail in the $F(ISI)$. In this case the contribution to the CV comes essentially from this exponential tail, while the isolated peak at ISI_0 has a negligible contribution.

On the other hand, if $\tau_\alpha > \mathrm{ISI}_0$, as in the case reported in Fig. 4.6(a), $F(ISI)$ does not show anymore a gap, but instead a continuous distribution of values. This because now the inhibitory effects of the received PSPs sum up leading to a continuous range of delayed firing times of the neuron. The presence of this peak of finite width at short ISI in the $F(ISI)$ plus the exponentially decaying tail are at the origin of the observed $CV > 1$. In Fig. 4.6 (e) and 4.6 (f) the distributions of the coefficient $CV_2^{(i)}$ are also displayed for the considered neurons as black lines with symbols. These distributions clearly confirm that the dynamics are bursting for the longer synaptic time scale and essentially Poissonian for the shorter one.

We would like to understand whether it is possible to reproduce similar distributions of the ISIs by considering an isolated cell receiving Poissonian distributed inhibitory inputs. In order to verify this, we simulate a single cell receiving K uncorrelated spike trains at a rate $\overline{\nu}_N$, or equivalently, a single Poissonian spike train with rate $K\overline{\nu}_N$. Here, $\overline{\nu}_N$ is the average firing rate of a single neuron in the original network. The corresponding $F(ISI)$ are plotted in Fig. 4.6 (c) and 4.6 (d), for $\tau_\alpha = 20$ ms and 2 ms, respectively. There is a remarkable similarity between the reconstructed ISI distributions and the real ones (shown in Fig. 4.6(a) and (b)) , in particular at short ISIs. Also the distributions of the $CV_2^{(i)}$ for the reconstructed dynamics are similar to the original ones, as shown in Fig. 4.6 (e) and 4.6 (f). Altogether, these results demonstrate that the bursting activity of inhibitory coupled cells is not a consequence of complex correlations among the incoming spike trains, but rather a characteristic related to intrinsic properties of the single neuron: namely, its tonic firing period, the synaptic strength, and the post-synaptic time decay. The fundamental role played by long synaptic time in

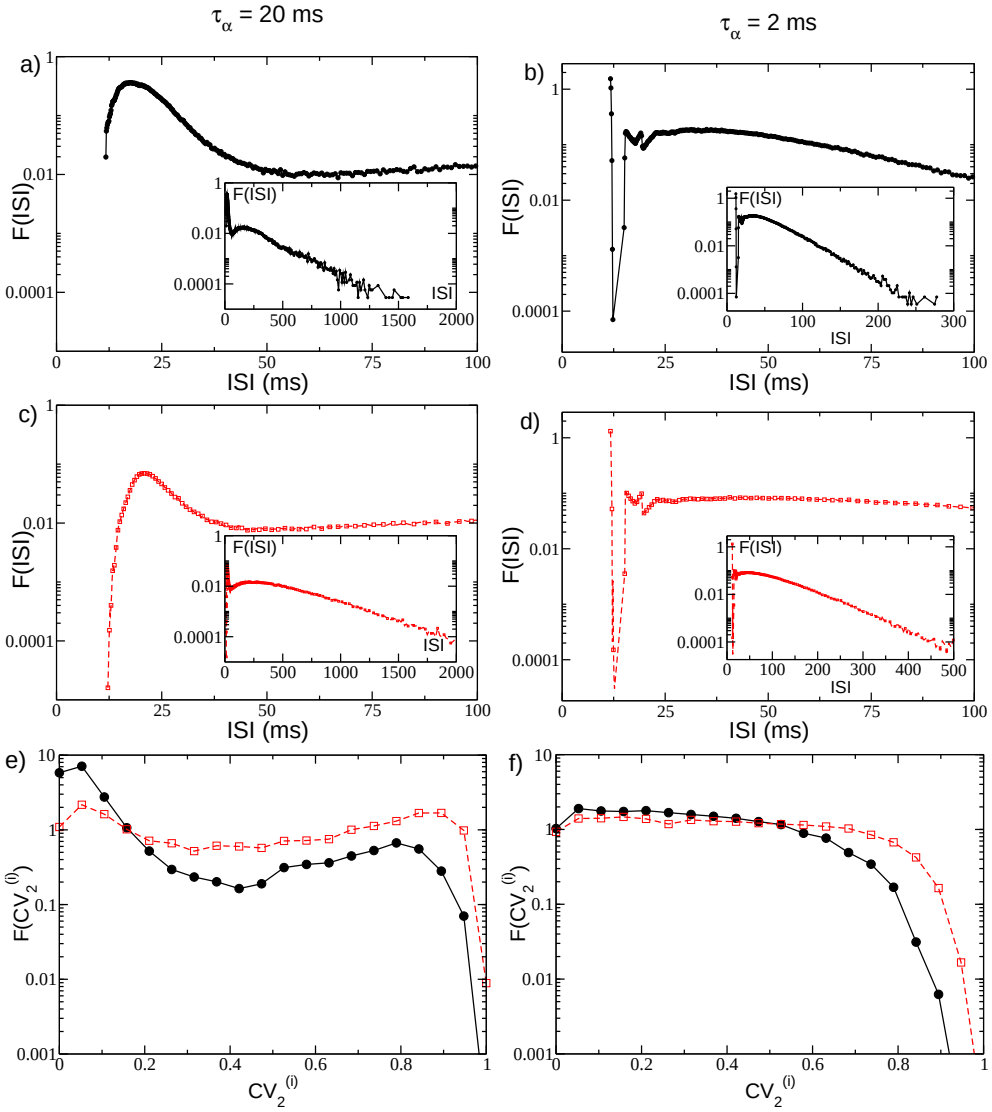

Figure 4.6: **Single neuron statistics.** First row : distributions $F(ISI)$ for one representative cell in the network are shown in black. Second row: the corresponding Poissonian reconstruction of the $F(ISI)$ are reported in red. In all plots the main figure displays the distributions at short ISIs, while the inset is a zoom out of the whole distribution. Third row: single neuron distribution of the $CV_2^{(i)}$ for the considered neuron (black solid lines with circles) and its Poissonian distribution (red dashed line with squares). The left (right) column corresponds to $\tau_\alpha = 20$ (2 ms). The network parameters are $\Delta V = 5$ mV and $g = 8$, and the others as in Fig. 4.1, both the examined neurons have $I_s = -45.64$ mV. For the Poissonian reconstruction the frequencies of the incoming uncorrelated spike trains are set to $\overline{\nu}_N \approx 7.4$ Hz ($\overline{\nu}_N \approx 8.3$ Hz) for $\tau_\alpha = 20$ms ($\tau_\alpha = 2$ms), as measured from the corresponding network dynamics. The distributions are obtained by considering a sequence of 10^9 spikes in the original network, and 10^7 events for the Poissonian reconstruction.

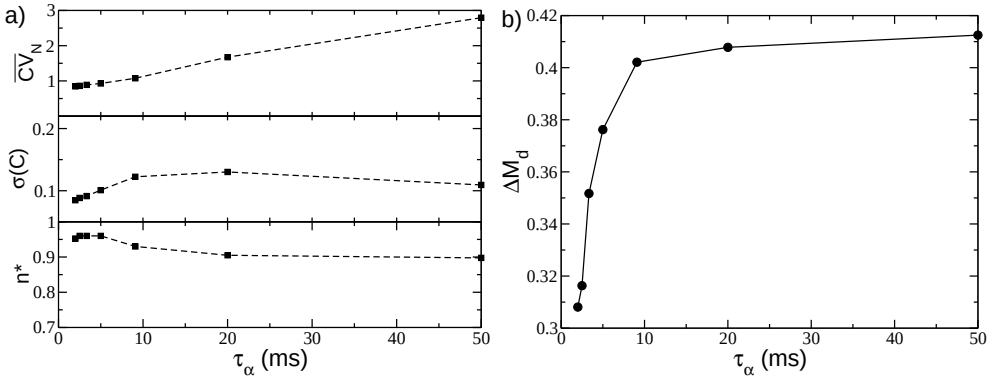

Figure 4.7: **Metrics of the structured activity vs synaptic time decay.** a) Metrics entering in the definition of Q_0 and their dependence from τ_α. From top to bottom: Averaged coefficient of variation $\overline{CV}_N$, standard deviation of the cross-correlation matrix $\sigma(C)$, and the fraction of active neurons n^*. b) ΔM_d as a function of τ_α. The system is left to evolve during 10^7 spikes, after discarding 10^5 transient spike events. Parameters here used $\Delta V = 5$ mV, $g = 8$, $K = 20$, $N = 400$.

inducing bursting activity has been reported also in a study of a single LIF neuron below threshold subject to Poissonian trains of exponentially decaying PSPs [143].

Obviously this analysis cannot explain collective effects, like the non trivial dependence of the number of active cells n^* on the synaptic strength, discussed in the previous sub-section, or the emergence of correlations and anti-correlations among neural assemblies (measured by $\sigma(C)$) due to the covarying of the firing rates in the network, as seen in the striatum slices and shown in Fig. 4.1 (c) for our model. To better investigate the influence of τ_α on the collective properties of the network we report in Fig. 4.7(a) and (b) the averaged CV, $\sigma(C)$, n^* and ΔM_d for $\tau_\alpha \in [2, 50]$ ms. As already noticed, the network performs better in mimicking the MSN dynamics and in discriminating between different inputs at larger τ_α (e.g. at 20 ms). However, what is the minimal value of τ_α for which the network still reveals cell assembly dynamics and discriminative capabilities ? From the data shown in Fig. 4.7(a) one can observe that $\sigma(C)$ and ΔM_d attain their maximal values in the range 10 ms $\leq \tau_\alpha \leq$ 20 ms. This indicates that clear cell assembly dynamics with associated good discriminative skills can be observed in this range. However, the bursting activity is not particularly pronounced at $\tau_\alpha = 10$ ms, where $\langle CV \rangle_N \simeq 1$. Therefore only the choice $\tau_\alpha = 20$ ms fulfills all the requirements.

Interestingly, genetic mouse models of Huntington's disease (HD) revealed that spontaneuous IPSCs in MSNs has a reduced decay time and half-amplitude duration compared to wild-types [125]. Our analysis clearly indicate that a reduction of τ_α results in more stochastic single-neuron dynamics, as indicated by $\overline{CV}_N \simeq 1$, as well as in a less pronounced structured assembly dynamics as shown in 4.7 (a). This resembles what observed for the striatum dynamics of freely behaving mice with symptomatic HD [46]. In particular, the authors have shown in [46] that at the single unit level HD mice reveals a $CV \simeq 1$ in contrast to $CV \simeq 2$ for wild-type mice, furthermore the correlated firing was definitely reduced in HD mice.

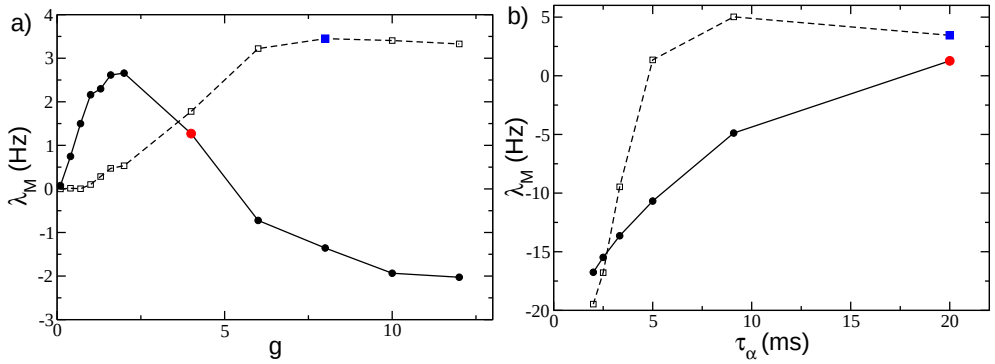

Figure 4.8: Linear stability analysis: a) Maximal Lyapunov exponent λ_M at a fixed $\tau_\alpha = 20$, as a function of connectivity strength for $\Delta V = 1$ mV (continuous line, filled circles) and $\Delta V = 5$ mV (dashed line, empty squares). b) Maximal Lyapunov exponent λ_M as a function of the pulse duration τ_α for the parameters $\{\Delta V, g\} = \{1 \text{ mV}, 4\}$ (continuous line with filled circles) and $\{5 \text{ mV}, 8\}$ (dashed line with empty squares). In both panels, the blue filled square indicates the triad $\{\Delta V, g, \tau_\alpha\} = \{5 \text{ mV}, 8, 20 \text{ ms}\}$, and the red filled circle to $\{\Delta V, g, \tau_\alpha\} = \{1 \text{ mV}, 4, 20 \text{ ms}\}$; these values are associated to the maximum values of Q_0 obtained for excitability distributions with fixed width ΔV. The tangent space Eq. (4.8) is evolved during a period corresponding to 10^7 spikes, after discarding a transient of 10^5 spikes. Other parameters used in the simulation: $K = 20$, $N = 400$.

4.3.5 Linear stability analysis

One of the questions that we would like to address is whether the existence of a bursting correlated activity is related to linear stability properties of the network or not. To characterize these properties, we calculate the MLE for the parameters examined in the text.

For a fixed pulse duration $\tau_\alpha = 20$ ms, the behaviour of λ_M as a function of the coupling g, for different excitability spreading ΔV, is definitely different. As shown in Fig. 4.8 (a), for $\Delta V = 1$ mV the MLE (as expected) is zero for very weakly coupled systems, then it first increases with g and reaches a maximum around $g = 2$ and then it decreases monotonically becoming negative for $g > 5$. For $\Delta V = 5$ mV, the MLE is always positive and increases with g saturating at an almost constant value $\lambda_M \simeq 3.4$ Hz for $g \geq 6$. We are specifically interested in the conditions for which the measure Q_0 is maximized, these points are indicated in Fig. 4.8 (a), as one can notice they correspond for both considered ΔV to positive λ_M.

Additionally we have analyzed the behaviour of λ_M as a function of τ_α by fixing g to the value that maximizes Q_0 in the previous analysis. In this case it appears that λ_M increases with τ_α and becomes definitely negative for sufficiently small τ_α (as shown in Fig. 4.8 (b)), in agreement with the results reported in [98, 87]. The cell assembly dynamics of our network resembles that of MSNs for large τ_α, the point where Q_0 is maximal are indicated also in Fig. 4.8 (b). These evidences seem to suggest that the striatally relevant dynamics correspond to a

chaotic regime, but located in proximity of the transition between chaotic and non-chaotic evolution [122].

However, all this analysis and the one reported in [122] consider only infinitesimal perturbations, while it has been clearly demonstrated that for inhibitory networks finite perturbations play a fundamental role as shown in [84, 98, 86, 87]. In particular our model, even for $\lambda_M < 0$, can display erratic evolution almost indistinguishable from chaos due to the so-called Stable Chaos mechanism [59, 87]. This leads us to conclude that the usual Lyapunov exponent is unable to capture the degree of erratic motion present in these systems, due to the possible amplification of finite amplitude perturbations.

4.3.6 Structural origin of the cell assemblies

A question that we have not addressed so far is: how do cell assemblies arise ? Since the network is purely inhibitory it is reasonable to guess that correlation (anti-correlation) among groups of neurons will be related to the absence (presence) of synaptic connections between the considered groups. In order to analyze the link between the correlation and the network connectivity we compare the clustered cross-correlation matrix of the firing rates $C(\nu_i, \nu_j)$ (shown in Fig 4.9 (a)) with the associated connectivity matrix $\mathcal{C}_{ij}$ (reported in Fig- 4.9 (b)). The cross-correlation matrix is organized in $k = 15$ clusters via the *k-means* algorithm, therefore we obtain a matrix organized in a $k \times k$ block structure, where each block (m, l) contains all the cross-correlation values of the elements in cluster m with the elements in cluster l. The connectivity matrix is arranged in exactly the same way, however it should be noticed that while $C(\nu_i, \nu_j)$ is symmetric, the matrix $\mathcal{C}_{ij}$ is not symmetric due to the unidirectional nature of the synaptic connections. From a visual comparison of the two figures it is clear that the most correlated blocks are along the diagonal and that the number of connections present in these diagonal blocks is definitely low, with respect to the expected value from the whole matrix. An exception is represented by the largest diagonal block which reveals, however, an almost zero level of correlation among its members. We have highlighted in blue some blocks with high level of anti-correlations among the elements, the same blocks in the connectivity matrix reveal a high number of links. A similar analysis, leading to the same conclusions was previously reported in [121].

However, we would like to make more quantitative this comparison. Therefore we have estimated for each block the average cross-correlation, denoted as $\overline{C}_{ml}$, and the average probability p_{ml} of unidirectional connections from the cluster l to the cluster m. These quantities are shown in Fig. 4.9 (c) for all the possible blocks, it is evident that the correlation $\overline{C}_{ml}$ decreases with the probability p_{ml}, a linear fit to the data is reported in the figure as a solid black line. However, there are blocks that are outliers with respect to this fit, in particular the black squares refer to the diagonal blocks and these are all associated to high correlation values $\overline{C}_{mm}$ and low probabilities p_{mm}, definitely smaller than the average probability $p = 0.05$, shown as a dashed vertical red line in Fig. 4.9 (c). An exception is represented by a single black square located exactly on the linear fit in proximity of $p = 0.05$, this is the large block with almost zero level of correlation among its elements previously identified. Furthermore, the blocks with higher anticorrelation, denoted as blue triangles in the figure, have probabilities p_{ml} definitely

larger than 5 %. Also in this case there are 2 exceptions, 2 triangles lie exactly on the vertical dashed line corresponding to 5 %. This is due to the fact that the p_{ml} are not symmetric, and it is sufficient to have a large probability to have connections in only one of the two possible directions between blocks m and l to observe anti-correlated activities between the two assemblies. To summarize we have clearly shown that the origin of the assemblies dynamically identified from the correlations of the firing rates is directly related to structural properties of the networks, as visualized by the connectivity matrix.

4.3.7 Discriminative and computation capability

In this sub-section we examine the ability of the network to perform different tasks: namely, to respond in a reproducible manner to equal stimuli and to discriminate between similar inputs via distinct dynamical evolution. For this analysis we have always compared the responses of the network obtained for a set of parameters corresponding to the maximum Q_0 value shown in Fig. 4.4(d), where $\tau_\alpha = 20$ ms, and for the same parameters but with a shorter PSP decay time, namely $\tau_\alpha = 2$ ms.

To check for the capability of the network to respond to cortical inputs with a reproducible sequences of states of the network, we perform a simple experiment where two different inputs $I^{(1)}$ and $I^{(2)}$ are presented sequentially to the system. Each input persists for a time duration T_{sw} and then the stimulus is switched to the other one and this process is repeated for the whole simulation time. The raster plot measured during such an experiment is shown in Fig. 4.10 (a) for $\tau_\alpha = 20$ ms. Whenever one of the stimuli is presented, a specific sequence of pattern activations can be observed. Furthermore, the sequence of emerging activity patterns is reproducible when the same stimulus is again presented to the system, as can be appreciated by observing the patterns encircled with black lines in Fig. 4.10 (a). Recall that the clustering algorithm here employed to identify the different groups is applied only during the presentation of the first stimulus, therefore the sequential dynamics is most evident for that particular stimuli.

Furthermore, we can quantitatively calculate how similar is the firing activity in the network at different times by estimating the STM. The similarity is quantified by computing the normalized scalar product of the instantaneous firing rates of the N neurons measured at time t_i and t_j. We observe that the similarity of the activity at a given time t_0 and at a successive time $t_0 + 2mT_{sw}$ is high (with values between 0.5 and 0.75), thus suggesting that the response to the same stimulus is similar, while it is essentially uncorrelated with the response at times corresponding to the presentation of a different stimulus, i.e. at $t_0 + (2m-1)T_{sw}$ (since the similarity is always smaller than 0.4) (here, $m = 1, 2, 3...$). This results in a STM with a periodic structure of period T_{sw} with alternating high correlated blocks followed by low correlated blocks (see Fig. 4.10(b)). The averaged version of the STM calculated over a sequence of 5 presentations of $I^{(1)}$ and $I^{(2)}$ is shown in Fig. 4.10 (c). These results show not only the capability of the network to distinguish between the stimuli, but also the reproducible nature of the system response. In particular, from Fig. 4.10 (c) it is evident how the patterns associated with the response to the stimulus $I^{(1)}$ or $I^{(2)}$ are clearly different and easily identifiable.

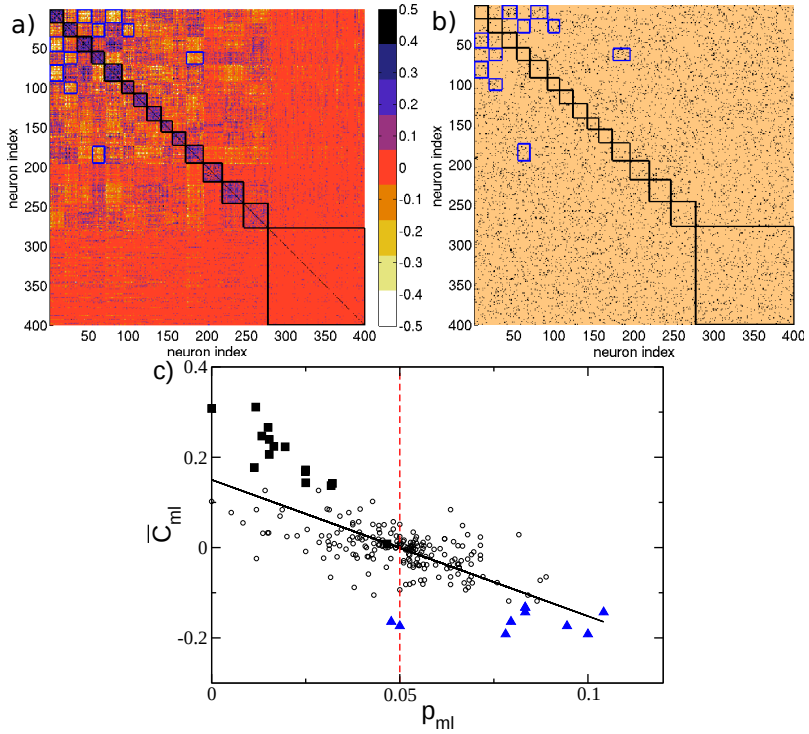

Figure 4.9: **Cell assemblies and connectivity.** a) Cross-correlation matrix $C(\nu_i, \nu_j)$ of the firing rates organized according to the clusters generated via the *k-means* algorithm with $k = 15$, the clusters are ordered as in Fig. 4.1(c) from the highest to the lowest correlated one. b) Connectivity matrix $\mathcal{C}_{ij}$ with the indices ordered as in panel a). Here, a black (copper) dot denotes a 1 (0) in $\mathcal{C}_{ij}$, i.e. the presence of a synaptic connection from j to i. c) Average cross-correlation $\overline{C}_{ml}$ among the elements of the matrix block (m, l) , versus the probability p_{ml} to have synaptic connections from neurons in the cluster l to neurons in the cluster m. Black squares indicate the blocks along the diagonal delimited by black borders in panel a) and b) , i.e. they correspond to the pairs $\{\overline{C}_{mm}, p_{mm}\}$; blue triangles denote the ten blocks with the lowest $\overline{C}_{ml}$ values, which are also delimited by blue edges in a) and b). The vertical red dashed line indicates the average probability to have a connection $p = 5\%$. The black solid line is the linear regression to the data ($\overline{C}_{ml} \approx 0.15 - 3.02 p_{ml}$, correlation coefficient $R = -0.72$). Other parameters as in Fig. 4.1.

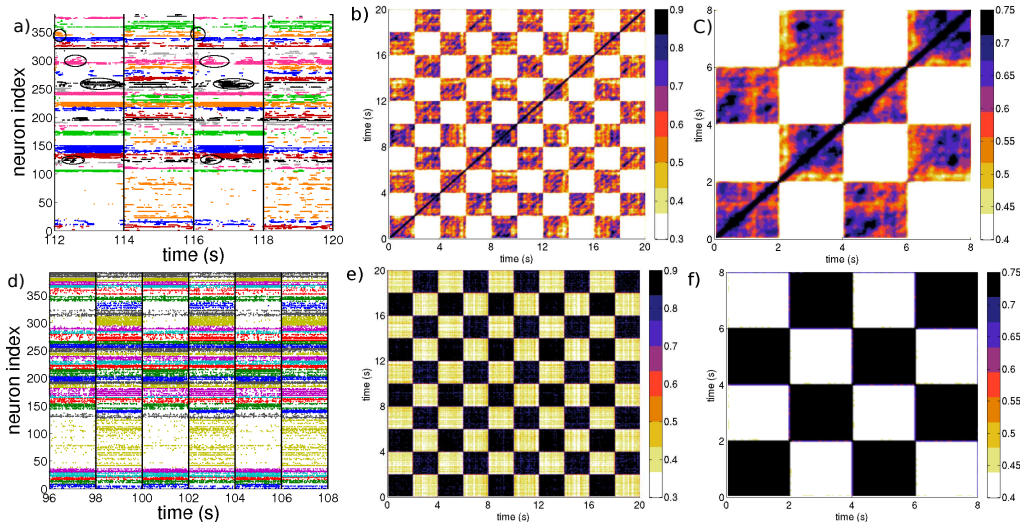

Figure 4.10: **Sequential switching.** For $\tau_\alpha = 20$ ms: a) Raster plot associated to the two input protocols $I^{(1)}$ and $I^{(2)}$. The circles denote the clusters of active neurons appearing repetitively after the presentation of the stimulus $I^{(1)}$. Vertical lines denote the switching times between stimuli. b) State Transition Matrix $\chi(m,n)$ calculated over a time span of 20 seconds. c) Averaged State Transition Matrix $\langle\chi\rangle$, obtained by considering a $4T_{sw} \times 4T_{sw}$ sub-matrix averaged over $r = 5$ subsequent time windows of duration $4T_{sw}$. d-f) same as a-c) for $\tau_\alpha = 2$ ms. In both cases, the inputs $I^{(1)}$ and $I^{(2)}$ are different realization of the same random process, they are obtained by selecting N current values I_i from the flat interval $[V_{th}, V_{th} + \Delta V]$. The input stimuli are switched every $T_{sw} = 2$ s. Number of clusters $k = 35$ in a). Other parameters as in Fig. 4.1.

To test for the presence of memory effects influencing the network response, we performed a further test where the system dynamics was completely reset after each stimulation and before the presentation of the next stimulus. We do not observe any relevant change in the network response, so we can conclude that our results are robust.

Next, we examined the influence of the PSP time scale on the observed results. In particular, we considered the case $\tau_\alpha = 2$ ms, for this value the network does not reveal a large variability in the response showing a reduced number of patterns of activity. In particular, as shown in Fig. 4.10(d) it responds in a quite uniform manner during the presentation of each stimulus. Furthermore, the corresponding STM and the averaged version reported in Figs. 4.10(e) and (f) show highly correlated blocks alternating to low correlated ones, but these blocks do not reveal any internal structure typical of cell assembly encoding.

We proceeded to check the ability of the network to discriminate among similar inputs and how this ability depends on the temporal scale of the synaptic response. In particular, we tried to answer to the following question: if we present two inputs that differ only for a fraction f of the stimulation currents, which is the minimal difference between the inputs that the network can discriminate ? In particular, we considered a control stimulation $I^{(c)} = I_i \in [V_{th}, V_{th} + \Delta V]$ and a perturbed stimulation $I^{(p)}$, where the stimulation currents differ only over a fraction f of currents I_i (which are randomly chosen from the same distribution as the control stimuli). We measure the differences of the responses to the control and to the perturbed stimulations by measuring, over an observation window T_e, the dissimilarity metric $d^f(t)$, this can be seen in Figs. 4.11(a) and (b) fro two values of T_e. In each figure we report the dissimilarity metric for two different values of PSP duration, namely $\tau_\alpha = 20$ ms (black circled line) and $\tau_\alpha = 2$ ms (red squared line).

The time averaged dissimilarity metric $\langle d \rangle^f$ is reported as a function of f in Fig. 4.11(c) for the two different values τ_α. It is clear that for any f-value the network with longer synaptic response always discriminates better between the two different stimuli than the one with shorter PSP decay.

In order to better characterize the computational capability of the network and the influence due to the different duration of the PSPs, we measure the complexity of the output signals as recently suggested in [144]. In particular, we have examined the response of the network to a sequence of three stimuli, each being a constant vector of randomly chosen currents. The three different stimuli are consecutively presented to the network for a time period T_{sw}, and the stimulation sequence is repeated for the whole experiment duration T_E. The output of the network can be represented by the instantaneous firing rates of the N neurons measured over a time window $\Delta T = 100$ ms, this is a high dimensional signal, where each dimension is represented by the activity of a single neuron. The complexity of the output signals can be estimated by measuring how many dimensions are explored in the phase space, more stationary are the firing rates less variables are required to reconstruct the whole output signal [144].

A principal component analysis (PCA) performed over $T_E/\Delta T$ observations of the N firing rates reveals that for $\tau_\alpha = 2$ ms the 80% of the variance is recovered already with a projection over a two dimensional sub-space (red bars in Fig. 4.12

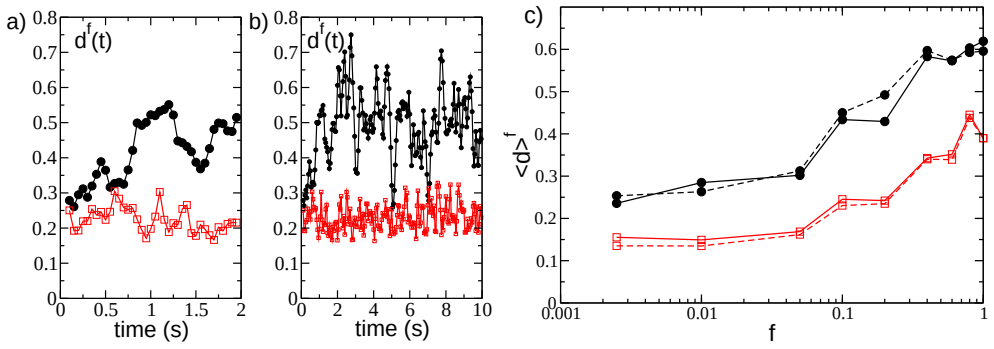

Figure 4.11: **Pattern separation.** Dissimilarity measure in time with an observation window of length a) $T_e = 2$ and b) $T_e = 10$, for the values of $\tau_\alpha = 20$ms (black circles) and $\tau_\alpha = 2$ms (red squares) and at a fixed value of $f = 0.2$. c) Average dissimilarity as a function of the fraction f of inputs differing from the control input, for the two studied values of τ_α, with an observation window $T_e = 2$ s . Other parameters used: $\Delta T = 50$ms, $\Delta V = 5$ mV. Remaining parameters as in Fig. 4.1.

(a)). On the other hand, for $\tau_\alpha = 20$ ms a higher number of principal components is required to reconstruct the dynamical evolution (black bars in Fig. 4.12 (a)), thus suggesting higher computational capability of the system with longer PSPs [144].

These results are confirmed by analyzing the projections of the firing rates in the subspace spanned by the first three principal components $(C1, C2, C3)$ shown in Fig. 4.12 (b) and (c) for $\tau_\alpha = 20$ ms and $\tau_\alpha = 2$ ms, respectively. The responses to the three different stimuli can be effectively discriminated by both networks, since they lie in different parts of the phase space. However, the response to the three stimuli correspond essentially to three fixed points for $\tau_\alpha = 2$ ms, while trajectories evolving in a higher dimension are associated to each constant stimulus for $\tau_\alpha = 20$ ms.

These analyses confirm that the network parameters selected by employing the maximal Q_0 criterion also result in a reproducible response to different stimuli, as well as in an effective discrimination between different inputs.

4.3.8 Physiological relevance for biological networks under different experimental conditions

The analysis here reported has been inspired by the experiment performed by Carrillo *et al.* [48]. In that experiment the authors considered a striatal network *in vitro*, which displays sporadic and asynchronous activity under control conditions. To induce spatio-temporal patterned activity they perfused the slice preparation with N-methyl-D-aspartate (NMDA). Since it is known that NMDA administration brings about an excitatory tonic drive with recurrent bursting activity [145, 146]. The crucial role of the synaptic inhibition in shaping the patterned activity in striatal dynamics is also demonstrated in [48], by applying the $GABA_a$ receptor antagonist bicuculline to effectively decrease the inhibitory synaptic effect.

In our simple model, ionic channels and NMDA-receptors are not modeled; nevertheless it is possible to partly recreate the effect of NMDA administration

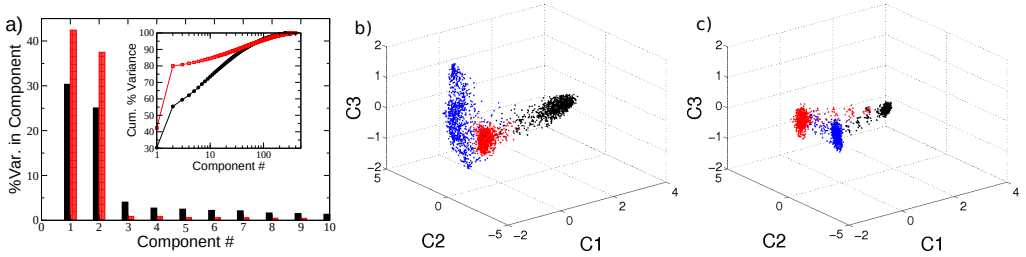

Figure 4.12: **Computational capability of the network.** Characterization of the firing activity of the network, obtained as response to three consecutive inputs presented in succession. a) Percentage of the variance of the neuronal firing activity reproduced by each of the first 10 principal components. The inset displays the corresponding cumulative percentage as a function of the considered component. Filled black and shaded red (bar or symbols) correspond to $\tau_\alpha = 20$ ms and $\tau_\alpha = 2$ ms, respectively. Projection of the neuronal response along the first three principal components for b) $\tau_\alpha = 20$ ms and c) $\tau_\alpha = 2$ ms. Each point in the graph correspond to a different time of observation. The three colors denote the response to the three different inputs, which are quenched stimulation currents randomly taken as $I^{(j)} \in [V_{th}, V_{th} + \Delta V]$ for $j = 1, 2, 3$, the experiment is then performed as explained in the text.

by increasing the excitability of the cells in the network, and the effect of the bicuculline as an effective decrease in the synaptic strength. We then verify *at posteriori* whether these assumptions lead to results similar to those reported in [48].

In our model the single cell excitability is controlled by the parameter I_i. The computational experiment consists in setting the system in a low firing regime corresponding to the control conditions with $I^{(c)} = \{I_i^{(c)}\} \in [-53, -49.5]$ mV and in enhancing, after 20 seconds, the system excitability to the range of values $I^{(e)} = \{I_i^{(e)}\} \in [-60, -45]$ mv, for another 20 seconds. This latter stage of the numerical experiment corresponds to the NMDA bath in the brain slice experiment. The process is repeated several times and the resulting raster plot is coarse grained as explained in Methods (sub-section *Synchronized Event Transition Matrix*).

From the coarse grained version of the raster plot, we calculate the *Network Bursting Rate* (NBR) as the fraction of neurons participating in a burst event in a certain time window. Whenever the instantaneous NBR is larger than the average NBR plus two standard deviations, this is identified as a *synchronized bursting event* (as shown in Fig. 4.13(a) and (f)). In Fig. 4.13(b) we plot all the neurons participating in a series of $S_s = 20$ synchronized bursting events. Here the switching times between control conditions and the regimes of increased excitability are marked by vertical dashed lines. Due to the choice of the parameters, the synchronized events occur only in the time intervals during which the network is in the enhanced excitability regime. Each synchronized event is encoded in a binary N dimensional vector $W_s(t)$ with 1 (0) entries indicating that the corresponding neuron was active (inactive) during such event. We then measure the similarity among all the events in terms of the *Synchronized Event Transition Matrix* (SETM) shown in Fig. 4.13(c). Furthermore, using the SETM we divide the synchronized events

into clusters according to an optimal clustering algorithm [58]. In the present case we have identified 3 distinct *states* (clusters), if we project the vectors W_s, characterizing each single synchronized event, on the two dimensional space spanned by the first two principal components $(C1, C2)$, we observe a clear division among the 3 states (see Fig. 4.13(d)). It is now important to understand whether the cells firing during the events classified as a state are the same or not. We observe that the groups of neurons recruited for each synchronized event, corresponding to a certain state, largely overlap, while the number of neurons participating to different states is limited. As shown in Fig. 4.13(e), the number of neurons participating to the events associated to a certain state is of the order of 40-50, while the coactive neurons (those participating in more than one state) ranges from 12 to 25. Furthermore, we have a core of 9 neurons which are firing in all states. Thus we can safely identify a distinct assembly of neurons active for each state.

As shown in Fig. 4.13(c), we observe, in analogy to [48], that the system alternates its activity among the previously identified cell assemblies. In particular, we have estimated the transition probabilities from one state to any of the three identified states. We observe that the probability to remain in state 2 or to arrive to this state from state 1 or 3 is quite high, ranging between 38 and 50 %, therefore this is the most visited state. The probability that two successive events are states of type 1 or 2 is also reasonably high ranging from $\simeq 29 - 38\%$ as well as the probability that from state 1 one goes to 2 or viceversa ($\simeq 38 - 43\%$). Therefore the synchronized events are mostly of type 1 and 2, while the state 3 is the less *attractive*, since the probability of arrving to this state from the other ones or to remain on it once reached, are between 25 - 29 %. If we repeat the same experiment after a long simulation interval $t \simeq 200$ s we find that the dynamics can be always described in terms of small number of states (3-4), however the cells contributing to these states are different from the ones previously identified. This is due to the fact that the dynamics is in our case chaotic, as we have verified in subsection (*Linear Stability Analysis*). Therefore even small differences in the initial state of the network, can have macroscopic effects on sufficiently long time scales.

To check for the effect of bicuculline, the same experiment is performed again with a much smaller synaptic coupling, namely $g = 1$, the results are shown in Fig. 4.13(f-j). The first important difference can be identified in higher NBR values with respect to the previous analyzed case ($g = 8$) Fig. 4.13(f). This is due to the decreased inhibitory effect, which allows most of the neurons to fire almost tonically, and therefore a higher number of neurons participate in the bursting events. In Fig. 4.13(g) it is clearly visible a highly repetitive pattern of synchronized activity (identified as state 2, blue symbols), this state emerges immediately after the excitability is enhanced. After this event we observe a series of bursting events, involving a large number of neurons (namely, 149), which have been identified as an unique cluster (state 1, red symbols). The system, analogously to what shown in [48], is now locked in an unique state which is recurrently visited until the return to control conditions. Interestingly, synchronized events corresponding to state 1 and state 2 are highly correlated when compared with the $g = 8$ case, as seen by the SETM in Fig. 4.13(h). Despite this, it is still possible to identify both states when projected on the two dimensional space spanned by the first two principal components (see Fig. 4.13(i)). This high correlation can be easily explained

by the fact that the neurons participating in state 2 are a subset of the neurons participating in state 1, as shown in Fig. 4.13(j). Furthermore, the analysis of the transition probabilities between states 1 and 2 reveals that starting from state 2 the system never remains in state 2, but always jumps to state 1. The probability of remaining in state 1 is really high $\simeq 64\%$. Thus we can affirm that in this case the dynamics is really dominated by the state 1.

To determine the statistical relevance of the results presented so far, we repeated the same experiment for ten different random realizations of the network, We found that, while the number of identified states may vary from one realization to another, the persisting characteristics that distinguish the NMDA perfused scenario and the decreased inhibition one, are the variability in the SETM and the fraction of coactive cells. More precisely, on one hand the average value of the elements of the SETM is smaller for $g = 8$ with respect to the $g = 1$ case, namely 0.54 versus 0.84, on the other hand their standard deviation is larger, namely 0.15 versus 0.07. Thus indicating that the states observed with $g = 1$ are much more correlated among them with respect to the states observable for $g = 8$, which show a larger variability. The analysis of the neurons participating to the different states revealed that the percentage of neurons coactive in the different states passes from 51 % at $g = 8$ to 91 % at $g = 1$. Once more the reduction of inhibition leads to the emergence of states which are composed by almost the same group of active neurons, representing a dominant state. These results confirm that inhibition is fundamental to cell assembly dynamics.

Altered intrastriatal signaling has been implicated in several human disorders, and in particular there is evidence for reduced GABAergic transmission following dopamine depletion [147], as occurs in Parkinson's disease. Our simulations thus provide a possible explanation for observations of excessive entrainment into a dominant network state in this disorder [148, 126].

4.4 Final Summary

In summary, we have shown that lateral inhibition is fundamental for shifting the network dynamics from a situation where a few neurons, tonically firing at a high rate, depress a large part of the network, to a situation where all neurons are active and fire with similar slow rates. In particular, if inhibition is too low, or too transient, *winner takes all* mechanism is at work and the activity of the network is mainly mean-driven. By contrast, if inhibition has realistic strength and duration, almost all the neurons are on average sub-threshold and the dynamical activity is fluctuation-driven [21].

Therefore we can reaffirm that the MSN network is likely capable of producing slow, selective, and reproducible activity sequences as a result of lateral inhibition. The mechanism at work is akin to the *winerless competition* reported to explain the functioning of olfactory networks in order to discriminate different odors [149]. Winnerless competition refers to a dynamical mechanism, initially revealed in asymmetrically coupled inhibitory rate models [150], displaying a transient slow switching evolution along a series of metastable saddles (for a recent review on the subject see [151]). In our case, the sequence of metastable states can be represented by the firing activity of the cell assembly, switching over time.

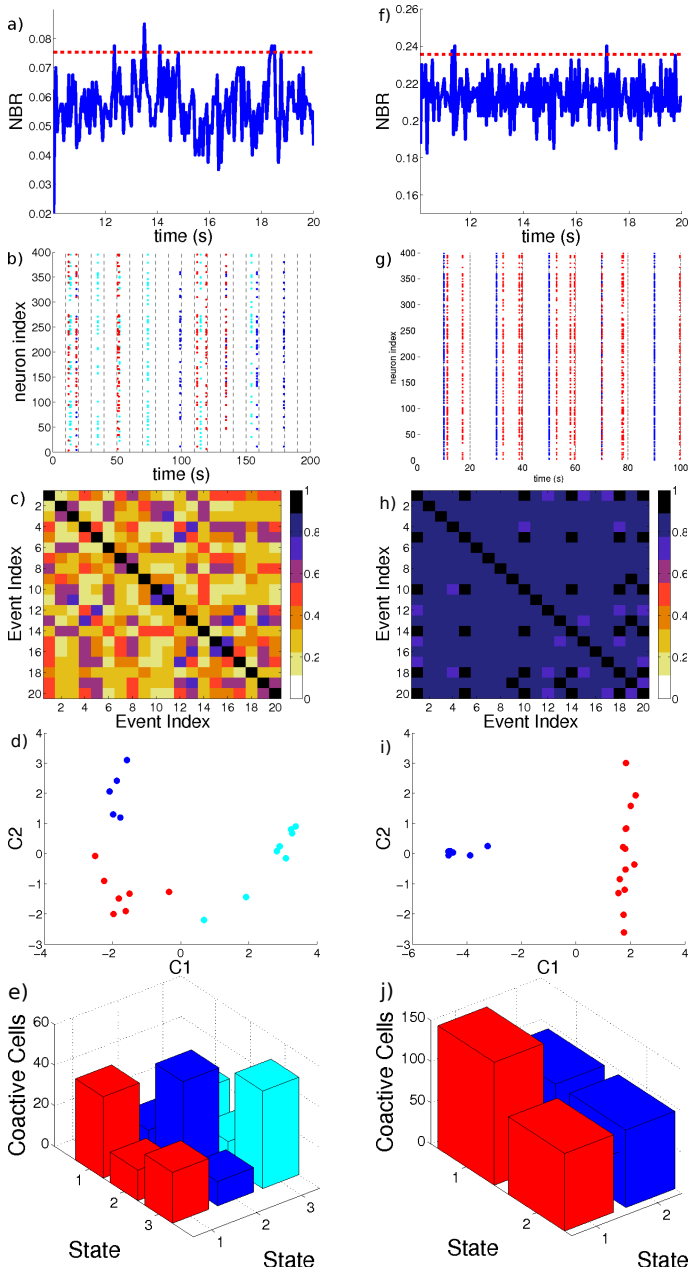

Figure 4.13: **Response of the network to an increase in the excitability.** a,f) Network Bursting Rate, and the threshold defined for considering a synchronized event. b,g) Neurons involved in the synchronized events, vertical lines denoted the switching times between the excited $I^{(e)}$ and control $I^{(c)}$ inputs. Colors in the raster indicates the group assigned to the synchronous event using an optimal community partition algorithm. c,h) Synchronized Event Transition Matrix, calculated with a window $T_W = 50$ ms and number of events $S_s = 20$. d,i) Projection of the synchronized events in the 2D space spanned by the first two principal components associated to the covariance matrix of the vectors W_s. e,j) Number of coactive cells in each state. The diagonal elements of the bar graph represents the total number of neurons contributing to one state. Panels (a-e) correspond to $g = 8$, while panels (f-j) depict the case $g = 1$. In both cases the system is recorded during the time span required to identify $S_s = 20$. Remaining parameters as in Fig. 4.1.

In particular, as in our analysis, slow synapses have been recognized as a fundamental ingredient, besides asymmetric inhibitory connections, to observe the emergence of winnerless competition in realistic neuronal models [152, 153].

We have introduced a new metric to encompass in a single indicator key aspects of this patterned sequential firing, and with the help of this metric we have identified the values of the parameters entering in the model to best obtain these dynamics. Furthermore, for the same choice of parameters the network is able to respond in a reproducible manner to the same stimulus, presented at different times, while presenting complex computational capability by responding to constant stimuli with an evolution in a high dimensional space [144].

Our analysis has revelealed that the IPSP/IPSC duration is crucial in order to observe bursting dynamics at the single cell level as well as structured assembly dynamics at the population level. A reduction of the synaptic time has been observed in symptomatic HD mice [125], in our model this reduction leads single neurons towards a Poissonian behaviour and to a reduced level of correlation/anticorrelation among neural assemblies, in agreement with experimental results reported for mouse models of HD [46].

In summary, we have been able to reproduce general experimental features of MSN networks in brain slices [48]. In particular, we have observed, as in the experiment, a structured activity alternating among a small number of distinct cell assemblies. Furthermore, we have reproduced the dynamical effects induced by decreasing the inhibitory coupling: the drastic reduction of the inhibition leads to the emergence of a dominant highly correlated neuronal assembly. This may help account for the dynamics of Parkinsonian striatal microcircuits, where dopamine deprivation impairs the inhibitory feedback transmission among MSNs [147, 126].

The results presented in this chapter have been published in Ref. [154].

Chapter 5

Conclusions

Throughout this dissertation we examined the α-pulse coupled Leaky Integrate and Fire network as a relevant model accounting for biological observations in the neuroscience's field. In doing so, we studied in detail the role of the structural properties (parameters) of the α-LIF model in shaping the dynamics in three experimentally inspired applications: i) Chapter 2 provided a theoretical substrate to understand the role of sparse connectivity in generating non-trivial dynamics in excitatory networks, akin to the *Giant Depolarizing Potentials* (GDP) in developing hyppocampal networks. ii) In chapter 3 it was analyzed the importance of inhibition as the origin of irregular spiking and perturbation amplification of balanced neural networks, which are prototypical of *cortical dynamics*. iii) In chapter 4, it was described how sparse connectivity, inhibition and synaptic dynamics can provide the conditions of emergence of cell assembly dynamics, which are related to the encoding mechanism observed in the *striatum*.

We started by considering the simplest case of an excitatory network of α-pulse coupled LIF neurons displaying a partially synchronized (PS) regime (chapter 2). It is known that this type of system is non-chaotic when it is globally coupled [83]. Removing links between the neurons in the network induces fluctuations in the synaptic drive and chaotic behavior emerges [66]. However, the question whether these two observations had a causal relation remained elusive. We found that the statistical properties of a deterministic neural network with broken links can be exactly described in terms of an equivalent fully coupled circuit plus an additive noise term mimicking the current fluctuations. This was demonstrated by comparing the statistics of the fields appearing in the α-LIF model (macroscopic variables) and the distribution of Insterspike Intervals (microscopic variables) of the determinsitic and stochastic model. Also the stability properties, quantified by the Maximal Lyapunov Exponent (MLE) were retrieved with the stochastic formulation. Analyzing the fluctuations at deterministic level, we discovered that in order to reproduce these fluctuations in a stochastic formulation we should include noise terms presenting time correlations as well as amplitudes depending on the state of the system. This stochastic formulation reduced considerably the dimensionality of the system and therefore the computation time of the MLE. These results allowed us to conclude that indeed the fluctuations of the field are responsible for the chaotic motion in this system. This kind of models might be

useful to account for the presence of global oscillations at population level in developing brain networks, in the form of GDPs [62]. During this developing period, GABAergic interneurons have a depolarizing role which leads the immature neural circuits to a synchronized activity, similar to the ones observed in the PS regime. However, it is important to remark that the topologies studied in this chapter are random networks, while some evidences found in studies on GDP generation in the CA3 region of the hippocampus have shown that the functional connectivity of the developing neurons might not follow random distributions [63]. Whether our results can be extended to a more complex connectivity such as scale-free or small world networks remains an open problem.

We verified that the picture of well organized dynamics in purely excitatory circuits changes dramatically when inhibition is considered. In chapter 3 we examined a sparsely connected neural network subjected to inhibitory feedback. This system is of particular importance since it is one of the simplest cases of balanced activity, in which external excitation is counteracted by feedback inhibition and the activity of the neurons is driven by fluctuations. Models of balanced activity have been used to simulate activity in the cortex, which presents large variability in the spiking times with coefficient of variation (CV) close to one [92]. Using the α-pulse coupled network we discovered that, in contrast to the regular dynamics emerging in a purely excitatory network, the inhibitory network is highly irregular ($CV \approx 1$). We showed that for fast synapses the system is not chaotic while slow ones produce a transition to a chaotic state, in any case the irregularity in the spiking dynamics is preserved regardless the chaotic nature of the system. If irregularity cannot be ascribed to the presence of chaos, what are the mechanisms that produces this type of behavior? Applying non-linear stability tools [101, 106], we discovered that in the fluctuation driven regime, finite size perturbations are amplified faster than infinitesimal ones, in contrast to the excitatory system. These results are supported by similar findings in the context of exponentially coupled synapses [60]. As a consequence of these non-linear instabilities, even if the system is linearly stable, an irregular evolution can arise [59]. The explanation for this seemingly counter-intuitive observation of stable irregular dynamics, is that of the *Stable Chaos*. Our non-linear stability analysis indeed supports this interpretation, as it is known that for systems subject to stable chaos, the Finite Size Lyapunov Exponent is larger than the MLE [59]. Similar interpretations have been reported in the context of δ-pulse coupled neurons where the same phenomenon is described in terms of reservoirs of stability of variable size according to the network scale, termed dynamic flux tubes [86]. One of the most interesting points of discussion of this chapter is that we provided insights to a new interpretation to the experimental results presented in [42]. There, the authors studied the activity of the rat's barrel cortex *in-vivo* subject to perturbations: Several measurements of the network dynamics under the same experimental conditions led to the same outcome (particularly the number of spikes emitted by the network). However, a perturbation amounting to the removal of a single spike in one of the repetitions produced an amplification of the initial perturbation, claiming the chaotic essence of this system. Nonetheless, our theoretical analysis clearly reveals that a finite perturbation (for example of the order of the single spike) can be amplified despite

the non-chaotic nature of the system. It shall be noticed that the results reported in chapter 3 were found by considering solely inhibitory feedback, in which the excitatory effect is captured by the constant driving DC current. Unfortunately this restricts the biological significance of the results since it is known that cortical circuits are mainly composed (80%) by excitatory pyramidal neurons and only 20% are GABAergic inhibitory interneurons [36]. This means that synaptic dynamics of the excitatory component present in a real network might potentially have an important role in the non-linear aspects of the network, which are not accounted for in our analysis. We hope that this issues can be solved in further investigations.

In chapter 4, we focused our attention in the study of striatal dynamics. The striatum, the main input to the basal ganglia, plays an important role in motor control and reward based learning, and the disruption of information signaling at striatal level is at the base of disorders such as Parkinson's and Huntington's diseases (PD and HD respectively). The striatum is formed by a sparsely and weakly connected circuit of GABAergic Medium Spiny Neurons (MSNs), and its dynamics is organized in groups of neurons firing coherently within a family while firing in an anti-correlated way with other groups of neurons. Although some detailed models have been proposed to account for the striatum activity (see [142, 123, 122, 121]), we showed that a minimal model of pulse coupled LIF neurons is able to reproduce the most relevant aspects of striatal dynamics. By proposing a novel indicator, we singled out the role of synaptic transmission parameters in shaping the striatal-like dynamics and we demonstrated the direct relation between cell assembly formation and the underlying topology of the network. Interestingly, we discovered that the range of parameters at which the network exhibits the desired behavior (in particular connectivity values, lateral inhibition strength and post-synaptic current duration), closely corresponds to experimental values reported for the MSN. Also, the MSN-like activity emergence seems to be related to the presence of weak chaos. We found that the inhibitory post-synaptic potential (IPSP) time scale is fundamental for the emergence of bursting dynamics. Reducing the IPSP drives the neurons to a Poisson like behavior and consequently to a reduction of the cell assembly structure, as observed in HD symptomatic mice [46, 125]. Finally, we were able to reproduce general experimental features of striatal dynamics *in-vitro* reported in [48]. In this paper the authors describe the response of the striatum in presence of NMDA as the alternating activity of a few number of cell assemblies, as we observed in our model. In the same study, the effect of reduced inhibitory coupling is characterized by the emergence of a dominant assembly, and this effect was also captured with our model. Reduced inhibitory coupling is related to Parkinsonian striatum, where the disruption of dopamine (DA) release, diminishes the strength of lateral inhibition among MSNs [147, 126]. It is important to remark that the striatal circuitry and its interaction with the basal ganglia is a highly complex system. For instance, the different effects of DA depending on the DA receptor in MSNs, the effect of fast spiking neurons, and the spike timing dependent plasticity at the cortico-striatal projection synapses are some aspects of the striatal dynamics not accounted by our model. Whether our results persist in complex models with more detailed dynamics is an open question. Nevertheless, network models such as the one presented here may offer a path towards

understanding how pathologies that affect single neurons lead to aberrant network activity patterns, as seen in PD and HD, and this is an exciting direction for future research.

Altogether we can conclude that the α-pulse coupled LIF model, despite its simplicity, has allowed us to reveal and analyze new collective dynamical behaviors which can be relevant in the context of developing hyppocampal networks, cortical, and striatal dynamics. Such a model is a trade-off in which sub-threshold behavior is simplified and action potential generation is completely disregarded, but it is possible to maintain a particularly important feature of real neural systems: the synaptic dynamics. In particular, we have verified that synaptic properties such as strength and time scale are crucial to determine the emergence of specific evolutions related to experimental observations, which cannot be accounted by networks with no synaptic dynamics. The stability analysis of the observed collective dynamical evolutions shed light on how different manifestations of chaos might generate useful dynamical regimes from a biological perspective, allowing for information encoding at the population level.

The results presented here led to three publications: Refs. [90, 87] in collaboration with A. Torcini, and Ref. [154] in collaboration with J.D Berke and A. Torcini.

Appendix A

Serial and parallel numerical implementation of the Event Driven Map

In this appendix an outline of the algorithm implementation to solve the Event Driven Map of the LIF model coupled with α-pulses is presented. The analytic form of the solution for the next firing time $\tau(n)$ of each cell is given by the implicit function (2.5), (3.6) and (4.2) which needs to be solved numerically for each of the N neurons. This is done by using standard zero finding algorithms of the function:

$$f(\tau) = \tau - \ln\left[\frac{a - v_m(n)}{a + gH_m(n) - 1}\right] \tag{A.1}$$

The solution of such a large set of equations is computationally inefficient, specially when dealing with large networks. Here we present a (serial) algorithm to overcome such inefficiency inspired by the algorithm outlined in [155]:

S1 At each step of the algorithm, the membrane potentials are sorted in descending order with an indexing routine [156].

S2 With a high probability, the next firing time solution will be found in a small fraction of the closest-to-threshold membrane potential. Therefore, only a subset (pool) consisting of the $M << N$ closest-to-threshold neurons are chosen to be solved their firing times.

S3 To avoid fictitious zeros and guaranteeing convergence to the minimal τ_m in the solution of the M equations, an outward bracketing routine is performed to find only the first zero-crossing of the function $f(\tau)$ in the domain $[0\ , x_B]$, by evaluating the function through N_B equally spaced intervals of size $\Delta_B = (x_B - 0)/N$, starting from 0 and checking for the first sign change in x_l. This will tell us that the real solution (the first one) is bracketed in the subinterval $[x_l - \Delta_B\ , x_l]$. A final bisection method is used in this small bracket to find a solution with some selected accuracy.

S4 The system is evolved during the found τ_m, if all the neurons remained under threshold, the solution is correct and the algorithm is repeated from step one,

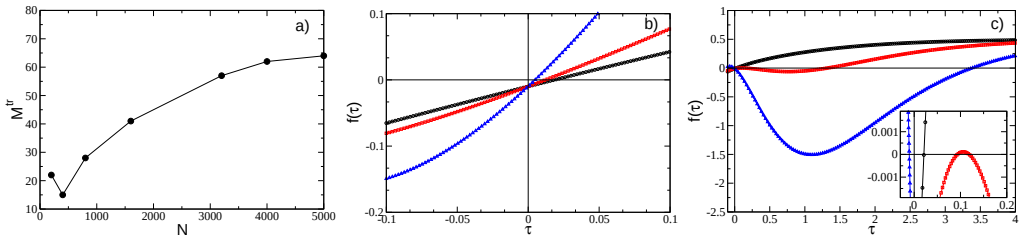

Figure A.1: a) Trained value of the pool size M^{tr} for different sizes of the network, growing sub-linearly with N. The value of M^{tr} in this case is chosen to be the average plus two standard deviations. b) Prototypical shape of equation A.1 for an excitatory network: The solutions are bounded in a precise domain for any value of g, in the plot $g = 0.1$ (black), $g = 1$ (red), $g = 5$ (blue). c) Same as in b) for an inhibitory network (negative values of g); inset: close-up of the functions near the origin. Parameters used in a) $\alpha = 5$, $g = -8$, $K = 20$, $a = 1.5$, b) and c) $\alpha = 2$, $a = 1.5$, $K = 20$, $P = 60$, $E = 6$, $x_m = 0.9901$

otherwise the previous state is recovered and the algorithm is repeated by choosing a larger set $M \sim \mathcal{O}(N)$, with a larger bracketing boundary $5 \times x_B$ divided in a larger number of sub-intervals $10 \times N$.

S5 The algorithm is repeated from step S1.

From the algorithm above, it is clear that the selection of the size of the pool M, the bracketing limit x_B and the number of bracketing intervals N_B are somehow arbitrary. The last of them is chosen intuitively as $N_B = N$, since we assume that an increase of the number of neurons needs also a much more fine grained zero-seeking intervals. On the other hand, M and x_B can be "taught" to the network during a slow training period, where a safe set of untrained parameters M, x_B are introduced in the evolution (those of step S4, for example). Allowing a small number of spikes compared with the actual simulation time, we can check on average what is the actual (trained) number M^{tr} of neurons that the algorithm needs to solve on average until finding the correct answer, as well as the maximal x_B^{tr} that the algorithm calculated. These two trained values are then used for the remaining simulation time.

As illustrated in figure A.1, the pool of neurons increases sub-linearly with the system size. Our approach (from now on termed Algorithm 2 in contrast to the original Algorithm 1 proposed in [155]), leads to an improvement from the view point of the number of routine calls to the zero-finding algorithms. In Algorithm 1, the sub-pool is set to be proportional to N (more precisely $M = N/10$), which is not an efficient selection of M, as discussed before. Such an inefficiency is, however, counterweight by performing the sorting routine each I steps, since it is assumed a more or less organized nature of firing in excitatory networks, which allowed the author to update the network during I steps without changing significantly the list of the closest-to-threshold neurons, and therefore assuring the existence of the solution in the same pool of the previous iterations. Under that assumption one would expect that the system evolves without failure for a fairly

			Zero find		
N	*evo*	*idx*	*bisect*	*zbrak*	Col 4 + Col 5
500	9.9	8.3	45.8	33.6	80.2
1000	13.9	10.2	30.4	40.4	72.1
2000	8.2	8.5	23.0	55.9	79.8
4000	17.4	4.7	10.2	64.1	74.9
8000	10.6	2.7	6.0	77.1	83.6

Table A.1: Profiling information of the algorithm described at the beginning of this appendix, with $M = N/10$ and $x_B = 1$. The values in the table correspond to the percentage of total time spent in each one of the routines in the algorithm (*evo* = update of the network, *idx* = sorting of the potentials, *bisect* = bisection of the bracketed solution, *zbrak* = bracketing of the solution).

smart choice of parameters. Unfortunately when dealing with inhibitory networks, due to the high irregularity in the firing, and the fact that the inhibitory feedback may push out the membrane potentials far from the threshold in a single iteration, the assumption of the unchanged list is not always true and a reorganization of the membrane potentials is required at each step.

Also in Algorithm 1, bracketing and bisection methods are simplified with a Newton-Rapson (NR) routine, leading to better performances respect to those obtained with the routines that we have chosen. It can be seen, indeed from the profiling information in Table A.1 that most of the running time is spent in the zero-finding routines (between 70% and 80%). However, the assumption underlying the selection of a NR routine in Algorithm 1 relies on the fact that for current driven networks (purely excitatory) the prototypical shape of function $f(\tau)$ is much simpler than the inhibitory counter-part, as depicted in Fig. A.1b). As seen in this picture a single zero-cross of the function exists for a large range of parameters, meaning that the real solution is guaranteed to be found at any time in some (small) bounded region with no ambiguity. Conversely, for a fluctuation driven network (inhibitory) the panorama changes drastically as seen in Fig. A.1 c). In such a case a whole different collection of scenarios may appear depending on the values of the parameters: i) single solution at small τ (black symbols), ii) single solution at large τ (blue symbols) iii) multiple solutions solutions close to each other (red symbols). Each one these scenarios justifies the use of rather different (and slower) zero-finding routines.

In figure A.2 a) we show the performance of Algorithm 1, compared with the Algorithm 2, for a given set of parameters and different sizes of the network. All the tests were performed on an AMD Opteron 6164HE server with 24 Cores running at 1700 MHz.

Parallelization of the algorithm

A further improvement can be obtained by parallelizing the algorithm. The event driven map for the case of α-pulse coupled system can be parallelized through T

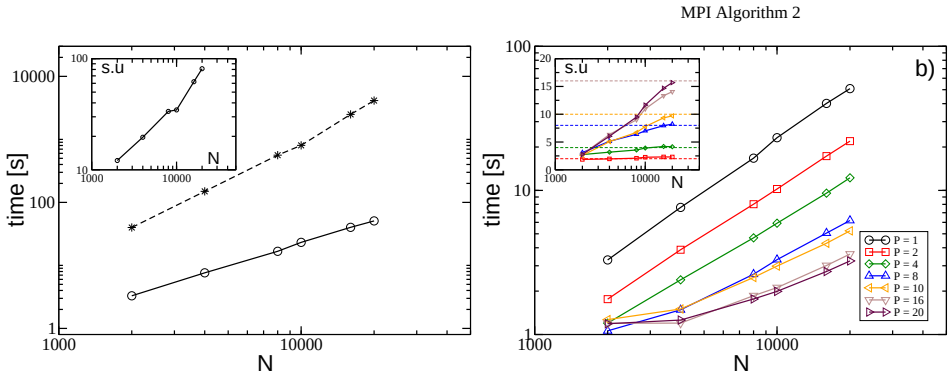

Figure A.2: Comparison of performance of Algorithm 1 (dashed line) and Algorithm 2 (solid line) for several values of N; inset: speed up factor (s.u) calculated as the running time of Algorithm 2 divided by the time of Algorithm 1. b) Performance of the parallelized version of Algorithm 2 for several number of processors; inset: the speed up is obtained by dividing the time taken by the serial code divided by the time taken by the parallelized version. In both figures the system is evolved for 10^5 spikes using the following parameters: $K = 20$, $\alpha = 9$, $g = 0.3$, $a = 1.5$. The times of simulation for the Algorithm 2 is considered after performing the training section, which is assumed to take much less time respect to the actual simulation time.

tasks (processes or threads) by assigning to each task a subset $n = N/T$ of neurons to perform computations.

P1 Each task sorts n neurons in descending order.

P2 Each task seeks in a small pool $M^{tr} << n$ the shortest firing time solution form its own subset.

P3 Each task communicates the partial solutions τ_m^T and the corresponding neuron m^T to a master task T_0 that chooses the minimum among the partial results.

P4 Master task T_0 sends the final τ_m and the corresponding m to all the other tasks.

P5 Each task is updated independently and returns a signal of success / fail to the master task T_0 and waits for a go (repeat) signal.

P6 Master task checks if any fail and communicates a repeat signal to the other tasks, otherwise communicate a go signal.

P7 Each task checks if there is a repeat signal, if so all tasks retrieve the past state and repeats the algorithm form step (1) with $M \sim \mathcal{O}(n)$, $5 \times x_B$ divided in a larger number of sub-intervals $10 \times n$.

P8 Each task repeats algorithm from step P1.

The algorithm outlined above is general for any paralleling method. One could choose to apply it on an OpenMP framework (shared memory paradigm, in which case the tasks are threads) or with MPI libraries (distributed memory paradigm, where each task is an indeed independent process) [157]. In figure A.2 b) it is shown the performance of the parallel algorithm for several number of tasks.

Bibliography

[1] Amiram Grinvald and Rina Hildesheim. Vsdi: a new era in functional imaging of cortical dynamics. *Nature Reviews Neuroscience*, 5(11):874–885, 2004.

[2] S Chemla and F Chavane. Voltage-sensitive dye imaging: Technique review and models. *Journal of Physiology-Paris*, 104(1):40–50, 2010.

[3] Per E Roland. Dynamic depolarization fields in the cerebral cortex. *TRENDS in Neurosciences*, 25(4):183–190, 2002.

[4] Abraham Z Snyder and Marcus E Raichle. Studies of the human brain combining functional neuroimaging and electrophysiological methods. *Simultaneous EEG and fMRI: Recording, Analysis, and Application*, pages 47–66, 2010.

[5] Alain Destexhe and Thierry Bal. *Dynamic-clamp: from principles to applications*, volume 1. Springer Science & Business Media, 2009.

[6] Rodrigo Quian Quiroga and Stefano Panzeri. *Principles of neural coding*. CRC Press, 2013.

[7] Alan L Hodgkin and Andrew F Huxley. A quantitative description of membrane current and its application to conduction and excitation in nerve. *The Journal of physiology*, 117(4):500–544, 1952.

[8] Alan L Hodgkin and Andrew F Huxley. Propagation of electrical signals along giant nerve fibres. *Proceedings of the Royal Society of London. Series B, Biological Sciences*, pages 177–183, 1952.

[9] Alan L Hodgkin, Andrew F Huxley, and B Katz. Measurement of current-voltage relations in the membrane of the giant axon of loligo. *The Journal of physiology*, 116(4):424, 1952.

[10] Alan L Hodgkin and Andrew F Huxley. The dual effect of membrane potential on sodium conductance in the giant axon of loligo. *The Journal of physiology*, 116(4):497–506, 1952.

[11] Alan L Hodgkin and Andrew F Huxley. Currents carried by sodium and potassium ions through the membrane of the giant axon of loligo. *The Journal of physiology*, 116(4):449–472, 1952.

[12] Wulfram Gerstner and Werner M Kistler. *Spiking neuron models: Single neurons, populations, plasticity*. Cambridge university press, 2002.

[13] Richard FitzHugh. Impulses and physiological states in theoretical models of nerve membrane. *Biophysical journal*, 1(6):445, 1961.

[14] Jinichi Nagumo, Suguru Arimoto, and Shuji Yoshizawa. An active pulse transmission line simulating nerve axon. *Proceedings of the IRE*, 50(10):2061–2070, 1962.

[15] Eugene M Izhikevich et al. Simple model of spiking neurons. *IEEE Transactions on neural networks*, 14(6):1569–1572, 2003.

[16] Eugene M Izhikevich and Jeff Moehlis. Dynamical systems in neuroscience: The geometry of excitability and bursting. *SIAM review*, 50(2):397, 2008.

[17] Anthony N Burkitt. A review of the integrate-and-fire neuron model: I. homogeneous synaptic input. *Biological cybernetics*, 95(1):1–19, 2006.

[18] Anthony N Burkitt. A review of the integrate-and-fire neuron model: Ii. inhomogeneous synaptic input and network properties. *Biological cybernetics*, 95(2):97–112, 2006.

[19] Nicolas Brunel. Dynamics of sparsely connected networks of excitatory and inhibitory spiking neurons. *J. Comput. Neurosci.*, 8(3):183–208, 2000.

[20] Nicolas Brunel and Vincent Hakim. Fast global oscillations in networks of integrate-and-fire neurons with low firing rates. *Neural. Comput.*, 11(1):1621–1671, mar 1999.

[21] Alfonso Renart, Rubén Moreno-Bote, Xiao-Jing Wang, and Néstor Parga. Mean-driven and fluctuation-driven persistent activity in recurrent networks. *Neural. Comput.*, 19(1):1–46, 2007.

[22] Magnus JE Richardson and Rupert Swarbrick. Firing-rate response of a neuron receiving excitatory and inhibitory synaptic shot noise. *Physical review letters*, 105(17):178102, 2010.

[23] Eric R Kandel, James H Schwartz, Thomas M Jessell, et al. *Principles of neural science*, volume 4. McGraw-Hill New York, 2000.

[24] Simona Olmi, Antonio Politi, and Alessandro Torcini. Collective chaos in pulse-coupled neural networks. *Europhys. Lett.*, pages 60007+, December 2010.

[25] Carl van Vreeswijk. Partial synchronization in populations of pulse-coupled oscillators. *Phys. Rev. E*, 54(5):5522–5537, November 1996.

[26] D Terman, N Kopell, and A Bose. Dynamics of two mutually coupled slow inhibitory neurons. *Physica D: Nonlinear Phenomena*, 117(1):241–275, 1998.

[27] David Golomb and John Rinzel. Clustering in globally coupled inhibitory neurons. *Physica D: Nonlinear Phenomena*, 72(3):259–282, 1994.

[28] John O'Keefe and Michael L Recce. Phase relationship between hippocampal place units and the eeg theta rhythm. *Hippocampus*, 3(3):317–330, 1993.

[29] Jan-Mathijs Schoffelen, Robert Oostenveld, and Pascal Fries. Neuronal coherence as a mechanism of effective corticospinal interaction. *Science*, 308(5718):111–113, 2005.

[30] Ole Jensen and John E Lisman. Position reconstruction from an ensemble of hippocampal place cells: contribution of theta phase coding. *Journal of neurophysiology*, 83(5):2602–2609, 2000.

[31] Edvard I Moser, Emilio Kropff, and May-Britt Moser. Place cells, grid cells, and the brain's spatial representation system. *Annu. Rev. Neurosci.*, 31:69–89, 2008.

[32] Renato E Mirollo and Steven H Strogatz. Synchronization of pulse-coupled biological oscillators. *SIAM Journal on Applied Mathematics*, 50(6):1645–1662, 1990.

[33] Carl Van Vreeswijk, LF Abbott, and G Bard Ermentrout. When inhibition not excitation synchronizes neural firing. *Journal of computational neuroscience*, 1(4):313–321, 1994.

[34] David Golomb and John Rinzel. Dynamics of globally coupled inhibitory neurons with heterogeneity. *Physical review E*, 48(6):4810, 1993.

[35] Stefano Luccioli and Antonio Politi. Irregular Collective Behavior of Heterogeneous Neural Networks. *Phys. Rev. Lett.*, 105(15):158104+, October 2010.

[36] Gyorgy Buzsaki. *Rhythms of the Brain.* Oxford University Press, USA, 1 edition, August 2006.

[37] Robert W Williams and Karl Herrup. The control of neuron number. *Annual review of neuroscience*, 11(1):423–453, 1988.

[38] Christoph Börgers and Nancy Kopell. Synchronization in networks of excitatory and inhibitory neurons with sparse, random connectivity. *Neural computation*, 15(3):509–538, 2003.

[39] Christof Koch. *Biophysics of Computation: Information Processing in Single Neurons (Computational Neuroscience).* Oxford University Press, 1 edition, November 1998.

[40] Bilal Haider, Alvaro Duque, Andrea R. Hasenstaub, and David A. McCormick. Neocortical network activity in vivo is generated through a dynamic balance of excitation and inhibition. *J. Neurosci.*, 26(17):4535–4545, 2006.

[41] Alfonso Renart, Jaime de la Rocha, Peter Bartho, Liad Hollender, Néstor Parga, Alex Reyes, and Kenneth D Harris. The asynchronous state in cortical circuits. *Science*, 327(5965):587–590, 2010.

[42] Michael London, Arnd Roth, Lisa Beeren, Michael Häusser, and Peter E. Latham. Sensitivity to perturbations in vivo implies high noise and suggests rate coding in cortex. *Nature.*, 466:123–127, jul 2010.

[43] Henk J Groenewegen. The basal ganglia and motor control. *Neural plasticity*, 10(1-2):107–120, 2003.

[44] Gustavo BM Mello, Sofia Soares, and Joseph J Paton. A scalable population code for time in the striatum. *Current Biology*, 25(9):1113–1122, 2015.

[45] Ann E Kelley. Ventral striatal control of appetitive motivation: role in ingestive behavior and reward-related learning. *Neuroscience & biobehavioral reviews*, 27(8):765–776, 2004.

[46] Benjamin R Miller, Adam G Walker, Anand S Shah, Scott J Barton, and George V Rebec. Dysregulated information processing by medium spiny neurons in striatum of freely behaving mouse models of huntington's disease. *Journal of neurophysiology*, 100(4):2205–2216, 2008.

[47] Joshua D Berke, Murat Okatan, Jennifer Skurski, and Howard B Eichenbaum. Oscillatory entrainment of striatal neurons in freely moving rats. *Neuron*, 43(6):883–896, 2004.

[48] Luis Carrillo-Reid, Fatuel Tecuapetla, Dagoberto Tapia, Arturo Hernández-Cruz, Elvira Galarraga, René Drucker-Colin, and José Bargas. Encoding network states by striatal cell assemblies. *Journal of neurophysiology*, 99(3):1435–1450, 2008.

[49] Luis Carrillo-Reid, Salvador Hernández-López, Dagoberto Tapia, Elvira Galarraga, and José Bargas. Dopaminergic modulation of the striatal microcircuit: receptor-specific configuration of cell assemblies. *The Journal of Neuroscience*, 31(42):14972–14983, 2011.

[50] Mark J West, Karen Østergaard, Ole A Andreassen, and Bente Finsen. Estimation of the number of somatostatin neurons in the striatum: an in situ hybridization study using the optical fractionator method. *Journal of Comparative Neurology*, 370(1):11–22, 1996.

[51] Dorothy E Oorschot. Total number of neurons in the neostriatal, pallidal, subthalamic, and substantia nigral nuclei of the rat basal ganglia: a stereological study using the cavalieri and optical disector methods. *Journal of Comparative Neurology*, 366(4):580–599, 1996.

[52] Mark J Tunstall, Dorothy E Oorschot, Annabel Kean, and Jeffery R Wickens. Inhibitory interactions between spiny projection neurons in the rat striatum. *Journal of Neurophysiology*, 88(3):1263–1269, 2002.

[53] Stefano Taverna, Yvette C Van Dongen, Henk J Groenewegen, and Cyriel MA Pennartz. Direct physiological evidence for synaptic connectivity between medium-sized spiny neurons in rat nucleus accumbens in situ. *Journal of neurophysiology*, 91(3):1111–1121, 2004.

[54] James M Tepper, Tibor Koós, and Charles J Wilson. Gabaergic microcircuits in the neostriatum. *Trends in neurosciences*, 27(11):662–669, 2004.

[55] Dieter Jaeger, Hitoshi Kita, and Charles J Wilson. Surround inhibition among projection neurons is weak or nonexistent in the rat neostriatum. *Journal of neurophysiology*, 72(5):2555–2558, 1994.

[56] Tibor Koós and James M Tepper. Inhibitory control of neostriatal projection neurons by gabaergic interneurons. *Nature neuroscience*, 2(5):467–472, 1999.

[57] Paul Erdös and Alfréd Rényi. On the evolution of random graphs. *Publ. Math. Inst. Hung. Acad. Sci*, 5:17–61, 1960.

[58] Mark Newman. *Networks: an introduction*. Oxford University Press, 2010.

[59] Antonio Politi and Alessandro Torcini. Stable chaos. In *Nonlinear Dynamics and Chaos: Advances and Perspectives*, pages 103–129. Springer, 2010.

[60] Rüdiger Zillmer, Nicolas Brunel, and David Hansel. Very long transients, irregular firing, and chaotic dynamics in networks of randomly connected inhibitory integrate-and-fire neurons. *Phys. Rev. E*, 79:031909, Mar 2009.

[61] L. F. Abbott and Carl van Vreeswijk. Asynchronous states in networks of pulse-coupled oscillators. *Phys. Rev. E*, 48(2):1483–1490, August 1993.

[62] Yehezkel Ben-Ari. Developing networks play a similar melody. *Trends in neurosciences*, 24(6):353–360, 2001.

[63] Paolo Bonifazi, Miri Goldin, Michel A Picardo, Isabel Jorquera, A Cattani, Gregory Bianconi, Alfonso Represa, Yehezkel Ben-Ari, and Rosa Cossart. Gabaergic hub neurons orchestrate synchrony in developing hippocampal networks. *Science*, 326(5958):1419–1424, 2009.

[64] Simona Olmi, Roberto Livi, Antonio Politi, and Alessandro Torcini. Collective oscillations in disordered neural networks. *Phys. Rev. E*, 81(4 Pt 2), April 2010.

[65] D Golomb, D Hansel, and G Mato. Mechanisms of synchrony of neural activity in large networks. *Handbook of biological physics*, 4:887–968, 2001.

[66] Lorenzo Tattini, Simona Olmi, and Alessandro Torcini. Coherent periodic activity in excitatory erdos-renyi neural networks: the role of network connectivity. *Chaos*, 22(2):023133, jun 2012.

[67] Stefano Luccioli, Simona Olmi, Antonio Politi, and Alessandro Torcini. Collective dynamics in sparse networks. *Phys. Rev. Lett.*, 109:138103, Sep 2012.

[68] Claudio J Tessone, Claudio R Mirasso, Raúl Toral, and James D Gunton. Diversity-induced resonance. *Physical review letters*, 97(19):194101, 2006.

[69] Claudio J Tessone, Alessandro Scirè, Raúl Toral, and Pere Colet. Theory of collective firing induced by noise or diversity in excitable media. *Physical Review E*, 75(1):016203, 2007.

[70] BA Huberman, JP Crutchfield, and NH Packard. Noise phenomena in josephson junctions. *App. Phys. Lett.*, 37(8):750–752, 1980.

[71] JB Gao, SK Hwang, and JM Liu. When can noise induce chaos? *Phys. Rev. Lett.*, 82(6):1132, 1999.

[72] Brian Dennis, Robert A Desharnais, JM Cushing, Shandelle M Henson, and RF Costantino. Can noise induce chaos? *Oikos*, 102(2):329–339, 2003.

[73] Simona Olmi and Alessandro Torcini. Coherent activity in excitatory pulse-coupled networks. *Scholarpedia*, 8(10):30928, 2013.

[74] Rüdiger Zillmer, Roberto Livi, Antonio Politi, and Alessandro Torcini. Stability of the splay state in pulse-coupled networks. *Phys. Rev. E*, 76:046102, Oct 2007.

[75] Réka Albert and Albert-László Barabási. Statistical mechanics of complex networks. *Rev. Mod. Phys.*, 74(1):47, 2002.

[76] R. Mannella. Absorbing boundaries and optimal stopping in a stochastic differential equation. *Phys. Lett. A*, 254(5):257 – 262, 1999.

[77] Maxi San Miguel and Raul Toral. Stochastic effects in physical systems. In *Instabilities and nonequilibrium structures VI*, pages 35–127. Springer, 2000.

[78] Giancarlo Benettin, Luigi Galgani, Antonio Giorgilli, and Jean-Marie Strelcyn. Lyapunov characteristic exponents for smooth dynamical systems and for hamiltonian systems; a method for computing all of them. part 1: Theory. *Meccanica*, 15(1):9–20, 1980.

[79] Peter C Müller. Calculation of lyapunov exponents for dynamic systems with descontinuities. *Chaos. Soliton. Fract.*, 5(9):1671–1681, 1995.

[80] Ch Dellago, Harald A Posch, and William G Hoover. Lyapunov instability in a system of hard disks in equilibrium and nonequilibrium steady states. *Phys. Rev. E*, 53(2):1485, 1996.

[81] Douglas Zhou, Yi Sun, Aaditya V. Rangan, and David Cai. Spectrum of lyapunov exponents of non-smooth dynamical systems of integrate-and-fire type. *J. Comput. Neurosci.*, 28:229–245, 2010.

[82] Stephen Coombes, Ruediger Thul, and KCA Wedgwood. Nonsmooth dynamics in spiking neuron models. *Physica D*, 241(22):2042–2057, 2012.

[83] S Olmi, A Politi, and A Torcini. Linear stability in networks of pulse-coupled neurons. *Front. Comput. Neurosci.*, 8(8), 2014.

[84] Rüdiger Zillmer, Roberto Livi, Antonio Politi, and Alessandro Torcini. Desynchronization in diluted neural networks. *Phys. Rev. E*, 74(3):036203, 2006.

[85] Sven Jahnke, Raoul-Martin Memmesheimer, and Marc Timme. Stable irregular dynamics in complex neural networks. *Phys. Rev. Lett.*, 100:048102, Jan 2008.

[86] Michael Monteforte and Fred Wolf. Dynamic flux tubes form reservoirs of stability in neuronal circuits. *Phys. Rev. X*, 2:041007, Nov 2012.

[87] David Angulo-Garcia and Alessandro Torcini. Stable chaos in fluctuation driven neural circuits. *Chaos, Solitons & Fractals*, 69(0):233 – 245, 2014.

[88] Alexander Neiman and Lutz Schimansky-Geier. Stochastic resonance in bistable systems driven by harmonic noise. *Phys. Rev. Lett.*, 72(19):2988, 1994.

[89] Matteo di Volo, Raffaella Burioni, Mario Casartelli, Roberto Livi, and Alessandro Vezzani. Heterogeneous mean field for neural networks with short-term plasticity. *Phys. Rev. E*, 90(2):022811, 2014.

[90] D Angulo-Garcia and A Torcini. Stochastic mean-field formulation of the dynamics of diluted neural networks. *Physical Review E*, 91(2):022928, 2015.

[91] W. R. Softky and C. Koch. The highly irregular firing of cortical cells is inconsistent with temporal integration of random epsps. *J. Neurosci.*, 13(1):334–350, 1993.

[92] Gary R Holt, William R Softky, Christof Koch, and Rodney J Douglas. Comparison of discharge variability in vitro and in vivo in cat visual cortex neurons. *J. Neurophysiol.*, 75(5):1806–1814, 1996.

[93] Klaus M. Stiefel, Bernhard Englitz, and Terrence J. Sejnowski. Origin of intrinsic irregular firing in cortical interneurons. *P. Nat. Acad. Sci. USA*, 110(19):7886–7891, 2013.

[94] Henry C Tuckwell. *Introduction to theoretical neurobiology: Volume 2, nonlinear and stochastic theories*, volume 8. Cambridge University Press, 2005.

[95] Ashok Litwin-Kumar and Brent Doiron. Slow dynamics and high variability in balanced cortical networks with clustered connections. *Nature. Neurosci.*, 15(11):1498–1505, 2012.

[96] Misha V. Tsodyks and Terrance Sejnowski. Rapid state switching in balanced cortical network models. *Network-Comp. Neural.*, 6(2):111–124, 1995.

[97] Tim P. Vogels, Kanaka Rajan, and L.F. Abbott. Neural networks dynamics. *Annu. Rev. Neurosci.*, 28(1):357–376, 2005.

[98] Sven Jahnke, Raoul-Martin Memmesheimer, and Marc Timme. How chaotic is the balanced state? *Front. Comp. Neurosci.*, 3(13), Nov 2009.

[99] A Politi, R Livi, G-L Oppo, and R Kapral. Unpredictable behaviour in stable systems. *Europhys. Lett.*, 22(8):571, 1993.

[100] PHE Tiesinga, Jorge V José, and Terrence J Sejnowski. Comparison of current-driven and conductance-driven neocortical model neurons with hodgkin-huxley voltage-gated channels. *Phys. Rev. E*, 62(6):8413, 2000.

[101] Erik Aurell, Guido Boffetta, Andrea Crisanti, Giovanni Paladin, and Angelo Vulpiani. Growth of noninfinitesimal perturbations in turbulence. *Phys. Rev. Lett.*, 77:1262–1265, Aug 1996.

[102] Gina G Turrigiano, Kenneth R Leslie, Niraj S Desai, Lana C Rutherford, and Sacha B Nelson. Activity-dependent scaling of quantal amplitude in neocortical neurons. *Nature*, 391(6670):892–896, 1998.

[103] Gina G Turrigiano. The self-tuning neuron: synaptic scaling of excitatory synapses. *Cell*, 135(3):422–435, 2008.

[104] Michael Monteforte and Fred Wolf. Dynamical entropy production in spiking neuron networks in the balanced state. *Phys. Rev. Lett.*, 105(26):268104, 2010.

[105] Carl van Vreeswijk and Haim Sompolinsky. Chaos in neuronal networks with balanced excitatory and inhibitory activity. *Science*, 274(5293):1724–1726, 1996.

[106] Tobias Letz and Holger Kantz. Characterization of sensitivity to finite perturbations. *Phys. Rev. E*, 61:2533–2538, Mar 2000.

[107] Massimo Cencini, Fabio Cecconi, and Angelo Vulpiani. *Chaos: From Simple Models to Complex Systems.* Series on advances in statistical mechanics. World Scientific, 2010.

[108] Antonio Politi. Lyapunov exponent. 8(3):2722, 2013.

[109] Alessandro Torcini, Peter Grassberger, and Antonio Politi. Error propagation in extended chaotic systems. *J. Phys. A-Math. Gen.*, 28(16):4533, 1995.

[110] Tatsuo Shibata and Kunihiko Kaneko. Collective chaos. *Phys. Rev. Lett.*, 81:4116–4119, Nov 1998.

[111] M Cencini, M Falcioni, D Vergni, and A Vulpiani. Macroscopic chaos in globally coupled maps. *Physica D*, 130(1):58–72, 1999.

[112] Massimo Cencini and Alessandro Torcini. Linear and nonlinear information flow in spatially extended systems. *Phys. Rev. E*, 63:056201, Apr 2001.

[113] Arkady Pikovsky and Antonio Politi. Dynamic localization of lyapunov vectors in spacetime chaos. *Nonlinearity*, 11(4):1049, 1998.

[114] Marcus Stephenson-Jones, Ebba Samuelsson, Jesper Ericsson, Brita Robertson, and Sten Grillner. Evolutionary conservation of the basal ganglia as a common vertebrate mechanism for action selection. *Current Biology*, 21(13):1081–1091, 2011.

[115] Nathaniel D Daw and Kenji Doya. The computational neurobiology of learning and reward. *Current opinion in neurobiology*, 16(2):199–204, 2006.

[116] Hugo Merchant, Deborah L Harrington, and Warren H Meck. Neural basis of the perception and estimation of time. *Annual review of neuroscience*, 36:313–336, 2013.

[117] Philip M Groves. A theory of the functional organization of the neostriatum and the neostriatal control of voluntary movement. *Brain Research Reviews*, 5(2):109–132, 1983.

[118] David G Beiser and James C Houk. Model of cortical-basal ganglionic processing: encoding the serial order of sensory events. *Journal of Neurophysiology*, 79(6):3168–3188, 1998.

[119] Luis Carrillo-Reid, Fatuel Tecuapetla, Osvaldo Ibáñez-Sandoval, Arturo Hernández-Cruz, Elvira Galarraga, and José Bargas. Activation of the cholinergic system endows compositional properties to striatal cell assemblies. *Journal of neurophysiology*, 101(2):737–749, 2009.

[120] Jaime N Guzmán, Adán Hernández, Elvira Galarraga, Dagoberto Tapia, Antonio Laville, Ramiro Vergara, Jorge Aceves, and José Bargas. Dopaminergic modulation of axon collaterals interconnecting spiny neurons of the rat striatum. *The Journal of neuroscience*, 23(26):8931–8940, 2003.

[121] Adam Ponzi and Jeff Wickens. Sequentially switching cell assemblies in random inhibitory networks of spiking neurons in the striatum. *The Journal of Neuroscience*, 30(17):5894–5911, 2010.

[122] Adam Ponzi and Jeff Wickens. Input dependent cell assembly dynamics in a model of the striatal medium spiny neuron network. *Frontiers in systems neuroscience*, 6, 2012.

[123] Adam Ponzi and Jeffery R Wickens. Optimal balance of the striatal medium spiny neuron network. *PLoS computational biology*, 9(4):e1002954, 2013.

[124] Joshua D Berke, Jason T Breck, and Howard Eichenbaum. Striatal versus hippocampal representations during win-stay maze performance. *Journal of neurophysiology*, 101(3):1575–1587, 2009.

[125] Damian M Cummings, Carlos Cepeda, and Michael S Levine. Alterations in striatal synaptic transmission are consistent across genetic mouse models of huntington's disease. *ASN neuro*, 2(3):AN20100007, 2010.

[126] Violeta G López-Huerta, Luis Carrillo-Reid, Elvira Galarraga, Dagoberto Tapia, Tatiana Fiordelisio, Rene Drucker-Colin, and Jose Bargas. The balance of striatal feedback transmission is disrupted in a model of parkinsonism. *The Journal of Neuroscience*, 33(11):4964–4975, 2013.

[127] Dietmar Plenz and Stephen T Kitai. Up and down states in striatal medium spiny neurons simultaneously recorded with spontaneous activity in fast-spiking interneurons studied in cortex–striatum–substantia nigra organotypic cultures. *The Journal of Neuroscience*, 18(1):266–283, 1998.

[128] Gloria J Klapstein, Robin S Fisher, Hadi Zanjani, Carlos Cepeda, Eve S Jokel, Marie-Françoise Chesselet, and Michael S Levine. Electrophysiological and morphological changes in striatal spiny neurons in r6/2 huntington's disease transgenic mice. *Journal of neurophysiology*, 86(6):2667–2677, 2001.

[129] Henrike Planert, Thomas K Berger, and Gilad Silberberg. Membrane properties of striatal direct and indirect pathway neurons in mouse and rat slices and their modulation by dopamine. *PloS one*, 8(3):e57054, 2013.

[130] Dietmar Plenz. When inhibition goes incognito: feedback interaction between spiny projection neurons in striatal function. *Trends in neurosciences*, 26(8):436–443, 2003.

[131] Tibor Koos, James M Tepper, and Charles J Wilson. Comparison of ipscs evoked by spiny and fast-spiking neurons in the neostriatum. *The Journal of neuroscience*, 24(36):7916–7922, 2004.

[132] S Schreiber, JM Fellous, D Whitmer, P Tiesinga, and Terrence J Sejnowski. A new correlation-based measure of spike timing reliability. *Neurocomputing*, 52:925–931, 2003.

[133] Mark EJ Newman. Fast algorithm for detecting community structure in networks. *Physical review E*, 69(6):066133, 2004.

[134] Mark D Humphries. Spike-train communities: finding groups of similar spike trains. *The Journal of Neuroscience*, 31(6):2321–2336, 2011.

[135] Santo Fortunato. Community detection in graphs. *Physics Reports*, 486(3):75–174, 2010.

[136] Peter Ronhovde and Zohar Nussinov. Local resolution-limit-free potts model for community detection. *Physical Review E*, 81(4):046114, 2010.

[137] Jörg Reichardt and Stefan Bornholdt. Statistical mechanics of community detection. *Physical Review E*, 74(1):016110, 2006.

[138] Vincent D Blondel, Jean-Loup Guillaume, Renaud Lambiotte, and Etienne Lefebvre. Fast unfolding of communities in large networks. *Journal of Statistical Mechanics: Theory and Experiment*, 2008(10):P10008, 2008.

[139] Andrea Lancichinetti and Santo Fortunato. Community detection algorithms: a comparative analysis. *Physical review E*, 80(5):056117, 2009.

[140] Aaron Clauset, Mark EJ Newman, and Cristopher Moore. Finding community structure in very large networks. *Physical review E*, 70(6):066111, 2004.

[141] Mark EJ Newman. Analysis of weighted networks. *Physical Review E*, 70(5):056131, 2004.

[142] Mark D Humphries, Ric Wood, and Kevin Gurney. Dopamine-modulated dynamic cell assemblies generated by the gabaergic striatal microcircuit. *Neural Networks*, 22(8):1174–1188, 2009.

[143] Rubén Moreno-Bote and Néstor Parga. Role of synaptic filtering on the firing response of simple model neurons. *Physical review letters*, 92(2):028102, 2004.

[144] Srdjan Ostojic. Two types of asynchronous activity in networks of excitatory and inhibitory spiking neurons. *Nature neuroscience*, 17(4):594–600, 2014.

[145] R Vergara, C Rick, S Hernández-López, JA Laville, JN Guzman, E Galarraga, DJ Surmeier, and J Bargas. Spontaneous voltage oscillations in striatal projection neurons in a rat corticostriatal slice. *The Journal of physiology*, 553(1):169–182, 2003.

[146] Sten Grillner, Jeanette Hellgren, Ariane Menard, Kazuya Saitoh, and Martin A Wikström. Mechanisms for selection of basic motor programs–roles for the striatum and pallidum. *Trends in neurosciences*, 28(7):364–370, 2005.

[147] Omar Jáidar, Luis Carrillo-Reid, Adán Hernández, René Drucker-Colín, José Bargas, and Arturo Hernández-Cruz. Dynamics of the parkinsonian striatal microcircuit: entrainment into a dominant network state. *The Journal of Neuroscience*, 30(34):11326–11336, 2010.

[148] Fatuel Tecuapetla, Luis Carrillo-Reid, José Bargas, and Elvira Galarraga. Dopaminergic modulation of short-term synaptic plasticity at striatal inhibitory synapses. *Proceedings of the National Academy of Sciences*, 104(24):10258–10263, 2007.

[149] Gilles Laurent. Olfactory network dynamics and the coding of multidimensional signals. *Nature Reviews Neuroscience*, 3(11):884–895, 2002.

[150] MI Rabinovich, R Huerta, A Volkovskii, HDI Abarbanel, M Stopfer, and G Laurent. Dynamical coding of sensory information with competitive networks. *Journal of Physiology-Paris*, 94(5):465–471, 2000.

[151] Mikhail I Rabinovich and Pablo Varona. Robust transient dynamics and brain functions. *Frontiers in computational neuroscience*, 5, 2011.

[152] Thomas Nowotny and Mikhail I Rabinovich. Dynamical origin of independent spiking and bursting activity in neural microcircuits. *Physical review letters*, 98(12):128106, 2007.

[153] MA Komarov, GV Osipov, and CS Zhou. Heteroclinic contours in oscillatory ensembles. *Physical Review E*, 87(2):022909, 2013.

[154] D Angulo-Garcia, Joshua D. Berke, and A Torcini. Cell assembly dynamics of sparsely-connected inhibitory networks: a simple model for the collective activity of striatal projection neurons. *arXiv:1511.06920 [q-bio.NC]*.

[155] Simona Olmi. Collective dynamics in complex neural networks. 2013.

[156] William H Press, Saul A Teukolsky, William T Vetterling, and Brian P Flannery. *Numerical recipes in FORTRAN (Cambridge)*. Cambridge Univ. Press, 1992.

[157] Michael Flynn. Some computer organizations and their effectiveness. *Computers, IEEE Transactions on*, 100(9):948–960, 1972.